Influence of the shock wave pressure gradient in α-Fe irradiated by a high-power ion beam on the occurence of a microhardness maximum at large depths

A. N. Valyaev, A. D. Pogrebnyak, V. I. Lavrent'ev, S. N. Volkov, and S. V. Plotnikov

Institute of Surface Modification, Sumy, Ukraine;
Technical University, Ust'-Kamenogorsk, Kazakhstan; Institute of Electrophysics,
Ural Branch of the Russian Academy of Sciences, Tomsk; Vostokmash, Ust'-Kamenogorsk, Kazakhstan
(Submitted May 22, 1997)
Pis'ma Zh. Tekh. Fiz. **24**, 47–53 (February 12, 1998)

The defect structure and microhardness of α-Fe irradiated by a high-power pulsed beam have been studied using positron annihilation, transmission electron spectroscopy, and a nanoindenter, and results are presented. It is shown that in α-Fe exposed to a high-power pulsed beam, the pressure gradient and depth of formation of the shock wave front influence the formation and location of the dislocation density maximum and the microhardness maximum in the modified layer. [S1063-7850(98)00902-1]

As is well known, high-power ion beams are used for surface modification, ion mixing, and for the deposition of films and coatings.[1–4] However, there are various unresolved problems which make it difficult to predict the changes in the physicochemical and operating characteristics of metallic materials. The main difficulty involves taking into account all the processes accompanying the action of a high-power pulsed beam which may influence the defect structure and microhardness, and their final profile in the material. Some of these processes taking place in a metal exposed to a high-power pulsed beam include heating, melting, evaporation, expansion of a vapor-plasma cloud (ablation), shock wave formation, quenching from the liquid to the gaseous state, mass transfer, and so on. The aim of the present study was to make an experimental investigation of the defect structure and microhardness after exposure of α-Fe to a high-power pulsed beam, and to examine the effects which influence the change in depth of the modified layer.

For the investigations we used coarse-grained (1.5–3 mm) $14\times14\times2$ mm annealed α-Fe samples. The high-power pulsed beam irradiation was performed using an accelerator with the beam parameters $E_{av}=300$ keV, pulse duration $t=100$ ns, and current density varying between 10^2 and 2.5×10^3 A/cm^2 (Ref. 5). The beam composition was $C^+\approx50\%$ and $H^+\approx50\%$. The residual pressure in the accelerator chamber was 10^{-5} Torr. The beam cross section was much greater than the size of the samples.

Foils were prepared at known distances from the surface for the electron microscopic examinations of the dislocation structure formed in the surface layers of a target exposed to a high-power pulsed beam. The method of preparing the foils was described in Ref. 6. The positron lifetime was measured using a spectrometer with a time resolution of 220 ps and a fixed full width at half maximum Δt. The positron source was ^{22}Na (B^+,γ) evaporated onto aluminum foil in a Mylar envelope. The source intensity was $\tau_1=150$ ps, $I_1=6.6\%$; $\tau_2=450$ ps, $I_2=2.6\%$ and the spectrum was calibrated using ^{207}Bi. The microhardness measurements were made using a Micromet system. The Rutherford backscattering spectra with channeling were measured using a 2 MeV $^4He^+$ ion beam. The defect profile was measured in the molten zone of the surface layer using a 0.2–30 keV slow positron beam, which allowed us to analyze layers between a few nanometers and 1.2 μm thick.[7]

As a result of quenching from the liquid state (and possibly from the gaseous state), a high concentration of vacancy clusters, impurity complexes, and dislocations form in a surface layer up to 1.2 μm thick, as is evidenced by an increase in the S parameter of the Doppler broadening curves of the annihilation peak compared with the initial (unirradiated) α-Fe sample (Fig. 1a). In the layer where the highest thermomechanical stresses are created (at the boundary between the liquid and solid phases), there is a high concentration of vacancy clusters, between 5×10^{17} and 10^{18} cm^{-3}, together with an advanced dislocation structure having the scalar density $\rho=6.5\times10^9$ cm^{-2} (Fig. 1a, curves *2* and *3*). The results obtained using Rutherford backscattering with channeling (Fig. 1b) indicate that the concentration of interstitial atoms also increased, as is indicated by the increase in χ for the $\langle100\rangle$ and $\langle001\rangle$ directions compared with the initial oriented crystal (coarse-grained).

Note that considerably larger interstitial defects form in the $\langle100\rangle$ direction. In a surface layer up to 5 μm thick the dislocation structure consists of individual, uniformly distributed dislocations. The average dislocation density directly at the surface reaches 3.6×10^9 cm^2. Substantial changes in the dislocation structure begin to appear at depths of 30–40 μm, where the dislocation structure becomes extremely nonuniform. In addition to a chaotic dislocation structure consisting of separate dislocations and entangled dislocations, the structure contains small-angle boundaries which range between dislocation networks with a misorientation angle of 5–7° and regions with a polygonized structure. Under high-power pulsed beam irradiation, the thermal relaxation time is substantially shorter than the irradiation time, so that the almost instantaneous heating of the metal creates stresses in the solid matrix near the surface (thermal impact). The material then melts and is ejected from the surface on the irradiated

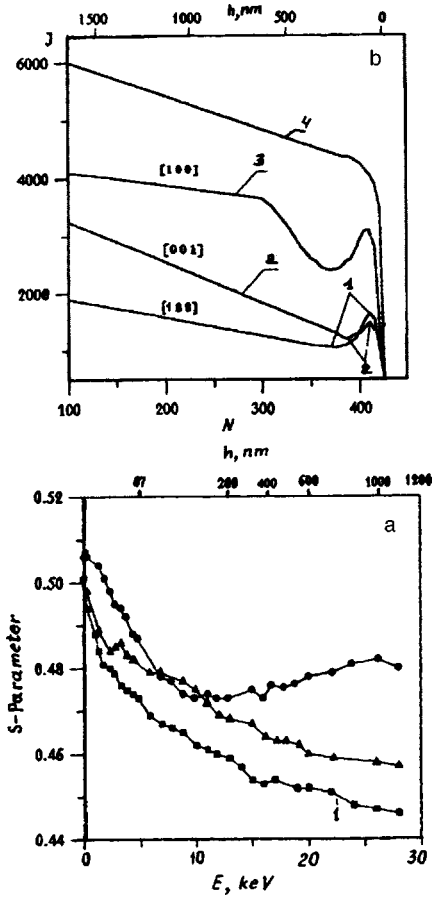

FIG. 1. a—Variation of the S parameter of the Doppler broadening curves of the annihilation peak with depth of the α-Fe layer: *1*—initial state; *2*—irradiated by a high-power pulsed beam with $j=150$ A/cm^2, $\tau=100$ ns; *3*—irradiated by a high-power pulsed beam with $j=400$ A/cm^2, $\tau=100$ ns; b—Energy spectra of Rutherford backscattering of ions with channeling (3 MeV $^4He^+$): *1*—⟨100⟩ orientation in initial state; *2*—⟨001⟩ orientation irradiated by a high-power pulsed beam with $j=400$ A/cm^2, $\tau=100$ ns; *3*—⟨100⟩ orientation irradiated by a high-power pulsed beam with $j=400$ A/cm^2, $\tau=100$ ns, and *4*—misoriented α-Fe grains.

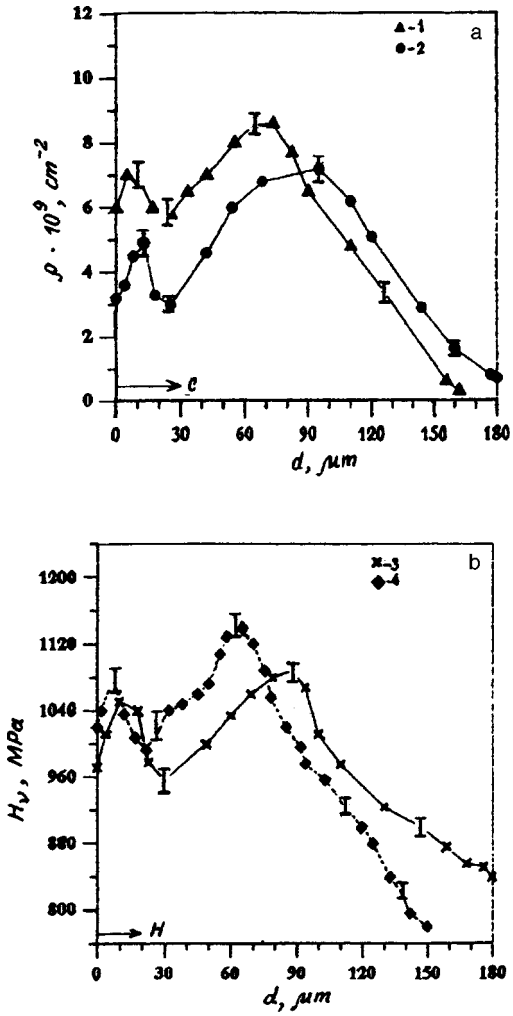

FIG. 2. Dislocation density (a) and microhardness (b) in α-Fe irradiated by a high-power pulsed beam as a function of the depth of the hardened layer (C is the dislocation density of the initial states and H is the microhardness of the unirradiated sample): *1, 3*—$j=150$ A/cm^2, $\tau=100$ ns; *2, 4*—$j=400$ A/cm^2, $\tau=100$ ns.

side. The resultant recoil momentum produces additional compression of the material in the solid phase. We show that the wave generated in this case is a shock wave. The criterion for shock wave formation was obtained for the action of a laser beam[8] and for our case will have the form

$$\frac{IS}{\tau_u} > C_e^4 \rho_0 R_0, \tag{1}$$

$$Q = IS\tau, \tag{2}$$

$$\mu_\Lambda = R_0^{-1}, \tag{3}$$

where I is the intensity, S is the irradiated area, and R_0 is the ion range in the material. These irradiation conditions give $I \sim 10^8$ W/cm^2$=10^{12}$ W/m^2, $\tau \sim 10^{-7}$ s, and $S \sim 10^{-4}$ m^2. For our target, with $C_e = 5\times10^3$ m/s, $\rho_0 = 7.9\times10^3$ kg/m^3, $R_0 = 1$ μm$=10^{-6}$ m, we obtain

$$\frac{IS}{\tau} \approx 10^{15} \quad \text{and} \quad C_e^4 \rho_0 R_0 \approx 10^{12}. \tag{4}$$

Thus, the criterion for the formation of a shock wave is satisfied and its initial pressure is a few gigapascal, i.e., the wave is a weak one between 2 and 10 GPa.

As the shock wave propagates into the target its pressure drops, causing H_v to decrease with depth (Fig. 2). However, the shock wave front becomes steeper (this is confirmed by our calculations) and the pressure gradient increases, reaching a maximum in the region where the shock wave front is formed. Intrinsic and impurity defects will be generated most vigorously near the shock wave front. Interstitial sites are considerably more mobile than vacancies, so that their sink for dislocations fixes the latter, reducing their mobility. Both the matrix atoms and defects (scattering centers) acquire the momentum of the shock wave.

Figures 2a and 2b give the average dislocation density (curves *1* and *2*) and the microhardness as a function of the distance from the surface of α-Fe irradiated by a high-power pulsed beam. These curves show well-defined peaks at the surface and in the interior of the modified layer. An increase in the energy flux (current density) of the high-power pulsed beam shifts the second peak closer to the surface, i.e., the

shock wave pressure gradient and the site of formation of the shock wave front have some influence here.

As a result of measuring the positron lifetime in α-Fe samples irradiated by a high-power pulsed beam, we found that the positrons are captured by vacancy clusters (three or more vacancies) with lifetime $\tau_2 = 224 \pm 5$ ps and $I_2 = 34.5\%$. Fixing the time $\tau_1 = 108$ ps, we obtained $\tau_2' = 165 \pm 2$ ps, which corresponds to the lifetime of positrons localized at dislocations. This agrees well with the results of Ref. 7.

To sum up, these experimental results indicate that a broad spectrum of defects, ranging from vacancy clusters to dislocations and a cellular dislocation structure, develops in the region of maximum shock wave gradient. This behavior suggests that the properties of materials may be specifically altered by selecting a suitable irradiation regime.

This work was partially financed by the Ukraine State Committee for Science and Technology, ''Raduga'' Project 7.5.4/73–93.

The authors would like to thank their colleagues at Sandia National Laboratories and Los Alamos National Laboratory for discussion of the results at seminars. Two of the authors, A. D. Pogrebnyak and A. N. Valyaev, thank the ISF for financing their participation in the IBMM'96 Conference, Albuquerque, USA.

[1] A. D Pogrebnjak, and Sh. M. Ruzimov, Phys. Lett. **120**, 259 (1987).
[2] A. D Pogrebnjak, Phys. Status Solidi **117**, 17 (1990).
[3] A. Davis, G. Remnev, R. Stinnett, and K. Yatsui, MPS Bulletin. **21**, 58 (1996).
[4] K. Yatsui, C. Grigoriu, H. Kubo, K. Masugata, and Y. Shimotori, Appl. Phys. Lett. **67**, 1214 (1995).
[5] A. D. Pogrebnyak, Yu. P. Sharkeev, N. A. Makhmudov, and T. I. Perevalova, and Sh. M. Tukhtaev, Poverkhnost' **3**, 95 (1993).
[6] Yu. F. Ivanov, A. D. Pogrebnyak, V. A. Martynenko, and R. Oshner, Fiz. Khim. Obrab. Mater. **6**, 13 (1996).
[7] A. Zecca, R. S. Brusa, M. Duarte Naia, J. Paridaens, A. D. Pogrebnjak, A. B. Markov, G. E. Ozur, D. I. Proskurovsky, and V. P. Rotstein, Phys. Lett. A **175**, 433 (1993).
[8] B. Steverding and A. H. Werhheiser, J. Phys. D , 545 (1971).

Translated by R. M. Durham

Initial peak on the time dependence of the heterogeneous recombination velocity of hydrogen atoms at the surface of phosphor crystals

V. F. Kharlamov, N. F. Vasil'ev, O. A. Ivashchuk, E. P. Krutovskiĭ, Yu. V. Mosin, and E. A. Zlotkin

Orlovsk State Technical University
(Submitted May 26, 1997)
Pis'ma Zh. Tekh. Fiz. **24**, 54–59 (February 12, 1998)

The radical recombination luminescence of phosphor crystals in strong atomic fluxes was investigated. An initial emission intensity peak was observed whose amplitude depends on the magnitude of the atomic flux, the phosphor crystal temperature, and the interval between switching the atomic source off and on. © *1998 American Institute of Physics.*
[S1063-7850(98)01002-7]

The heterogeneous recombination reaction of hydrogen atoms at the surface of solids is accompanied not only by the generation of phonons but also by the electronic excitation of the crystals, which results in the emission of photons and electrons as well as the formation of electron–hole pairs. The electronic accommodation of the chemical reaction energy produced by the heterogeneous recombination of H atoms may be the dominant mechanism of energy dissipation which controls the reaction rate and the intensity of the surface chemiluminescence.[1] For weak fluxes of atomic hydrogen ($j=10^{12}-10^{17}$ cm$^{-2}\cdot$s^{-1}) the intensity I of the radical recombination luminescence of phosphor crystals depends linearly on the density N of chemisorbed atoms and the atomic flux j:

$$I(t)=ajN(t), \tag{1}$$

where t is the time, a is a coefficient which depends on the temperature and type of phosphor, $j=0.25\,\overline{v}n$, n is the density of gas-phase atoms, and $\overline{v}$ is their thermal velocity.[1,2]

We observed that condition (1) is not satisfied. We found that for strong atomic fluxes $j\approx 10^{18}$ cm$^{-2}\cdot$s^{-1} and the curves $I(t)$ become abruptly nonmonotonic.

Spectrally pure hydrogen was prepared by diffusion across electrically heated nickel and was pumped continuously through a vacuum chamber containing the sample. Hydrogen atoms were generated using an rf electric discharge in a molecular gas. For the experiments we used finely dispersed CaO–Bi and ZnS–Tm phosphors with a specific surface area of ~ 1 m$^2\cdot$g^{-1}. The intensity of the radical recombination luminescence was recorded using a photomultiplier and a recording millivoltmeter. The phosphors were deposited on an electrically heated molybdenum substrate or were deposited on both surfaces of a quartz piezoresonance transducer which measured the weight with a sensitivity of 10^{-3} monolayers.

The samples were preliminarily outgassed in atomic hydrogen. The temperature of the walls of the glass vacuum chamber containing the sample was held at $T=450$ K for 2 h, and the removal of adsorbed contaminants was monitored from the readings of the piezotransducer. The kinetics of the radical recombination luminescence and the adsorption kinetics of the H atoms were recorded after a pause in the excitation of the sample by atomic hydrogen, during which chemisorbed atoms were desorbed from the surface by recombination.

The curves $I(t)$ contain an initial peak of 1 s duration (Fig. 1), whose amplitude depends on the magnitude of the atomic flux j, the phosphor crystal temperature, and the pause between switching off and switching on the atomic source. When the density of gas-phase atoms is reduced by decreasing the rf discharge power, the initial peak on the curve $I(t)$ disappears. According to the piezotransducer readings, after the atomic source is switched on, filling of the surface of the phosphor crystals with chemisorbed H atoms takes place slowly and continues for more than 20 s, and the $I(t)$ and $N(t)$ curves differ. Recombination desorption of atoms is observed for more than 100 s after the rf discharge is switched off.

The curve (1) obtained for low atomic hydrogen fluxes for CaO–Bi, ZnS–Tm, and other phosphors indicates that no luminescence is excited in the H atom adsorption processes (no adsorboluminescence is observed).[1,2] Thus, the initial peak observed on the curves $I(t)$ should be attributed to the abruptly nonmonotonic time dependence of the reaction rate for the heterogeneous recombination of atoms, which is responsible for the excitation of radical recombination luminescence.

In order to interpret these experimental results, in the model describing the heterogeneous recombination reaction of hydrogen atoms at the surface of solids,[3–5]

$$R+Z\rightleftarrows RZ \quad \text{(I)} \quad RZ\rightleftarrows (RZ) \quad \text{(II)}$$

$$2RZ\rightarrow R_2+2Z \quad \text{(III)} \quad RZ+(RZ)\rightarrow R_2+2Z \quad \text{(IV)}$$

$$R+Z\rightleftarrows (RZ) \quad \text{(V)} \quad 2(RZ)\rightleftarrows R_2+2Z \quad \text{(VI)}$$

we also take into account the physical adsorption of atoms in the second adlayer and transitions of atoms from the second adlayer to free adsorption states of the first adlayer:

$$R+V\rightleftarrows RV \quad \text{(VII)} \quad RV+Z\rightleftarrows V+RZ \quad \text{(VIII)},$$

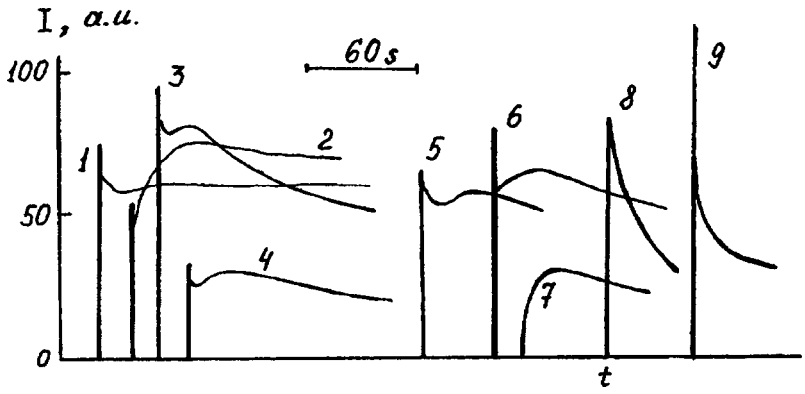

FIG. 1. Time dependence of the radical recombination luminescence intensity of ZnS–Tm (*1–4*) and CaO–Bi (*5–9*) phosphors after switching on a source of hydrogen atoms ($n=10^{13}$ cm^{-3}) at temperature (K): *1, 5, 6*—295, *2*—333, *3*($\times 10$)—370, *4*($\times 10^2$)—395, *7*—413, *8*—470, and *9*—570. Interval between switching off and switching on the H atom source (s): *1–4*—120, *5*—60, and *6–9*—600.

where R is an atom, R_2 is a molecule, Z is an adsorption center, RZ is a preadsorbed atom, (RZ) is a chemiadsorbed atom, V is a complex of m chemisorbed atoms, $m=3$, 4, and RV is a physically adsorbed atom near the minimum of the potential relief, formed by a group of m chemisorbed particles. Reactions (I)–(VIII) correspond to the rate equations:

$$\dot{n}_1=(k_1+k_8n_3)n_4-(k_1'+k_2+k_8'n_2^m)n_1-2k_3n_1^2 - k_4n_1n_2+k_2'n_2,$$

$$\dot{n}_2=k_2n_1+k_5n_4-k_4n_1n_2-2k_6n_2^2+2k_6'n_4^2,$$

$$\dot{n}_3=(k_7+k_8'n_1)n_2^m-k_7'n_3-k_8n_3n_4,$$

$$n_1+n_2+n_4=1,$$

where $n_1=[RZ]$, $n_2=[(RZ)]$, $n_3=[RV]$, and $n_4=[Z]$ are the surface concentrations of the materials, k_1-k_8' are the rate constants of the reactions, $k_i=j\sigma_i$, $i=1$, 5, 7, and σ_i is the cross section for adsorption of atoms in states RZ, (RZ), and RV. Here we have $I=\eta_3k_3n_1^2+\eta_4k_4n_1n_2$, $J\simeq k_3n_1^2+k_4n_1n_2$, where η_3 and η_4 are coefficients, and J is the rate of heterogeneous atomic recombination. We take the following rate constants in reciprocal seconds: $k_1=1.62\times 10^2$, $k_1'=10^7$, $k_2=k_2'=k_6'=0$, $k_3=2.86\times 10^{11}$, $k_4=10^3$, $k_5=1.45\times 10^{-2}$, $k_6=10^{-2}$, $k_7=1.42\times 10^{-3}$, $k_7'=10^{11}$, $k_8=2\times 10^{11}$, $k_8'=2\times 10^7$, $m=3$, $\eta_3=2\times 10^{-4}$, and $\eta_4=0.5$ (the condition $\eta_3\ll\eta_4$ may be explained by the low efficiency of the dipole–dipole interaction which is responsible for the electronic excitation of surface luminescence centers in reaction (III) compared with nonadiabatic transitions with exchange of chemical bonds, which are responsible for the electronic excitation of the surface in reaction (IV) (Ref. 3).) In this case, the theoretical curve $J(t)$ contains an initial peak of duration ~ 1 s and has the same profile as the experimental curve $I(t)$ (Fig. 2), where $J(t)\approx k_3n_1^2(t)$, $I(t)\approx\eta_3k_3n_1^2(t)$. The theoretical adsorption and desorption curves $n_2(t)$ exhibited the same behavior as the similar experimental curves $N(t)$. The theoretical value of the heterogeneous atomic recombination coefficient $\gamma=J^*n_2^*N_0j^{-1}=10^{-3}$ also agrees with the experiment, where the asterisk denotes steady-state values and $N_0=10^{14}$ cm^{-2} is the density of adsorption centers for H atoms on the surface of ZnS and CaO (Ref. 3).

Using different values of n (between 1×10^{12} and 3×10^{15} cm^{-3}), we calculated the reaction rates J^* under steady-state conditions and at the maximum of the initial peak J_m, and also the position of the initial peak for which we simulated half-minute pauses between switching off and switching on the atomic source. According to the calculations, in the interval $[0, \tau]$, where $\tau=0.5$–2 s, an increase in the density of gas-phase atoms is accompanied by a shift of the maximum of the initial peak from 0.1 to 1 s. With increasing n, J_m increases more rapidly than J^* and for $n=10^{12}$, we find $J_m=0$. This explains the absence of initial peaks on the experimental curves $I(t)$ for weak atomic fluxes and also the previously observed giant flashes of radical recombination luminescence when phosphors are excited by

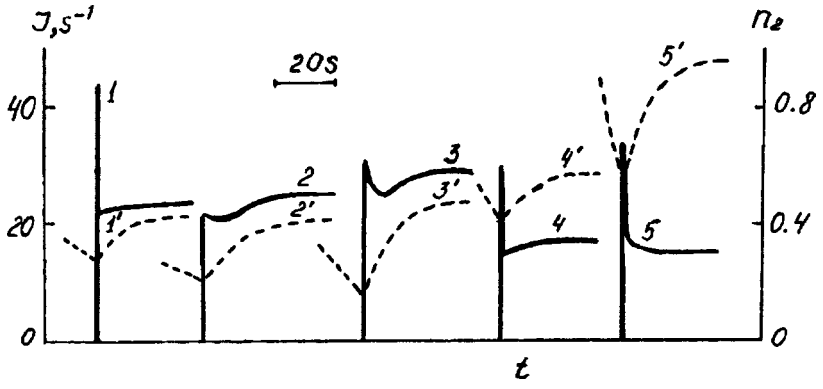

FIG. 2. Curves showing how the theoretical curves $n_2(t)$ (dashed curves) and $J(t)$ are influenced by the interval between switching off and switching on the atom source (s): *1*, *4*($\times 10^{-1}$), *5*($\times 10^{-3}$)—30, *2*—90, *3*—270, and by the density of gas-phase atoms: ($\times 10^{-13}$ cm^{-3}): *1–3*—1, *4*—3, and *5*—3×10^2.

strong fluxes of H atoms ($n \approx 10^{15}$ cm^{-3}) (Ref. 6). Using Eq. (2) for weak atomic fluxes ($j = 10^{12} - 10^{17}$ cm$^{-2} \cdot$s^{-1}) gives a theoretical dependence the same as expression (1) for the intensity of the radical recombination luminescence (in cases of small perturbations, the nonlinear system (I)–(VIII) behaves as a linear one).

To conclude, a previously unknown effect, involving peaking of the heterogeneous chemical reaction rate, has been observed for the heterogeneous recombination of hydrogen atoms. A mathematical model consistent with the experimental results has been proposed for this effect.

[1] V. P. Grankin, Poverkhnost'. No 1. 20 (1997).
[2] V. P. Grankin, N. D. Grankina, and V. V. Styrov, Zh. Fiz. Khim. **67**, 1669 (1993).
[3] V. F. Kharlamov, *Recombination of Atoms at the Surface of Solids and Accompanying Effects* [in Russian], Tomsk State University Press, Tomsk (1994).
[4] V. F. Kharlamov, Sh. L. Izmailov, and N. Ph. Vasil'ev, React. Kinet. Catal. Lett. **60**, 107 (1997).
[5] V. F. Kharlamov, Zh. Fiz. Khim. **71**, 678 (1997).
[6] Sh. L. Izmaĭlov and V. F. Kharlamov, Izv. Vyssh. Uchebn. Zaved. Fiz. No. 12, , 89 (1984).

Translated by R. M. Durham

Formation of a low-resistivity penetrating metal–Si layer under the action of CO_2 laser radiation

P. S. Shkumbatyuk

Drogobych Pedagogical Institute
(Submitted June 25, 1997)
Pis'ma Zh. Tekh. Fiz. **24**, 60–63 (February 12, 1998)

Some characteristic features observed as a result of the action of CO_2 laser radiation on a metal–silicon layer are described, especially the formation of a low-resistivity penetrating layer. The assumption is put forward that this low-resistivity penetrating layer forms as a result of the solid-phase dissolution of metal in Si or by diffusion of the metal into defects formed by laser radiation. © *1998 American Institute of Physics.* [S1063-7850(98)01102-1]

Studies of the action of laser radiation with $h\nu \geqslant E_e$ on Si are known to be of scientific interest as a possible technological method of controlling the electrophysical properties of ion-doped alloys. Of particular importance is the problem of defect formation, where the influence of local electronic excitations and heating induced by the laser radiation may be the dominant mechanism. In view of the important role of electronic and electron–phonon excitations, studies of the action of $h\nu < E_g$ laser radiation on Si are equally important in order to investigate the mechanism of defect formation. According to Refs. 1–3, one method of studying the action of $h\nu < E_e$ radiation on Si is to investigate the thermal effects induced by the absorption of radiation by free carriers.

Thus, some characteristic features of the action of cw CO_2 laser radiation on metal–Si are reported here. A metal–Si sandwich (p–Si, $\rho = 1 \times 10^2\ \Omega \cdot$cm, $t = 0.6$ mm) was exposed to CO_2 laser radiation at a power density up to 10^3 W/cm^2 for up to 20 s at room temperature in air. The metals used were Au, Cu, and Al weighing up to 2 mg. The temperature to which the metal–Si was heated by the radiation, measured by pyrometry, was $1-1.2\times 10^3$ °C.

Figure 1a shows the surface of one half of a cleaved Al–Si interaction zone after exposure to laser radiation. Depending on the irradiation time and the power density, the contact zone had a depth of up to 0.1 mm with an oxidized surface consisting of Al and Si. Within this layer (Fig. 1b) a polycrystalline friable structure is observed, with no metal inclusions. With decreasing power density and increasing irradiation time (Fig. 1c), the structure becomes less friable and the metal–Si surface area decreases. After laser anneal-

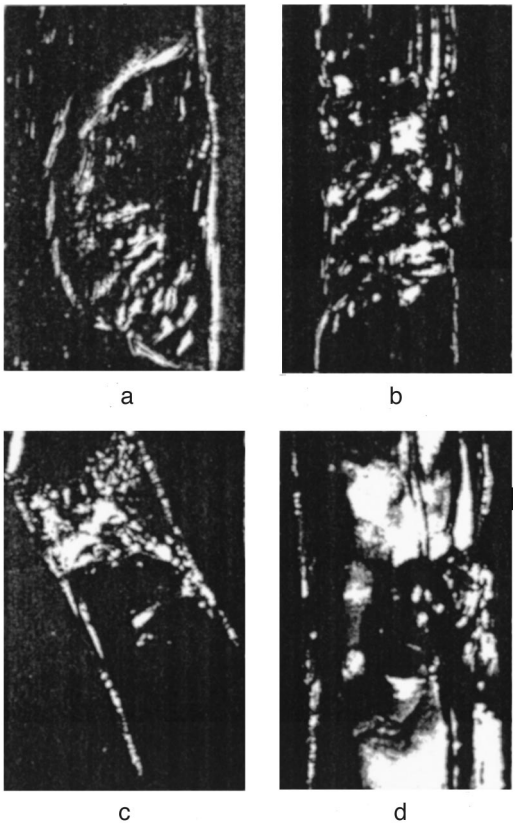

FIG. 1. Structural changes to a low-resistivity penetrating Al–Si layer after laser irradiation: a—irradiated surface; b, c—vs. thickness, and d—vs. thickness after laser annealing (×50) (a, b, c—×40.

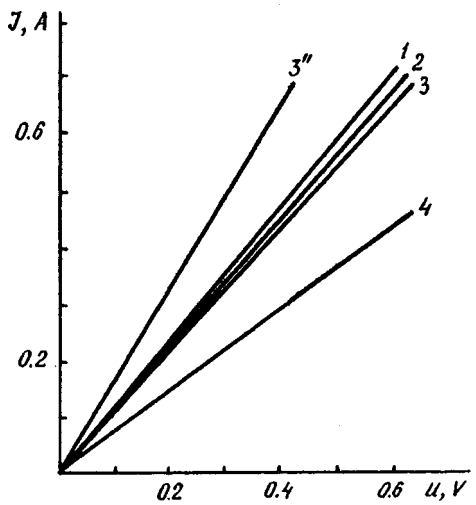

FIG. 2. Current–voltage characteristics of a low-resistivity penetrating metal–Si layer at 300 K: *1*—Au–Si, *2*—Cu–Si, *3*—Al–Si, *3″*—Al–Si at 77 K, and *4*—after annealing.

ing (Fig. 1d), a single-crystal structure is observed with an elevated defect concentration in the irradiation zone. After irradiation of Cu–Si a polycrystalline structure is observed within the layer, with larger blocks compared with the Al–Si structure and no metal inclusions. The interaction surface consists of copper oxides and silicon particles. When contact is established between Au and Si, no polycrystalline structure is formed and penetrations in the form of microchannels and Au inclusions are identified over the thickness.

Assuming that the metal–Si structure does not melt as a result of the irradiation and annealing, it may be postulated that a low-resistivity penetrating layer is formed by solid-phase dissolution of the metal in Si or by the diffusion of metal in laser-induced defects.

The electrical properties of the penetrating layer were investigated using the current–voltage characteristics at 77 and 300 K. For the measurements the resistance of the system was limited by the resistance of the output contacts which was 0.75 Ω at 300 K. Before soldering the outputs for Al–Si, Au was fused onto the surface of the contact by short-lived laser irradiation. Figure 2 gives the linear current–voltage characteristics of the low-resistivity layers for the positive direction of current. For the annealed layer (Fig. 2, curve *4*) the increase in resistivity is caused by a decrease in the metal concentration, which indicates that metal reaches the surface region, possibly in the direction of the laser irradiation.

[1] R. A. Weeks, J. Non-Cryst. Solids **71**, 435 (1983).
[2] A. V. Zoteev and V. F. Kiselev, Vestn. Mosk. Gos. Univ. Ser. Fiz. Astron. **28**, No 1, 20 (1987).
[3] I. W. Boyd, J. Appl. Phys. **54**, 3561 (1983).

Translated by R. M. Durham

Structural, mechanical, and frictional properties of titanium nitride films exposed to continuous ion beam bombardment

I. G. Romanov, I. N. Tsareva, and L. A. Krivina

Nizhniĭ Novgorod Branch of the A. A. Blagonravov Institute of Mechanical Engineering, Russian Academy of Sciences

(Submitted July 10, 1997)
Pis'ma Zh. Tekh. Fiz. **24**, 64–68 (February 12, 1998)

The influence of low-dose (10^{14}–10^{15} cm^{-2}) ion bombardment on the structural, mechanical, and frictional properties of titanium nitride films has been studied and results are presented. It is shown that at these doses plastic deformation processes take place in the target material, which change the degree of crystallinity. By selecting the bombardment conditions, the properties of TiN films can be varied fairly widely. © *1998 American Institute of Physics.* [S1063-7850(98)01202-6]

Recently, considerable attention has been paid to new, wear-resistant coatings used in various fields of technology. Of particular importance are ion-plasma technologies which can produce carbonitride films with enhanced physicomechanical, tribological, and anticorrosion properties. However, the development of modern materials science requires research to strengthen still further already available high-strength materials. Ion implantation is extremely promising for these purposes.

Here we report results of a study of the influence of continuous ion beams on various properties of titanium nitride films. The films were deposited at a pressure of 1.06 Pa using an NNV-11 system. For the experiments we used ceramic substrates (Al_2O_3) and NaCl samples. The thickness of the films varied between 0.25 and 3 μm. The samples were bombarded by continuous 40 keV B^+ and Ar^+ ion beams at $j=8-10$ μA/cm^2 using the ILU accelerator. The ion doses varied between 6×10^{13} and 6×10^{16} cm^{-2}. Before and after the ion bombardment, the TiN samples were subjected to electron diffraction and x-ray structural analyses. The microhardness (H_μ) and coefficient of friction (f) were measured by dry sliding using a ShKh-15 indenter.

The initial thin films (0.25 μm) had a NaCl fcc structure (Fig. 1a) with lattice parameter $a=4.24$ Å (in good agreement with the published data[1]), an average grain size of 2.8 μm, and a well-defined texture. This texture was obtained because for the electron diffraction analyses the films were deposited on freshly cleaved (100)-oriented sodium chloride. However, it may also be caused by the growth texture observed at these thicknesses.

After ion bombardment, the grain size of the TiN films remained almost constant. Some reduction in the lattice parameter to 4.225 Å and 4.205 Å was observed as a result of Ar^+ and B^+ ion bombardment, respectively. At the dose $\Phi=2\times10^{14}$ cm^{-2} some disordering of the grains is observed (Fig. 1b). Electron diffraction patterns obtained under general diffraction conditions revealed a decrease in the intensity of the texture maxima. This behavior occurs under implantation because high stresses are created in the target material by the implanted impurities and the formation of radiation defects. When the yield stress is reached, plastic deformation processes begin to take place, leading to the partial relaxation of these stresses. It was shown in Refs. 2 and 3 that for thin films the range $\Phi=10^{14}$–10^{15} cm^{-2} corresponds to inelastic deformation doses. However, in materials with different degrees of crystallinity, plastic deformation processes are not always manifest in the same way. In higher-quality crystals whose texture follows the directions of the slip system the grains may become misoriented, while in lower-quality crystals (Fig. 1c) the opposite process takes place, as is clearly illustrated in Fig. 1d. The grains become aligned in the direction of plastic deformation and the degree of texturing increases.

After bombardment of the films in this range of doses, the mechanical properties show some improvement. Figure 2 shows the dose dependences of the microhardness increment of TiN films. Since the depth of indentation exceeded the film thickness in the microhardness measurements, the experimental values of H_μ before and after ion bombardment correspond to the compound TiN-Al_2O_3. The following formula[4] was used to determine the true values of the microhardness of TiN:

$$H_\mu = H_c + (H_c - H_0)/[2(h/t) + 3(h/t)^2],$$

where H_c is the microhardness of the compound, H_0 is the microhardness of the substrate, measured at the same load, t is the film thickness, and h is the depth of indentation. Several sections can be identified on the $H_\mu(\Phi)$ curves for B^+ and Ar^+ implantation. An initial increase in H_μ is caused by the formation of point defects and isolated dislocations. For $\Phi>10^{14}$ cm^{-2} plastic deformation processes take place and ΔH_μ remains almost constant. An increase in the microhardness at doses above 10^{15} cm^{-2} is caused by the formation of stress fields from dislocation pileups. Bombardment with boron has a weaker hardening effect because of its lower atomic mass.

The coefficient of friction revealed a more complicated dependence on bombardment dose (Fig. 2). Over the entire range of doses, the coefficient of friction was higher than its initial value. However, its increase differed in different sec-

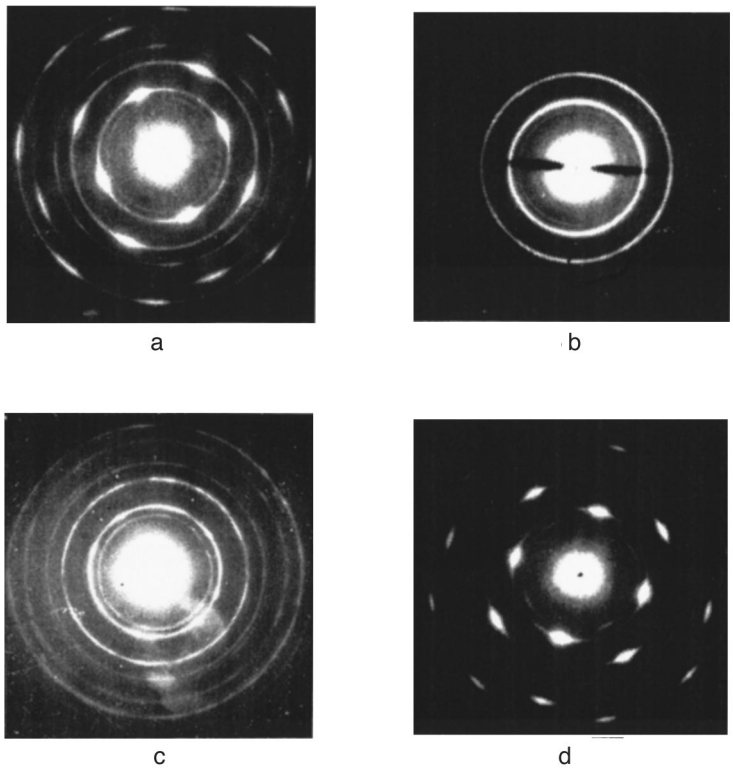

FIG. 1. Transmission electron-diffraction patterns (general diffraction) of TiN films bombarded by B^+ ions: a—before bombardment, b—$\Phi = 2\times10^{14}$ cm^{-2}, c—before bombardment, and d—$\Phi = 10^{15}$ cm^{-2}.

tions of the dose dependence. Since the radiation-induced hardening effect should help to reduce the coefficient of friction, any increase in f is probably caused by an increase in the average tangential stresses during contact between the indenter and the irradiated TiN coating. At the initial bombardment stage (10^{13}–10^{14} cm^{-2}) shear in the microcontact may be difficult because of the compressive stresses created by the radiation defects. In the range 10^{14}–10^{15} cm^{-2} where the microhardness increment is constant, the coefficient of friction increases at a greater rate because of plastic deformation processes accompanied by a reduction in the degree of texture (Fig. 1c). It is known that in fcc crystals plastic deformation takes place in the (111) planes. Since the grains in the irradiated TiN films are preferentially oriented in the (100) direction, which is unfavorable for shear under friction, this factor could be responsible for the increased values of the friction coefficient. In lower-quality crystals the degree of texturing is increased after bombardment, causing a decrease in the coefficient of friction. Thus, the repeated plastic deformation processes taking place under bombardment explain the multivalued dependence of f on the ion dose.

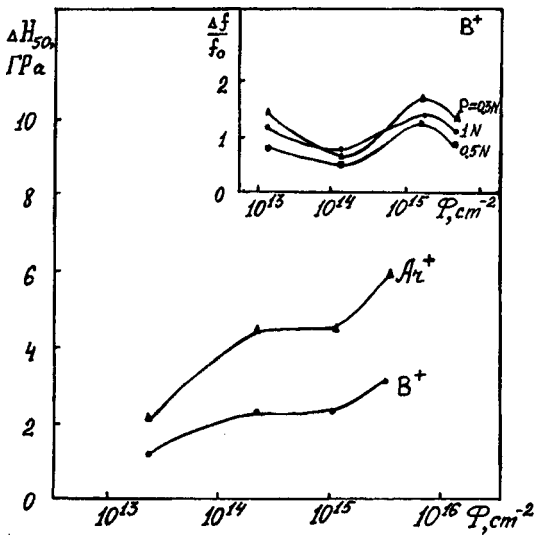

FIG. 2. Dose dependences of changes in microhardness (a) and coefficient of friction (b) of TiN films after bombardment.

These investigations have show that quasicontinuous ion beam implantation can be successfully used to modify the properties of wear-resistant TiN coatings. However, the wide range of structural changes accompanying the ion bombardment must be taken into account.

[1] L. I. Mirkin, *Handbook of X-Ray Analysis of Polycrystalline Materials* (Plenum Press, New York, 1964; Fizmatgiz, Moscow, 1961).
[2] A. P. Pavlov, D. I. Tetel'baum, E. V. Kuril'chik, and I. G. Romanov, Dokl. Akad. Nauk SSSR. **311**, 607 (1990) [Sov. Phys. Dokl. **35**, 275 (1990)].
[3] I. G. Romanov and A. L. Chekanov, Poverkhnost' No. 5, 40 (1993).
[4] G. G. Devyatykh, A. V. Gusev, A. M. Shiryaev *et al.*, Vys. Veshchestva No. 5–6, 167 (1992).
[5] I. V. Kragel'skiĭ and N. M. Mikhin, *Friction Components of Machines* [in Russian], Metallurgiya, Moscow (1984), p. 280.

Translated by R. M. Durham

Electronic spectrum of $Bi_2Sr_2CaCu_2O_8$ near the Fermi level from results of numerical calculations and ultraviolet (8.43 eV) photoelectron spectroscopy

A. M. Aprelev and A. A. Lisachenko

St. Petersburg State University, Physics Scientific-Research Institute
(Submitted June 26, 1997)
Pis'ma Zh. Tekh. Fiz. **24**, 69–74 (February 12, 1998)

The structure of the spectrum of the partial density of filled states of $Bi_2Sr_2CaCu_2O_8$ in the range $E_b<4$ eV, obtained by ultraviolet ($h\nu=8.43$ eV) photoelectron spectroscopy was compared with that calculated by the strong coupling method. The results of the calculations agree with the experimental results in the range of binding energies $1<E_b<4$ eV. Analysis of the evolution of the spectra under thermal and phototreatment in ultrahigh vacuum and in oxygen reveals that oxygen atoms from Cu–O planes possess the highest mobility in the lattice and the surface of the single crystal is formed by Bi–O planes. [S1063-7850(98)01302-0]

The properties of the normal and superconducting states of high-temperature superconducting cuprates are attributed to characteristics of their electronic structure and specifically to the energy spectrum of filled states near the Fermi level.[1]

In an earlier study[2] ultraviolet ($h\nu=8.43$ eV) photoelectron spectroscopy was used to identify and study the structure of the spectrum of filled states of $Bi_2Sr_2CaCu_2O_8$ near the Fermi level $E_b<4$ eV. An analysis of the *in situ* evolution of the spectrum during thermal and photoactivated treatments in vacuum and in oxygen revealed that the intensity of various peaks in this structure correlated with the oxygen concentration in the sample. This suggested that they may be genetically linked to hybridized oxygen orbitals. The difference between the photoelectron spectra obtained for different oxygen contents in the sample may be attributed to the partial density of single-particle states.

An important argument in support of these hypotheses would be that the difference between the experimental spectra obtained for different oxygen contents agreed with the calculated spectrum of the partial density of filled oxygen states. At the same time, this agreement would also indicate that the model and approximations used for the calculations are adequate. However, it is impossible to make a direct comparison between the experimental results[2] and the calculated results reported in the literature (see Ref. 3, for example) because only part of the Brillouin zone is probed in our experiments.

The aim of the present study is to calculate the partial density of filled oxygen states integrated over the experimentally probed part of the Brillouin zone and to compare the calculated results with the experiment.

Calculated and experimental results. To compare the experimental and calculated spectra, we need to take into account some characteristic features of the experiments. For instance, in our experiments[2] unusually soft radiation with the photon energy $h\nu=8.43$ eV is used to excite the photoemission. The photoelectrons emitted in a cone with an vertex angle of 34° and axis normal to the surface were recorded. Since the energy of an excited electron is comparable with the work function, the electron beam is strongly refracted at the surface barrier, which appreciably narrows the probed region in k-space. In addition, the use of an immersion objective system with a constant extraction potential[2] has the result that the size of the probed region depends on the electron binding energy in the initial state. From calculations made in Ref. 4, the spatial boundary of the region (E_b, k_x, k_y) is a surface of revolution with its axis normal to the surface (Fig. 1). Values of the quasimomentum as a percentage of the Brillouin zone of $Bi_2Sr_2CaCu_2O_8$ in the Γ–M direction are plotted on the abscissa. It can be seen from the figure that states in a region of k-space considerably smaller than the Brillouin zone (approximately 10% smaller) are probed in our photoemission experiments. Thus, it would be incorrect to compare the experimental spectra with the spectra of states integrated over the k-density reported in the literature. Thus, the densities of filled states were calculated with allowance for specific characteristics of the experiments reported in Ref. 2. The calculations were made by S. S. Nazin (Institute of Solid State Physics, Russian Academy of Sciences) using a semiempirical strong coupling method[5] which has proved highly successful in calculations of the electronic structure of $Bi_2Sr_2CuO_6$, $La_{1.85}Sr_{0.15}CuO_4$, $YBa_2Cu_3O_7$, and $Ti_2Ba_2CuO_6$ (Refs. 6 and 7).

The calculations were made for the body-centered cubic lattice of the tetragonal phase of $Bi_2Sr_2CaCu_2O_8$ compounds ($a=b=5.398$, $c=30.52$). The basis orbitals included the $6s^2$, $6p^3$, $5d^{10}$ Bi orbitals, $5s^2$, $5d$ Sr orbitals, $4s^2$, $4s$, $3d^{10}$ Cu orbitals, $2s$ and $2p$ oxygen orbitals, and $4d$ Ca orbitals. A detailed description of the calculation method is given in Refs. 6 and 7. The results of calculations of the partial density of states associated with oxygen and making an appreciable contribution in the binding energy range 0–6 eV are plotted in Fig. 2 (curves *1–3*). The states obtained by hybridization of oxygen orbitals with strontium, bismuth, and copper orbitals are situated in the O–Sr, O–Bi, and O–Cu planes, respectively. Each curve (Fig. 2, curves *1*, *2*,

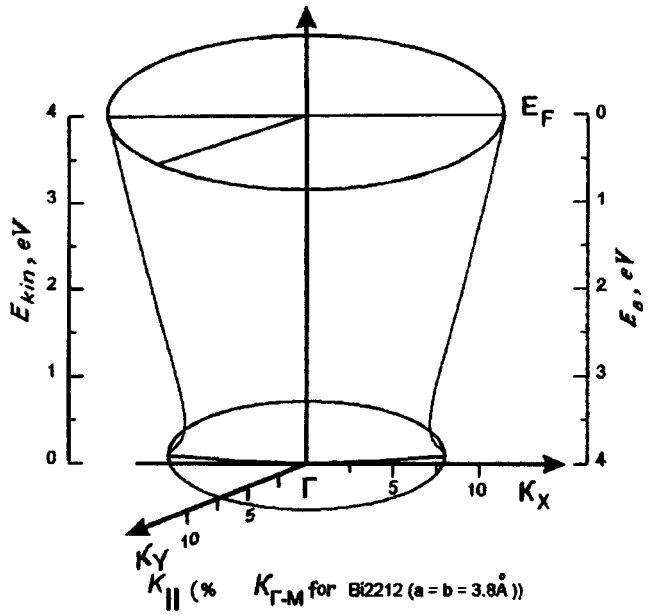

FIG. 1. Size of the k-region probed in the photoelectronic spectroscopy experiment ($h\nu = 8.43$ eV) as a function of the kinetic energy of the emitted electrons.

and *3*) exhibits some characteristic features: the partial density of O(Cu) states has two peaks at $E_b = 1.8$ and 2.8 eV, O(Bi) has a peak at 1.4 eV, and the density of O(Sr) states has a maximum at $E_b = 2.3$ eV.

The partial densities of filled electronic states were compared with the experimental difference spectra obtained for different treatments in ultrahigh vacuum and oxygen. The difference spectra were obtained by subtracting the spectrum of the sample before treatment from the photoelectronic spectrum after some particular treatment. In the range of binding energies $1 < E_b < 4$ eV, the position of the peaks of the calculated density of states formed by oxygen from

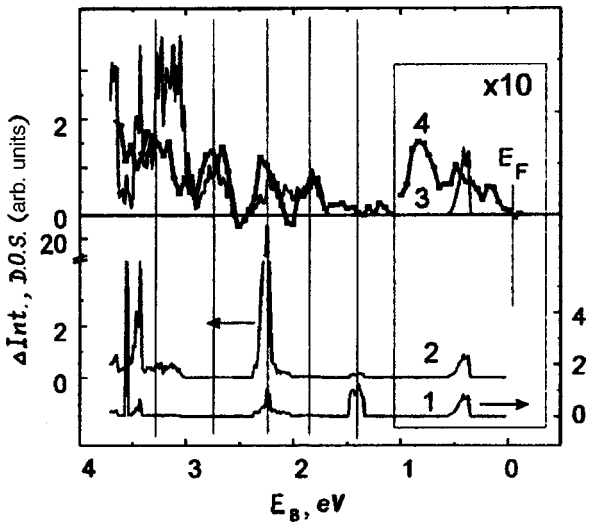

FIG. 2. Calculated spectra of the partial oxygen density of electronic states and experimental difference photoelectronic spectrum: *1–3*—calculated partial densities of electronic states for oxygen from the Sr–O, Bi–O, and Cu–O planes, respectively, and *4*—difference spectrum corresponding to heating between 77 and 300 K in ultrahigh vacuum.

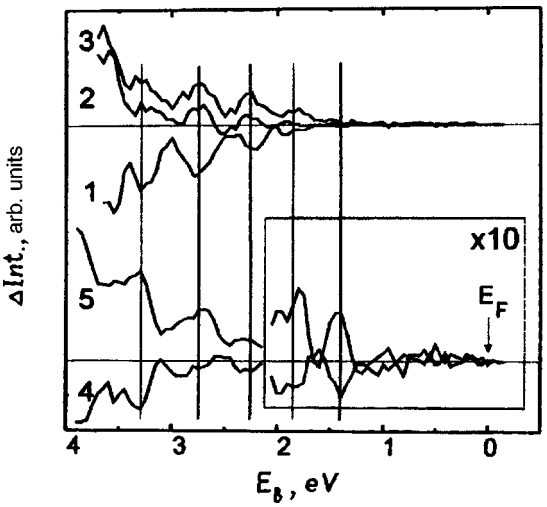

FIG. 3. Experimental photoelectronic difference spectra: *1–3*—difference spectra for heating in ultrahigh vacuum to 570 K—*1*, and in 0.5 Torr oxygen to 570 and 670 K—*2*, *3*; *4*, *5*—difference spectra obtained for illumination with the complete spectrum of a DRT-120 (0.05 W/cm^2) mercury lamp in ultrahigh vacuum and oxygen (0.5 Torr) for 30 min, respectively.

O–Cu planes is consistent with the difference spectra obtained for heating of a $Bi_2Sr_2CaCu_2O_8$ single crystal, cleaved in ultrahigh vacuum, from 77 to 300 K (Fig. 2, curve *4*), followed by heat treatment in ultrahigh vacuum and oxygen at 570 K and 670 K (Fig. 3, curves *1–3*). The experimental spectrum does not reveal any feature at $E_b = 1.5$ eV caused by the oxygen from Bi–O planes. In addition, the possible contribution to the experimental spectrum made by the oxygen orbitals from Sr–O planes is also small because the 2.3 eV peak is only negligibly higher than the 1.8 eV peak.

This result suggests that the electronic structure may be adequately described using the single-electron approximation in the binding energy range $1 < E_b < 4$ eV. It should be noted that, unlike the calculated partial (oxygen) density of filled electronic states in the range $0 < E_b < 4$ eV, the experimental photoelectronic spectrum has significant characteristics at 0.18 and 0.9 eV. This may be caused by the inadequacy of the model which does not take into account the carrier correlations and the nonuniformity of the oxygen distribution caused by interaction of oxygen vacancies with appreciable diffusion of oxygen in the lattice.[8,9]

A comparison between the intensity of the peaks in the experimental difference spectra (Fig. 1, curve *4* and Fig. 2, curves *1–3*) and the calculated spectra of filled states (Fig. 1, curves *1–3*) indicates that oxygen from the Cu–O plane has the highest mobility in the $Bi_2Sr_2CaCu_2O_8$ lattice and as a result of thermally activated oxygen depletion of the surface layer, new vacancies appear in Cu–O layers.

Unlike heat treatment, photoactivation gives rise to a characteristic in the spectrum at $E_b = 1.5$ eV (Fig. 2, curves *4* and *5*). This experimental observation may be attributed to an increase in the relative contribution made by oxygen from the Bi–O plane to photoactivation of oxygen exchange between the sample and the gas phase. This may involve the photoactivated desorption (adsorption) of oxygen, bearing in mind that for cleaved $Bi_2Sr_2CaCu_2O_8$ single crystals, the boundary with vacuum is formed by the Bi–O plane.

The authors would like to thank S. S. Nazin for making the calculations, and Professor V. A. Grazhulis and A. M. Ionov for fruitful discussions.

This work was carried out as part of the ''Surface Atomic Structures'' Federal Program (Project No. 95-1.14) and the Research Program of the State Committee for Higher Education in the Fundamental Natural Sciences (Project No. 95-07 100-164).

[1] Z.-X. Shen and D. S. Dessau, Phys. Rep. **253**, 3 (1995).
[2] A. M. Aprelev, V. A. Grazhulis, A. M. Ionov, and A. A. Lisachenko, Physica C **235–240**, 1015 (1994).
[3] E. Z. Kurmaev and L. D. Finkelstein, Int. J. Mod. Phys. B **5**, 1097 (1991).
[4] A. M. Aprelev, Thesis for Candidates's Degree [in Russian], St. Petersburg State University (1997).
[5] W. Harrison, *Electronic Structure and the Properties of Solids* (Freeman, San Francisco, 1980; Mir, Moscow, 1983).
[6] S. V. Meshkov, S. N. Molotkov, S. S. Nazin, I. S. Smirnova, and V. V. Tatarskii, Physica C **161**, 497 (1989).
[7] S. V. Meshkov, S. N. Molotkov, S. S. Nazin, I. S. Smirnova, and V. V. Tatarskii, Physica C **172**, 149 (1990).
[8] D. D. Sarma, S. R. Barman, H. Kajueter, and G. Kotliar, Cond-Mat/9609259.
[9] A. Fujimori, I. Hase, M. Nakamura *et al.*, Phys. Rev. B **46**, 9841 (1992).

Translated by R. M. Durham

Influence of changes in the density of a solid on the diffusion mobility of atoms under bombardment by high-power nanosecond charged particle beams

G. A. Bleĭkher, V. P. Krivobokov, O. V. Pashchenko, and S. N. Yanin

Nuclear Physics Scientific-Research Institute, Tomsk
(Submitted July 23, 1997)
Pis'ma Zh. Tekh. Fiz. **24**, 75–79 (February 12, 1998)

A theoretical analysis is made of the behavior of the diffusion coefficient of a metal having a nonequilibrium density as a result of the action of high-power nanosecond radiation fluxes. It is shown that a reduction in the density of the sample as a result of thermomechanical processes substantially increases the diffusion mobility of the atoms. © *1998 American Institute of Physics.* [S1063-7850(98)01402-5]

In experiments to study the mixing of thin films under the action of high-power nanosecond energy fluxes, it has been observed that the atoms exhibit extremely high mobility with effective diffusion coefficients of $10^{-2}-10^{-4}$ cm^2/s, which is several orders of magnitude higher than the diffusion coefficients in liquid metals. This effect was identified for ion beams (Ref. 1, for example), electron beams,[2] and also for pulsed laser radiation.[3]

Various mechanisms of atomic migration have been considered to explain this effect, such as diffusion and thermal diffusion in the molten surface layer of the sample, hydrodynamic mixing, and impurity segregation in a moving solidification front.[4] This cannot be regarded as an exhaustive list, however, and calculations of atomic transport based on these mechanisms usually give results lower than those obtained experimentally. There is thus a need to search for other mechanisms for the transport of material under the action of concentrated pulsed radiation fluxes.

The action of high-power nanosecond beams stimulates intensive thermomechanical processes in a solid, as a result of which the material has a density ρ differing from the normal value ρ_0 by between a few and tens of percent for microseconds or even milliseconds[5] (Fig. 1). This change in density should cause changes in the diffusion characteristics of the material. Here we make a theoretical study of the behavior of the diffusion coefficient of a liquid metal under conditions of nonequilibrium density.

To this end, we carried out molecular dynamics modeling of the diffusion processes, taking the self-diffusion of aluminum as an example.

We used the interatomic interaction potential obtained by the pseudopotential method using Heine–Abarenkova–Animalu form factors. The crystallite calculated was a cube consisting of $N=2048$ mobile atoms. Periodic boundary conditions were set at all faces. The temperature dependence of the fcc lattice constant of aluminum in the temperature range 1000–2500 K was determined by the expression $a(T)=a(T_{\rm mp})^3\sqrt{1+\beta(T-T_{\rm mp})}$, where $T_{\rm mp}=934$ K is the melting point and $\beta=0.113\times10^{-3}$ 1/K is the volume coefficient of expansion. The lattice constant at the melting point $a(T_{\rm mp})$ was calculated for this potential by using an artificial damping method and was 0.42456 nm, which corresponds to density $\rho_0(T_{\rm mp})=2.362$ g/cm^2. For a given temperature T the atoms were assigned velocities consistent with a Maxwellian distribution. The equations of motion for the atoms were then solved before the establishment of statistical equilibrium between the potential and kinetic energies of the system ($\sim10^{-13}$ s). Only then did we begin to calculate the diffusion characteristics.

In the modeling process we calculated the mean square atomic displacement

$$\langle R^2\rangle=\frac{1}{N}\sum_{i=1}^{N}(R_i(t)-R_0(0))^2,$$

where $R_i(t)$ is the position of the ith atom at time t. The dependence $\langle R^2(t)\rangle$ becomes linear within approximately 10^{-12} s, so that the diffusion coefficient D can be calculated using the formula

$$D=\langle R^2\rangle/6t.$$

To check the model, calculations were first made for the equilibrium density of liquid aluminum. The values obtained for the self-diffusion coefficient of liquid aluminum (see Fig. 2 and Table I) agree with the experimental data,[6] which indicates that this model is accurate.

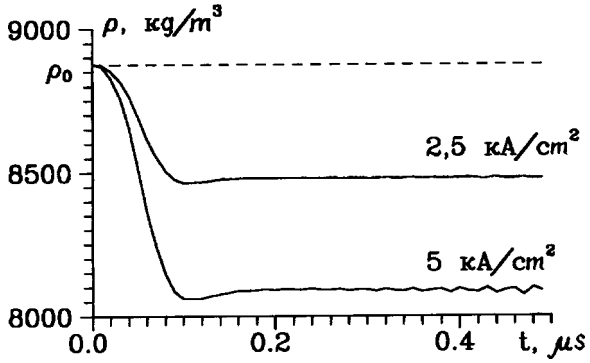

FIG. 1. Evolution of the density near the surface of a copper sample bombarded by a 0.5 MeV electron beam with a pulse length of 100 ns at different current densities.

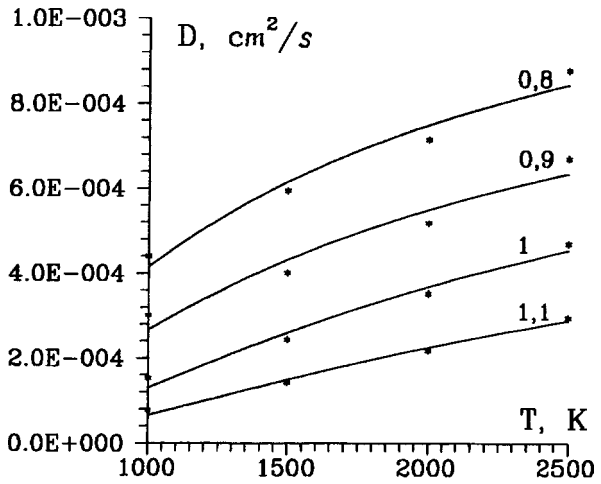

FIG. 2. Coefficient of self-diffusion of liquid aluminum versus temperature and density calculated using the molecular dynamics method.

Results of calculating the diffusion coefficient of aluminum for various temperatures and densities are plotted in Fig. 2. The asterisks indicate the points obtained by the molecular dynamics modeling, while the solid curves give a least-squares fit using the Arrhenius expression

$$D(T)=D_0\ \exp\left(-\frac{E_a}{kT}\right),$$

where D_0 is the preexponential factor and E_a is the diffusion activation energy (see Table I).

TABLE I. Preexponential factor and diffusion activation energy as a function of aluminum density calculated using results of molecular dynamics modeling.

ρ/ρ_0	D_0, cm^2/s	E_a, eV
0.8	1.36×10^{-3}	0.102
0.9	1.13×10^{-3}	0.125
1.0	1.05×10^{-3}	0.180
1.1	7.76×10^{-4}	0.213

Thus, these results indicate that the reduction in the density of an irradiated sample caused by thermomechanical processes substantially increases the diffusion mobility of the atoms, mainly as a result of a decrease in the diffusion activation energy. Since the material at the surface is in a rarefied state for microseconds or milliseconds,[2] this mechanism makes a significant contribution to the increased diffusion and thermal diffusion fluxes, which are proportional to the diffusion coefficient.

To sum up, we can affirm that the transport of atoms at the surface of a solid exposed to high-power nanosecond radiation fluxes is a complicated process which involves several mechanisms. Only detailed allowance for all these transport mechanisms can yield a mathematical model which provides a quantitative description of this effect.

[1] A. N. Didenko and V. P. Krivobokov, Zh. Tekh. Fiz. **58**, 2002 (1988) [Sov. Phys. Tech. Phys. **33**, 1214 (1988)].
[2] G. Battaglin, A. Carnera, L. F. Donà dalle Rose, P. Mazzoldi, E. d'Anna, G. Leggieri, and A. Luches, Thin Solid Films **145**, 147 (1986).
[3] A. Miotello, L. F. Donà dalle Rose, and A. Desalvo, Appl. Phys. Lett. **40**, 135 (1982).
[4] V. P. Krivobokov, O. V. Pashchenko, and G. A. Sapul'skaya, Zh. Tekh. Fiz. **64**(5), 37 (1994) [Tech. Phys. **39**, 475 (1994)].
[5] V. P. Krivobokov, O. V. Pashchenko, and G. A. Sapul'skaya, Izv. Vyssh. Uchebn. Zaved. Fiz. No. **12**, 37 (1993).
[6] D. R. Wilson, *Structure of Liquid Metals and Alloys* [Russ. transl.], Metallurgiya, Moscow (1972).

Translated by R. M. Durham

Structural transition and its governing laws

G. E. Skvortsov

St. Petersburg State University
(Submitted September 24, 1997)
Pis'ma Zh. Tekh. Fiz. **24**, 80–85 (February 12, 1998)

An analysis is made of the phenomenon of structural transition which generalizes the phase transition concept and encompasses structures of all levels and strong nonequilibrium. The main properties, the laws governing structural transitions, and the effects caused by them are indicated. A simple model is proposed to describe structural transition and is used to analyze various nonequilibrium transitions. © *1998 American Institute of Physics.*
[S1063-7850(98)01502-X]

Some laws governing highly nonequilibrium processes were identified and discussed in Refs. 1–4. The present paper examines the application of these laws to the phenomenon of structural transition.

The genetic link between structural transition and instability[3] is used to establish the main properties and laws governing a transition. The analysis is made using extremum principles characteristic of structural transition, which differ from equilibrium laws. A simple, effective model is proposed to describe quasisteady-state structural transitions (ranging from the transition to turbulence to the transition to superconductivity).

1. A structural transition is a macroscopically observable process with a substantial change where an object, the system $O_1[S_1]$ having the structure S_1, is transformed as a result of the action to give $O_2[S_2]$.

The numerous structural transitions include quasiequilibrium phase transitions,[5] many-particle nuclear-atomic disintegration processes, chemical reactions, and macrostructural transformations.

The structure of an object consists of a hierarchical system of substructures of levels $S=1,2\ldots$ and is defined by the sequence of sets

$$\{\lambda_s,\tau_s,\varepsilon_s,n_s;m_s,\lambda_{s+1},\tau_{s+1},\varepsilon_{s+1}\}, \tag{1}$$

where the first three quantities are the space, time, and energy characteristics of the coupling between the structure-kinetic elements (fluctons) of level S, n_s is their number density, and the last four quantities are the parameters of the structural elements. The definitions of these quantities and the relations between them for the s and $s+1$ levels are given in Ref. 4.

Most structural transitions can be included in a system with three levels: macroscopic fluctons ($s=1$), macromolecular globules (2), and atomic molecular clusters (3).

The energy model of a multilevel sequence of structural transitions may be represented with allowance for the laws given in Refs. 2–4, by an expression for the resonant departure from equilibrium

$$\text{res}=\sum_{s=1}\left[1+\left(\frac{\varepsilon_s}{\varepsilon_1}\right)^r\left(\frac{e-\varepsilon_s}{\varepsilon_1}\right)^{l_\pm}\right]^{-1}. \tag{2}$$

Here e is the energy acting on a structural element, and $l_\pm$ determines the ''analytic form'' of the structural element in terms of energy as ε_s is approached from the right and from the left (hysteresis). The spectrum $\varepsilon_s=sT_0$, $T_0=12.5$ K considered in Ref. 6 may be taken as ε_s and most of the results of Ref. 6 can be described, including the ''devil's staircase,'' by suitably selecting r and $l_\pm$.

Expression (2) allows for the extremum property of a structural transition: max res for $e\simeq\varepsilon_s$ corresponds to the initial stage of the transition process. The extremum dependence in terms of the departure from equilibrium is attributable to the threshold processes of activation of the internal degrees characteristic of structural transitions. Note that min res corresponds to the stable structure S_2.

2. A genetic link between the phenomenon of structural transition and instability was identified in Ref. 3: a structural transition accompanies instability while in a system with a large number of degrees, instability is generally caused by structural transition.

This link can be used to specify new criteria for structural transition, to give a suitable classification, and to make a dynamic analysis of structural transition.

The criteria for structural transition consistent with this link are all general instability criteria,[7] i.e., rate, bifurcation, and balance criteria.

These three types of criteria reflect different aspects of the structural transition phenomenon. In its quasisteady-state form, the rate criterion reflects the activation slowing of the rate at the initial stage of the structural transition, whereas in its abruptly increasing form it indicates the concluding stage of destruction of the initial structure. The bifurcation criterion reflects the appearance of various possible results of the structural transition, i.e., the ''creation'' property. This is caused by the inherent instability of a large reaction to small perturbations. The balance criterion indicates that the action of the system coupling and the external action preceding the structural transition are equal.

When the structural transition is accomplished by means of a controllable action, such as a linear increase with time, $g=g_0t$, in accordance with the relation

$$d_t\Phi(g(t))=d_g\Phi(g)g_0, \tag{3}$$

the bifurcation-jump singularities of the determining quantity $\Phi(g)$ coincide with singularities in the time analysis.

The general balance criterion[7]

$$\partial_t A = g_+[A] - g_-[A], \quad g_+[A] = g_-[A] \tag{4}$$

in its simplest form gives an approximate criterion for structural transition, namely, that the active departure from equilibrium equal unity.[2,3]

Note that reliable experimental criteria for structural transitions are singularities of structure-dependent quantities, such as electromagnetic susceptibilities, taking the form of kinks, peaks, and jumps.[6]

We observe that the Landau theory[8] with allowance for the choice of free energy, is essentially a bifurcation theory (catastrophe).

3. The familiar classification of structural transition as being indicated by a jump, reflecting some singularities associated with the structural transition, neglects some important characteristics.

We give a classification of structural transition according to natural indications. As the most suitable we take these indications of a $1 \rightarrow 2$ transition:

$$S_1 \rightarrow S_2, \quad \Delta E = \frac{\varepsilon_2 - \varepsilon_1}{\varepsilon_1}, \quad \Delta\Pi = \frac{\Pi_2 - \Pi_1}{\Pi_1},$$

$$H_{12} = \tau_{12}\left|\frac{\partial \overline{g}}{\partial t}\right|, \tag{5}$$

$s_{1,2}$ are the primary structural characteristics, ΔE is the energy effect of the structural transition, $\Pi_{1,2}$ are the values of the structure-dependent quantities, τ_{12} is the required transition time, and H_{12} is the rate parameter.

For the first indication, in a three-level structure there are clearly nine kinds of structural transition. The other three indications are best classified according to three gradations, corresponding to low, moderate, and high values of ΔE, $\Delta\Pi$, and H_{12}.

The first type include quasi-equilibrium phase transitions, while the last type include explosive structural transitions, ultrafast compression of solids, and the formation of the elements.

It is useful to bear in mind the link between the type of structural transition and the characteristic of its accompanying instability: soft and hard regimes for structural transitions of the second and first kind, a self-oscillatory regime for structural transitions of the second kind, positive feedback for explosive structural transitions, and so on.

4. By applying the laws given in Refs. 2–4 and the extremum laws, it is possible to obtain a simple description of the first type of structural transition. Its form is similar to the van der Waals theory (Ref. 8, p. 549) but it has a fundamental basis and a wide range of validity.

The initial quantities of interest are the fluxes and forces, which for a structural transition of the first kind are functions of a set of departures from equilibrium $\{g_m\}$ and have the form

$$\Phi_n(g) = \sum_m B_{nm}(g) g_m. \tag{6}$$

The determining relations (6) should reflect the laws of qualitative boundary, abnormality, and alternation of nonequilibrium.

For the case of a single action and state parameter p, a simple dependence satisfying these laws and giving an acceptable interpolation in the structural transition region has the form

$$\Phi(x,p) = a_1\left(\frac{1}{3}x^3 - a_2x^2 + a_3x\right) + a_4 \equiv a_1 B(x)x + a_4,$$

$$a_1 = \frac{6(\Phi_1 - \Phi_2)}{(x_2 - x_1)^3}, \quad a_2 = \frac{x_1 + x_2}{2} \equiv \overline{x}, \quad a_3 = x_1 x_2,$$

$$a_4 = \Phi_1 - a_1 B_1 x_1. \tag{7}$$

Here $\Phi(x)$, $x = g/g_1$ are quantities normalized relative to the initial boundary of the structural transition: $\Phi(x_1 = 1) = 1$, $x_{1,2}$ are the zeros of the functions $\Phi'(x)$, and x_2 is the final boundary of the structural transition.

The function $\Phi(x)$ gives an N-shaped curve in the structural transition region which is essentially universal: an increase represents the normal reaction of the structure S_1, max Φ at x_1 represents the onset of structural transition, a decrease—an anomalous reaction of the ''mixture''—represents a transition from S_1 to S_2, min Φ at x_2 represents the end of the structural transition, and an increase represents the normal reaction of S_2.

The region of anomalous behavior $\Phi' < 0$, $x_1 < x < x_2$ is characterized by the evolution of fluctuations (instability) to the higher level at $\Phi''(\overline{x}) = 0$.

The problem as to how abruptly the quantities vary during a structural transition in the model (7) is as follows. According to the model (7), the values of $\Phi(g)$ have the greatest abruptness in the transition process $|\Phi'(\overline{x})| = 3(\Phi_1 - \Phi_2)/2(x_2 - x_1)$. If the abruptness is small, then if Φ is used as the control parameter, the values of $g(\Phi)$ will undergo a jump: $\Delta g = g_1 - g_2$, $\Phi_{\min} < \Phi < \Phi_{\max}$.

The critical point evidently corresponds to the condition $g_1 = g_2$.

The proposed model of structural transition can be used to describe a wide range of phenomena, and also sequences of structural transitions if an additive modification is used (see formula (2)).

5. The description of various structural transitions using this model is considered.

5.1. Boiling regime, data from Ref. 9, p. 158. The determining quantity is the heat flux

$$\overline{q}(\tau) = \frac{q(\tau)}{q_1}, \quad q_1 = q(\Delta_1 T), \quad \tau = \frac{\Delta T}{\Delta_1 T};$$

$$\Delta_1 T = 19 \text{ K}; \quad q_1 = 8.5 \times 10^5 \text{ W/m}^2, \quad \Delta_2 T = 280,$$

$$q_2 = 10^5.$$

In accordance with the model (7), we have

$$a_1 = 0.00206, \quad a_2 = 7.85, \quad a_3 = 14.7,$$

$$a_4 = 0.985; \quad \overline{q}'(\overline{\tau}) = -0.097. \tag{8}$$

In the transition to the metastable region a temperature jump will take place (and be observed) because of the small abruptness of q.

5.2. Anomalous relaxation in shock waves; data from Ref. 10, p. 134, Fig. 19. The determining quantity is the density behind the shock wave front

$$\rho(m)=\frac{\rho_2}{\rho_{c1}},\quad m=\frac{M_s}{M_{s1}};\quad M_{s1}=10.8,\quad M_{s2}=12.2;$$

$$p_1=0.01\text{ mm},\quad \rho_{c1}=11.9,\quad \rho_{c2}=11.4.$$

We have

$$a_4=114,\quad a_2=1.07,\quad a_3=1.13,\quad a_4=-44.6;$$

$$\rho'(\overline{m})=-0.6. \tag{9}$$

This transition, according to the physical mechanism of anomalous relaxation,[11] takes place from level 3 to level 1.

The model indicates a jump in M_s which corresponds to the observed bifurcation of the shock wave.[11]

It should be noted that the data from Ref. 12, p. 318, Fig. 19 demonstrate the existence of anomalous relaxation at 4.2–5 km/s for 1 atm, and also a weaker singularity at a shock wave velocity of 2 km/s.

It is interesting to note that strong shock wave singularities are indicated in condensed media (Ref. 12, p. 311); these are presumably caused by anomalous relaxation (see Ref. 3).

5.3./ Transition to turbulence (Ref. 9, p. 21). The determining quantity is the reciprocal drag coefficient

$$\xi(r)=\frac{\varphi_1}{\varphi},\quad r=\frac{\mathrm{Re}}{\mathrm{Re}_1};\quad \mathrm{Re}_{1,2}=2.5,\ 4\times10^4,$$

$$\varphi_{1,2}=0.03,\ 0.04.$$

We have

$$a_1=6.94,\quad a_2=1.3,\quad a_3=1.6,\quad a_4=-3.4;$$

$$\xi'(\overline{r})=-0.6. \tag{10}$$

With increasing pressure, a jump in flow rate should occur at the beginning of the transition to turbulence.

Among the many existing commentaries on this work, it is merely noted that these examples and other data indicate that transient metastable states are realistic (in the van der Waals model they are generally eliminated as unrealizable). Moreover, by suitably using these states, we can obtain cycles of energy conversion of the second kind.

[1] G. E. Skvortsov, Pis'ma Zh. Tekh. Fiz. **16**(17), 15 (1990) [Sov. Tech. Phys. Lett. **16**, 647 (1990)].
[2] G. E. Skvortsov, Pis'ma Zh. Tekh. Fiz. **23**(6), 85 (1997) [Tech. Phys. Lett. **23**, 246 (1997)].
[3] G. E. Skvortsov, Pis'ma Zh. Tekh. Fiz. **23**(7), 23 (1997) [Tech. Phys. Lett. **23**, 261 (1997)].
[4] G. E. Skvortsov, Pis'ma Zh. Tekh. Fiz. **23**(10), 17 (1997) [Tech. Phys. Lett. **23**, 383 (1997)].
[5] Yu. F. Gufan, *Structural Phase Transitions* [in Russian], Moscow (1982).
[6] *Systems of Singular Temperature Points of Solids* [in Russian], Moscow (1986).
[7] E. N. Perevoznikov and G. E. Skvortsov, Zh. Tekh. Fiz. **52**, 2353 (1982) [Sov. Phys. Tech. Phys. **27**, 1451 (1982)].
[8] L. D. Landau and E. M. Lifshitz, *Statistical Physics*, Part 1, 3rd ed. (Pergamon Press, Oxford, 1977; 4th ed., Nauka, Moscow, 1976).
[9] S. S. Kutateladze, *Analysis of Similarity and Physical Models* [in Russian], Novosibirsk (1986).
[10] *Physics of Fast Processes*, Vol. 3 [in Russian], Moscow (1971).
[11] G. I. Minin, A. P. Bedin, N. I. Yushchenkova, G. E. Skvortsov, and A. P. Ryazin, Zh. Tekh. Fiz. **51**, 2315 (1981) [Sov. Phys. Tech. Phys. **26**, 1363 (1981)].
[12] *Physics of High-Speed Processes*, Vol. 2 [in Russian], Moscow (1971).

Translated by R. M. Durham

Possible transport of an electron beam with above-limit current in a vacuum channel with plasma partitions

A. E. Dubinov, V. D. Selemir, and A. V. Sudovtsov

Russian Federal Nuclear Center—All-Russian Scientific Research Institute of Experimental Physics, Sarov (Arzamas-16)

(Submitted May 22, 1997)
Pis'ma Zh. Tekh. Fiz. **24**, 86–90 (February 12, 1998)

Computer modeling by the particle-in-cell method is used to demonstrate that a high-current electron beam with an above-limit current can be transported in a vacuum channel with plasma partitions, whereas without these partitions a virtual cathode forms, blocking the channel.
 [S1063-7850(98)01602-4]

Many scientific and technical applications require energy to be transferred in the form of high-current electron beams over large distances without appreciable losses. To this end, evacuated transport channels with a magnetically guided beam are being developed.[1]

However, the transport channel described in Ref. 1 has a fundamental constraint on the current which can be transported,[2] above which a virtual cathode forms and blocks the channel.

An original solution designed to increase the transportable current above the existing limit was proposed in Ref. 3. This solution essentially involves dividing the channel into sections and separating them with electrically conducting films, foils, or grids whose thickness is less than the mean free path.

Note that this channel need not contain a magnetic beam-guiding system. Since the conducting film (foil, grid) shunts the radial defocusing electric field of the beam in its vicinity, only magnetic focusing forces act on the electrons near the film as a result of the self-induced magnetic field of the beam, obviating the need for external focusing. However, this channel may also be used with a magnetic system.

A disadvantage of this type of transport channel[3] is the strong angular scattering of electrons by atoms from the film (foil, grid) which leads to losses of beam electrons and reduces the transport efficiency. In addition, thin films are not sufficiently long-lived and become damaged after a few electron current pulses.

Theoretical and experimental investigations which we carried out to develop microwave generators with a virtual cathode, in which a thin plasma sheet is used as the anode,[4,5] led us to the idea of replacing the thin films and foils in transport channels with thin plasma partitions. However, this solution needs to be checked to determine whether beam or beam–plasma instabilities occur in the channel and disrupt the transport process.

To this end we carried out computer modeling of a channel with plasma partitions, for which we used the 2.5-dimensional version of the well known Karat code[6] based on a completely self-consistent PIC code.

The transport channel was formed by a planar waveguide 30 cm long and 10 cm wide to which a strong longitudinal magnetic field of 50 kG was applied. An electron beam with a linear current density of 400 A/cm and an electron energy of 0.5 MeV was injected into the waveguide.

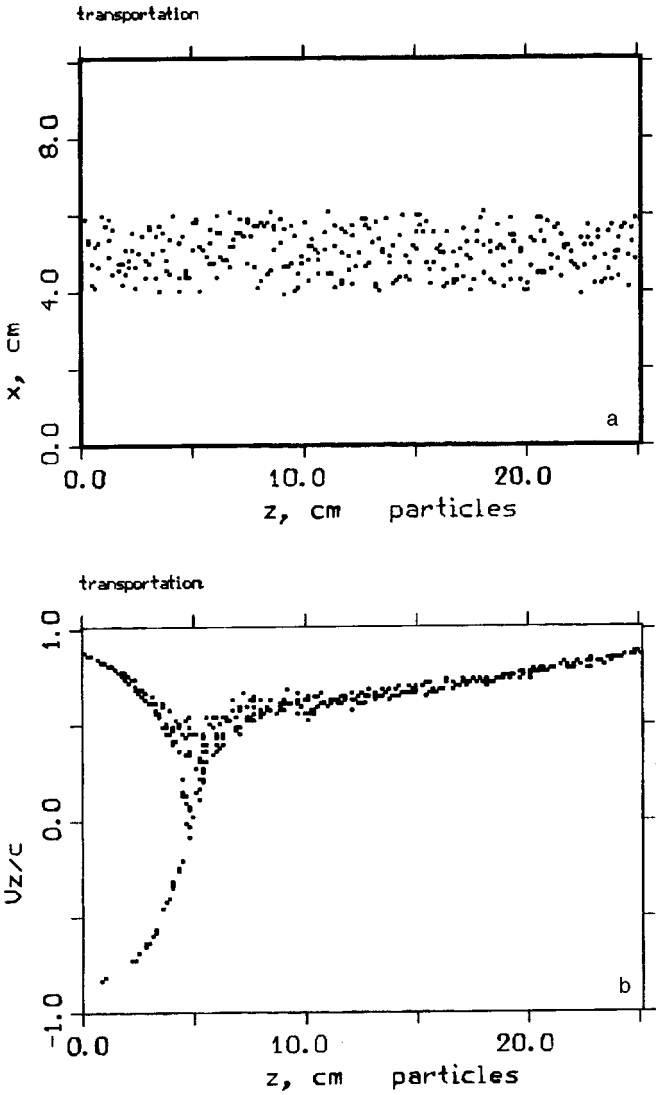

FIG. 1. Results of modeling for a free channel: a—channel geometry with beam, b—phase portrait.

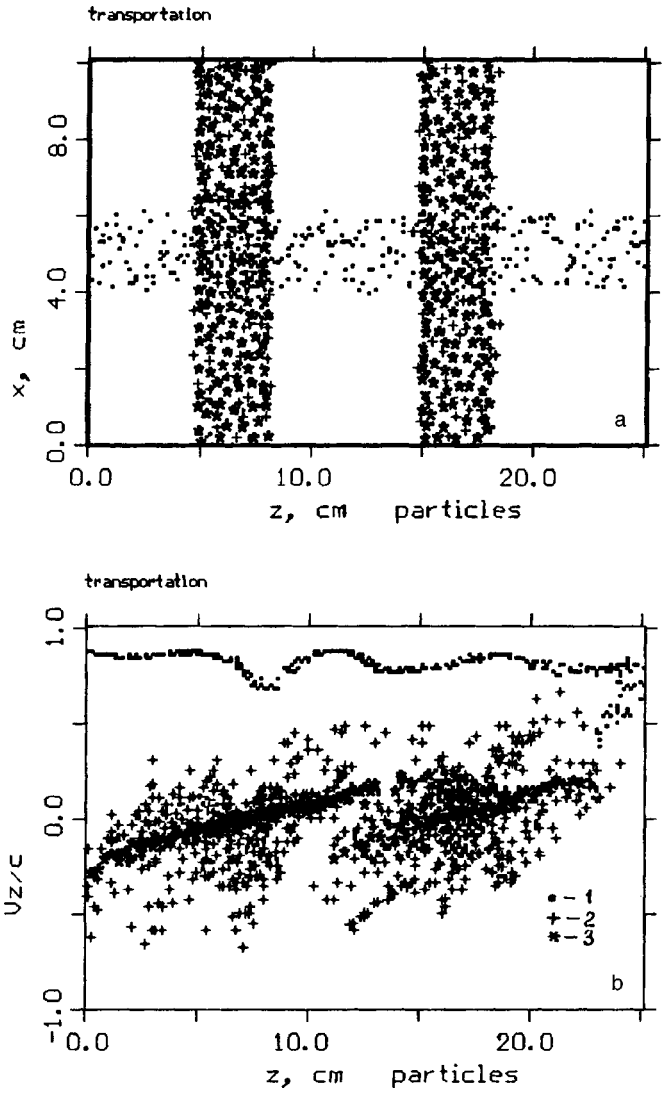

FIG. 2. Results of modeling for a channel with plasma partitions: a—channel geometry with beam and plasma partitions; b—phase portrait; *1*—beam electrons, *2*—plasma electrons, and *3*—plasma ions.

Two situations were modeled: a free waveguide and a waveguide loaded with two plasma partitions, 3 cm thick, each containing a plasma density of 5×10^{11} cm^{-3}. The results of the modeling are plotted in Figs. 1 and 2, respectively.

It was found that in the absence of the plasma partitions, a virtual cathode forms in the channel (Fig. 1b), which indicates that the electron current is above the limit for this waveguide.

With the plasma partitions in the channel, the electron beam propagates completely through the waveguide, without forming a virtual cathode (Fig. 2b).

Thus, it has been established that a transport channel loaded with plasma partitions can transmit electron beams with above-limit currents without appreciable losses.

However, it should be borne in mind that an electron beam entrains positive plasma ions in the collective motion, which may be useful for accelerating ion beams. In this case, and also if a pure electron beam is required, a magnetic particle separator can be installed at the exit from the transport channel.

This work was carried out as part of the Russian Fund for Fundamental Research, Project No. 96-02-17047a.

The authors would like to thank V. P. Tarakanov for consultation on the use of the Karat code.

[1] V. V. Chikunov, B. A. Knyasev, P. I. Melnikov, in *Proceedings of the XIIIth International Symposium on Discharges and Electrical Insulation in Vacuum*. Paris, 1988, p. 436.
[2] L. S. Bogdankevich and A. A. Rukhadze, Usp. Fiz. Nauk **103**, 609 (1971) [Sov. Phys. Usp. **14**, 163 (1971)].
[3] R. J. Adler, B. Sabol, and G. F. Kiuttu, IEEE Trans. Nucl. Sci. **NS-30**, 3198 (1983).
[4] A. L. Babkin, A. E. Dubinov, V. G. Kornilov *et al.*, Russian Patent No. 2046440 published 8.06.93, Int Cl.: H 01 J 25/00; Byull. Izobret. No. 29, (1995).
[5] A. L. Babkin, A. E. Dubinov, V. S. Zhdanov *et al.*, Fiz. Plazmy **23**, 343 (1997) [Plasma Phys. Rep. **23**, 316 (1997)].
[6] V. P. Tarakanov, *User's manual for code Karat*, Berkley Research Associates Inc, Springfield, VA, (1992).

Translated by R. M. Durham

Photolytic properties of a pulsed discharge in water

V. L. Goryachev, F. G. Rutberg, and A. A. Ufimtsev

Institute of Problems in Electrophysics, Russian Academy of Sciences, St. Petersburg
(Submitted August 18, 1997)
Pis'ma Zh. Tekh. Fiz. **24**, 91–95 (February 12, 1998)

Results are presented of an experimental investigation of the photolytic properties of a pulsed discharge in water. A model is proposed for this process which satisfactorily describes the dependence of the hydrogen peroxide concentration on the specific discharge energy. © *1998 American Institute of Physics.* [S1063-7850(98)01702-9]

It has been established that, regardless of the single-pulse energy, pulsed discharges in water have the capacity to cleanse water of bacterial and chemical contamination.[1,2] These discharge properties are now beginning to be used in various water purification technologies under industrial conditions. However, the physical mechanisms responsible for the action of a discharge in water on microorganisms and organic and inorganic substances present in the water are by no means clear. This particularly applies to the long-term maintenance of the bactericidal properties of water treated with electric discharges. Since the plasma column of a pulsed discharge in water has a temperature $T=(10-20)\times 10^3$ K (Ref. 3) and pressure $P=10^7-10^9$ Pa, it is logical to assume that it is a powerful pulsed emitter of ultraviolet radiation. The fraction of radiation in the wavelength range $\lambda=100-200$ nm may be very appreciable and this part of the electromagnetic radiation spectrum absorbed by water causes a photolysis reaction:[4,5]

$$H_2O+h\nu\rightarrow(H_2O)^*\rightarrow H+OH.$$

The concentration of product hydrogen or hydrogen peroxide (H_2O_2) can serve as a quantitative measure of this reaction.

Here, the intensity of the photolysis process caused by a pulsed discharge in water is estimated from the measured H_2O_2 concentration in the water after treatment with a pulse-periodic discharge.

The investigation was carried out using apparatus described in Ref. 6. The discharge took place in a cylindrical cell 50 mm in diameter using point-plane electrodes. The average specific input energy was varied by varying the number of pulsed discharges. The single-pulse energy was determined from measurements of the voltage and current. The pulse repetition frequency was 0.5 Hz. Under these conditions the water was efficiently mixed by the pressure pulses excited by the discharge. The H_2O_2 concentration was determined by titration in the analytical laboratory of the Applied Chemistry Russian Scientific Center. The experiments were carried out using distilled and ordinary (tap) water.

The results of the measurements are plotted in Fig. 1, which gives the mass concentration of H_2O_2 as a function of the average specific energy deposited in the water by the electric discharge. It can be seen that the qualitative behavior for the distilled and tap water is the same. Similar curves were obtained in Ref. 4 for the hydrogen concentration formed as a result of the ultraviolet irradiation of water. It was established that the presence of impurities in the water substantially reduces the H_2O_2 concentration, as is observed in our experiments, where the H_2O_2 concentration in tap water is lower than that in distilled water. The experimentally determined dependence of the H_2O_2 concentration on the deposited energy reflects the characteristic features of photolysis induced by a source of electromagnetic radiation having a continuous or near-continuous absolute black-body radiation spectrum at $T=(1-2)\times 10^4$ K. At these temperatures the intensity of the ultraviolet radiation in the range 100–300 nm contains an appreciable fraction of the entire spectrum. Since ultraviolet radiation in the range 100–200 nm is absorbed, leading to the formation of hydrogen peroxide,[4,5] and 200–300 nm photons are strongly absorbed by H_2O_2 molecules,[7] the irradiation of water by a pulsed discharge plasma is accompanied not only by the generation of H_2O_2 but also by a dissociation process, which is reflected in the behavior of the experimental dependence. To a first approximation, this dependence may be described by the following differential equation:

$$\frac{dn}{dE}=A-B\times n. \tag{1}$$

Here n is the concentration of H_2O_2 molecules, A is the rate of H_2O_2 generation as a result of the absorption of energy from photons having the highest energy yield, and B is the coefficient of energy absorption of a single H_2O_2 molecule.

To a first approximation, we can write the following expressions for the coefficients A and B:

$$A=(\gamma_1\Phi_1)/(h\nu_1), \tag{2}$$

where γ_1 is a coefficient determining the fraction of the electromagnetic radiation in the range $\gamma_1+\Delta\nu$, which has the highest quantum yield Φ_1 for the $H_2O+h\nu_1\rightarrow H+OH$ reaction, and

$$B=(\gamma_2\Phi_2)/(h\nu_2\sigma_{abs}d). \tag{3}$$

Here γ_2 and Φ_2 are similar to γ_1 and Φ_1 but for the reverse reaction $H_2O_2+h\nu_2=2OH$, σ_{abs} is the absorption cross section, and the d is the characteristic size of the cell which determines the absorption (in our case, the cell radius). The quantum yields for the photolytic generation of H_2O_2 are

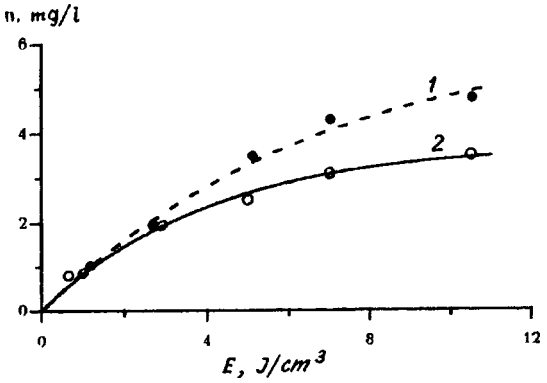

FIG. 1. Hydrogen peroxide concentration versus specific discharge energy: *1*—distilled water and *2*—tap water.

given in Refs. 4, 5, and 8. The absorption cross section for the photoprocesses leading to the dissociation of H_2O_2 and the quantum yield of this process are given in Ref. 7. These values in the expressions for the coefficients A and B will be used for the following estimates, written in the form:

$$B = 0.19\gamma_2\Phi_2 \ \text{cm}^3/\text{J},$$

$$A/B = 2.0\times 10^2(\gamma_1\Phi_1)/(\gamma_2\Phi_2) \ \text{mg/l}. \quad (4)$$

The values of the coefficients γ_1 and γ_2 determine the total spectral fraction of the radiation energy in the energy deposited by the electric discharge. The coefficient γ_1 takes into account that part of the spectrum corresponding to the generation of H_2O_2 $\lambda = 100-200$ nm, while γ_2 allows for that corresponding to dissociation, $\lambda = 200-300$ nm. Since it is fairly difficult to determine experimentally the fraction of the energy dissipated in radiation and its emissivity, we confine ourselves to a lowest-order estimate. Moreover, an estimate of the plasma column temperature can be used to estimate the ratio A/B. This estimate was based on the equation for conservation of energy, averaged over the time of action of the discharge pulse, assuming that this energy is expended in changing the internal energy of the plasma column, the mechanical work accompanying expansion, and radiation losses. These estimates showed that the temperature of the plasma column lies in the range $(10-12)\times 10^3$ K.

By comparing the estimated values of B and n_∞ with the experimental values obtained by extrapolating the experimental curves, we obtain the solution of Eq. (1):

$$n = n_\infty(1-\exp(-BE)), \quad (5)$$

where $n_\infty = A/B$ is the limiting H_2O_2 concentration which can be obtained for discharge energies $E \gg 1/B$.

A comparison between the experimental and calculated results yields the following conclusions. The experimentally determined value of the coefficient B is an order of magnitude higher than the calculated value. This is evidently because the dissociation of H_2O_2 is not caused only by the ultraviolet irradiation. An additional contribution to the dissociation process is made by reactions with impurities, such as iron or copper ions formed by erosion of the electrodes. This is supported by the fact that the curve for tap water is lower than that for distilled water. Thus, the limiting H_2O_2 concentration obtained experimentally is considerably lower than the calculated value. The presence of impurities also explains why the H_2O_2 concentration obtained after the action of the discharge decays rapidly with time, as was shown by the measurements. The experiments showed that the concentration falls almost to zero over a few days.

The main conclusions are as follows:

1. It has been established experimentally and theoretically that a pulsed discharge has a photolytic action in water, leading to the formation of hydrogen peroxide.

2. Above $w > 10-15$ J/cm^2, the steady-state concentration of hydrogen peroxide depends weakly on the specific discharge energy.

3. The hydrogen peroxide concentration is strongly influenced by impurities contained in the water, particularly erosion products from the electrodes.

This work was supported by the Russian Fund for Fundamental Research (Grant No. 97-02-16022).

[1] E. G. Zhuk, Electron. Obrab. Mater. No 1, 57 (1971).
[2] A. A. Bogomaz, V. L. Goryachev, A. S. Remennyĭ, and F. G. Rutberg, Pis'ma Zh. Tekh. Fiz. **17**(15), 65 (1991) [Sov. Tech. Phys. Lett. **17**, 448 (1991)].
[3] V. Ya. Ushmakov, *Pulsed Electrical Breakdown of Liquids* [in Russian], Tomsk (1975).
[4] V. Sokolov and G. Stein, J. Chem. Phys. **44**, 1546 (1966).
[5] V. Sokolov and G. Stein, J. Chem. Phys. **44**, 3329 (1966).
[6] V. L. Goryachev, F. G. Rutberg, and V. N. Fedyukovich, Teplofiz. Vys. Temp. **34**, 757 (1996).
[7] W. C. Schumb, C. N. Satterfield, and R. L. Wentworth, *Hydrogen Peroxide*, Amer. Chem. Soc. Monograph No. 128 (Reinhold, New York, 1955).
[8] A. M. Pravilov, *Photoprocesses in Molecular Gases* [in Russian], Énergoatomizdat, Moscow (1992).

Translated by R. M. Durham

Enhancement of the characteristics of thin-film electromluminescent structures based on ZnS:Mn films after low-power laser irradiation

Ya. F. Kononets

Institute of Semiconductor Physics, Ukrainian National Academy of Sciences, Kiev
(Submitted August 19, 1997)
Pis'ma Zh. Tekh. Fiz. **24**, 1–6 (February 26, 1998)

It is shown that short-term exposure of thin-film electroluminescent structures based on ZnS:Mn films to ultraviolet pulses with energy much lower than the threshold energies for laser annealing of ZnS:Mn films can enhance the brightness and efficiency of the electroluminescence, increase the slope of the brightness-voltage characteristics, improve the operating stability, and increase the electrical safety margin of the structures. It is established that the improvement in the properties of structures is caused by the photostimulation of below-threshold defect annealing processes and impurity diffusion, which lead to redistribution of the Mn ions in the ZnS film and reduce the concentration of shallow states which influence the structural characteristics. © *1998 American Institute of Physics.* [S1063-7850(98)01802-3]

Thin-film electromluminescent structures using ZnS:Mn films are widely used in high-information-capacity displays in information systems.[1] These displays have appreciable advantages over liquid-crystal or plasma displays, but they are expensive so that it is essential to reduce their cost to make them more competitive.[1]

One of the technological operations involved in the fabrication of these thin-film electroluminescent (TFEL) structures is thermal annealing in vacuum at 500–600 °C, which is required to achieve a uniform impurity distribution and to activate these impurities, to improve the quality of the ZnS:Mn film, and therefore enhance the brightness and electroluminescence efficiency of the TFEL structure.[1] However, this annealing makes the fabrication technology more complex because of the need to use high-melting substrates and protective measures to prevent interlayer diffusion of impurities. Laser annealing, which can recrystallize the ZnS:Mn layer without heating the substrate, requires powerful sources of ultraviolet radiation since the laser annealing threshold is $\geqslant 0.5$ J/cm^2, and the process must be carried out in a rare-gas atmosphere at a pressure of a few atmospheres.[2]

It was recently observed[3] that in ZnS:Mn films exposed to low-power pulsed ultraviolet radiation ($h\nu \geqslant 3.6$ eV, $E_p \geqslant 10^{-4}$ J/cm^2), considerably below the threshold energies for laser annealing, the photoluminescence intensity of the Mn^{2+} ions ($\lambda_{max}=585$ nm) showed an appreciable increase. The magnitude of the effect depends on the technology used to fabricate the ZnS:Mn films and on the power and duration of the ultraviolet irradiation. The aim of the present study is to determine the influence of this effect on the electroluminescence properties of TFEL structures using ZnS:Mn films, in order to identify the nature of the effect and the possibilities for using it to fabricate TFEL structures without thermal annealing.

The investigation was carried out using Metal-Insulator-Semiconductor-Insulator-Metal TFEL structures fabricated by electron-beam deposition of semiconducting (S) ZnS:Mn films and insulating (I) SiO_x-Al_2O_3 films on glass or sapphire substrates coated with a conducting In_2O_3 (M) layer and heated to $T_s=100-150$ °C. The thickness of the ZnS:Mn layer was ~ 0.6 μm and the Mn concentration was 0.8 wt. %. The thickness of the lower and upper insulating layers was of the order of 0.3 μm. The structures were fabricated in a single process cycle, but before the upper electrode Al (M) layer was deposited, the structures were either treated for 15 min with pulsed radiation from an LGI-21 laser ($\lambda=337$ nm, $E_p=10^{-3}$ J/cm^2, $f=50$ Hz) or they were thermally annealed in vacuum for 1 h at temperatures of 300, 400, and 500 °C. The three types of structures obtained—without annealing, thermally annealed, or ultraviolet treated (ultraviolet annealed)—were used for the investigations.

Studies were made of the photoluminescence and electroluminescence spectra, the brightness and electroluminescence efficiency, defined as the ratio of the brightness of the structure to the current flowing through it, and also the transported charge as a function of the applied voltage, and the kinetic characteristics of the luminescence in various spectral ranges. The brightness-voltage and charge-voltage characteristics were measured using standard techniques, and a KSVY-23 spectrometer was used to study the spectral characteristics of the luminescence. The photoluminescence was excited by pulsed radiation from an LGI-21 laser and the electroluminescence was excited by a sinusoidal voltage of frequency 40–5000 Hz or by alternating voltage pulses of 10–40 μs length. These pulses were also used to study the luminescence kinetics with a time resolution of $\leqslant 10^{-6}$ s.

The investigations showed that the emission band of the Mn^{2+} ions dominates in the photoluminescence spectra of all types of structure, since the emission outside the manganese band, including the so-called self-activated emission in the ~ 450 nm range, is two orders of magnitude weaker. It was established that the ultraviolet treatment and the thermal annealing do not significantly alter the luminescence kinetics. It was found that the ultraviolet annealing effect for the

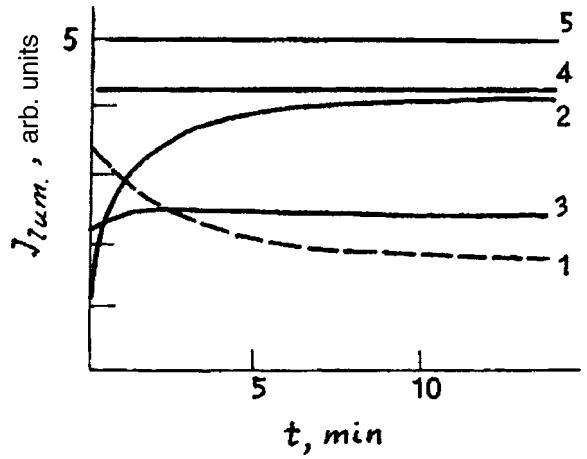

FIG. 1. Influence of time of exposure to pulsed ultraviolet radiation ($E_p=10^{-3}$ J/cm^2, $f=50$ Hz) on the photoluminescence intensity near 585 nm (*2*–*5*) and 450 nm (*1*) for the initial ZnS:Mn films (*1*, *2*) and after thermal annealing at 300, 400, and 500 °C (curves *3*, *4*, and *5*, respectively.)

ZnS:Mn films, i.e., increase in the photoluminescence intensity of the Mn^{2+} ions during excitation, is appreciable (Fig. 1) for the initial ZnS:Mn films (curve *2*), and decreases (curves *3*–*5*) after thermal annealing or an increase in deposition temperature. Ultraviolet annealing of the ZnS:Mn film ($T_s=120$ °C) for 15 min is equivalent to thermal annealing at 400 °C for 1 h (see curves *2* and *4* in Fig. 1). The increase in the photoluminescence of the Mn^{2+} ions during ultraviolet treatment of the ZnS:Mn films is accompanied by a decrease in the self-activated emission (curve *1*), which is usually attributed to intrinsic ZnS luminescence centers, including (Zn_i-V_{Zn}) defects.[4] Note that in undoped ZnS films, however, ultraviolet annealing increases the intensity of the self-activated emission.

Manganese emission also dominates in the electroluminescence spectra of these structures and ultraviolet annealing, like thermal annealing, does not substantially alter the spectra or kinetics of the luminescence. Figure 2 gives the

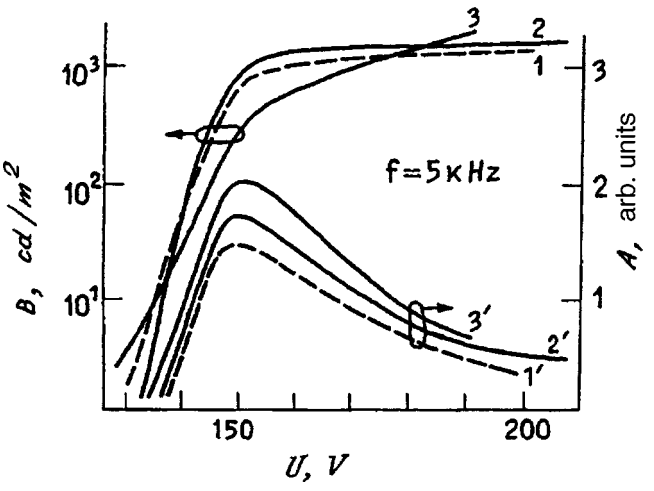

FIG. 2. Brightness (B) and efficiency (A) of the electroluminescence (*1′*–*3′*) versus voltage ($f=5$ kHz) for the initial TFEL structures (*1*, *1′*) and those treated with ultraviolet radiation for 15 min (*2*, *2′*) or thermal annealing at 500 °C for 1 h (*3*, *3′*).

brightness-voltage characteristics (curves *1*–*3*) and the electroluminescence efficiency (curves *1′*–*3′*) as a function of voltage for the initial ($T_s=120$ °C) structures (curves *1* and *1′*) and for those which had undergone additional ultraviolet annealing (15 min, curves *2* and *2′*), or conventional thermal annealing (curves *3* and *3′*). It can be seen that this ultraviolet annealing enhances the brightness and efficiency of the electroluminescence, increases the slope of the brightness-voltage characteristics (see curves *1* and *2*), and improves the electrical safety margin. The TFEL structures exposed to standard thermal annealing at $T_0=500$ °C (curves *3* and *3′*) have a higher brightness and electroluminescence efficiency but the slope of the current-voltage characteristics is gentler and the electrical safety margin is lower, apparently because of the deterioration in the properties of the insulating layers caused by the thermal annealing. This is why thermal annealing is usually carried out before the upper insulator is deposited.

It is known[2] that doping of ZnS with manganese, which is an efficient luminescence center in ZnS, isoelectronically replacing a zinc atom in the cationic sublattice, is more effective when this sublattice contains vacancies—zinc vacancies (V_{Zn})—where the manganese is incorporated, as is indicated by the decrease in the self-activated emission observed when the ZnS is doped with manganese. The increase in the self-activated emission observed as a result of ultraviolet annealing in undoped ZnS films and its decrease in ZnS:Mn films indicates that the ultraviolet quanta stimulate V_{Zn} defect formation processes and therefore the diffusion of manganese ions to form additional luminescence centers. It is known[5] that the activation energies of these processes decrease considerably in highly disordered lattices and thus these processes may play an important role on exposure to ultraviolet pulses at below-threshold power.[6]

It is postulated that the observed influence of these below-threshold ultraviolet radiation pulses on the properties of ZnS:Mn films deposited at $T<150$ °C and therefore containing a considerable number of nonequilibrium defects including manganese atomic inclusions, is caused by the photostimulation of defect formation processes such as V_{Zn} and diffusion of Mn to form additional luminescence centers. This is accompanied by a reduction in the number of shallow states which influence the brightness and efficiency of the electroluminescence, the slope of the brightness-voltage characteristic, and the operating stability of the TFEL structure.

The ultraviolet annealing conditions were not optimized, but the results indicate that exposure of the TFEL structures to LGI-21 laser pulses for 15 min is equivalent to thermal ananealing of these structures for 1 h in vacuum at 400 °C. It has thus been demonstrated that thermal annealing may be replaced by a short period of selective ultraviolet annealing which, by simplifying and reducing the cost of the fabrication technology, can produce TFEL structures with acceptable characteristics on inexpensive, low-melting substrates.

The author would like to thank L. I. Veligura for assistance with the preparation of the structures.

[1] Y. F. Ono, *Electroluminescent Displays* (World Scientific, Singapore, 1995), p. 187.
[2] Jonson, US Patent No. 4 442 136, published Oct. 1984.
[3] L. I. Veligura, Ya. F. Kononets, and O. A. Ostroukova, *Abstracts of International Conference on Luminescence, FIAN, Moscow, 1994*, p. 232.
[4] J. E. Nichols, J. J. Devis, and B. C. Covenott, J. Phys. C. Solid. State Phys. **12**, 370 (1979).
[5] V. I. Emel'yanov, Izv. Ross. Akad. Nauk, Ser. Fiz. **56**(4), 147 (1992).
[6] R. V. Prudnikov, P. K. Kashkarov, and V. Yu. Kashkarov, Vestn. Mosk. Gos. Univ. **36**, 61 (1995).

Translated by R. M. Durham

Influence of electron irradiation on the fundamental absorption edge of a copper monoxide CuO single crystal

Yu. P. Sukhorukov, N. N. Loshkareva, A. S. Moskvin, V. L. Arbuzov, and S. V. Naumov

Institute of Metal Physics, Ural Branch of the Russian Academy of Sciences, Ekaterinburg; Urals State University, Ekaterinburg
(Submitted August 22, 1997)
Pis'ma Zh. Tekh. Fiz. **24**, 7–12 (February 26, 1998)

As a result of irradiation of a CuO single crystal with 5 MeV electrons, the fundamental absorption edge has an ''Urbach'' appearance and characteristic features appear near the edge. These changes are explained using a model of polar-center phase nuclei. © *1998 American Institute of Physics.* [S1063-7850(98)01902-8]

In systems with charge nonuniformity, which includes the p-type antiferromagnetic semiconductor CuO, nuclei (microgranules) of a new phase of polar (electron and hole) Jahn-Teller centers are formed.[1] These nuclei are responsible for the many unique properties of copper-oxygen compounds.[2] These nucleation centers may be crystal defects, including radiation defects. In earlier studies we investigated the influence of 5 MeV electron irradiation on the electrical[3] and optical properties of CuO single crystals.[4] We observed that the electrical resistivity of the single crystal increased and the absorption intensity became redistributed between bands corresponding to transitions in the matrix and p-type polar centers. Here we present the results of a study to determine the influence of electron irradiation on the fundamental absorption edge of CuO.

The characteristics of the CuO single crystals used were given in Ref. 1. We used a sample of thickness (50 ± 5) μm in the (110) plane, in which the crystal c axis lies. The CuO was irradiated at 250 K using a linear accelerator at an electron energy of 5 MeV and fluence of 3×10^{18} cm^{-2}. The optical absorption spectra were investigated using a KSVU-12 optical system in the spectral range 1–2 eV using both natural light and polarized light with $E\| c$ and $E\perp c$. The measurements were made over the temperature range 70–300 K and the relative error in the determination of the absorption coefficient was 1.8%.

According to the cluster model, the fundamental absorption edge in CuO can be attributed to transitions with $b_{1g}-e_u$ charge transfer in the $[CuO_4]^{-6}$ cluster.[5] In an unirradiated CuO single crystal, the edge is described by indirect allowed transitions for which the band gap E_g is 1.46 eV at room temperature and 1.54 eV at $T=80$ K.

Electron irradiation of a CuO single crystal causes considerable changes near the absorption edge, as shown in Fig. 1: 1) a narrow band appears at $h\omega=1.34$ eV, 2) the fine structure of the narrow exciton-like band at 1.7 eV disappears, and 3) the fundamental absorption edge becomes broader. The 1.34 eV band has a high absorption coefficient $K\sim 1000$ cm^{-1}. When the temperature is reduced to 80 K, its intensity increases negligibly and its position remains the same. We recently observed a similar band when CuO single crystals were bombarded with He^+ ions. This band had unusual polarization properties for bands associated with optical transitions: in unpolarized light, the band maximum was observed at higher energies than in polarized light. This observation suggests that this band is caused by light scattering at defects, evidently at phase nuclei of polar centers, whose refractive index differs from that of the matrix.

The broadening of the absorption edge of the irradiated sample is accompanied by a considerable reduction in the absorption coefficient near 1.6–2.0 eV. In the range $K\approx 1000^{-1}$ the absorption edges of the irradiated and unirradiated CuO intersect, being divided into two parts at the point of intersection: lengthened tails at the base and a broadened section at the peak of the absorption band. In polarized light the broadening of the absorption edge remains unchanged.

Whereas the behavior $K\sim(h\omega-Eg)^2$ observed before irradiation of CuO at $T=300$ K and $T=80$ K indicated the existence of indirect allowed transitions,[5] after irradiation we did not obtain any curves typical of a specific type of transition. Unlike the unirradiated CuO, the absorption edge of the electron-irradiated single crystal is described by an exponential dependence of absorption on energy (Urbach edge). The curves obtained at different temperatures in natural light converge at a ''focal point'' $E_0=1.62$ eV (inset in Fig. 1). As the temperature increases, the slope of the curves decreases. Calculations of the temperature dependence of the optical gap $El_g(T)$ were made using a model proposed in Ref. 6 using the following values for the parameters: $\sigma_0=0.424$—the parameter of the change in $El_g(T)$, the high-temperature variation $dE_g/dT=-0.004$ meV, and the sum of the constants which include the contributions of the self-energies of the electrons and holes to the lattice vibrations and the expansion of the crystal $A_v+A_c=89$ meV. In this case, the photon energy was taken as $h\omega=50$ meV which was obtained by analyzing the absorption edge of the unirradiated single crystal.[5] The values of El_g obtained using this formalism, 1.42 eV at $T=295$ K and 1.61 eV at $T=80$ K, differ from the value of E_g for the unirradiated crystal.

Prior to irradiation of CuO with the polarization $E\| c$, the temperature dependence $E_g(T)$ in the range $80<T<273$ K was accurately described by the Varshni formula.[5] A devia-

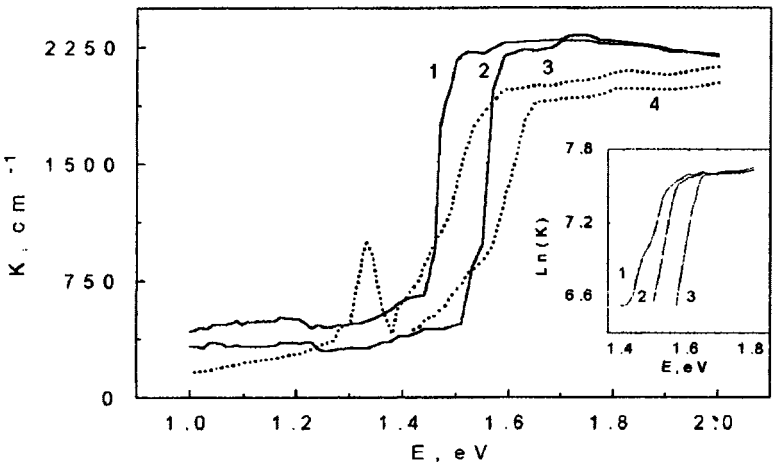

FIG. 1. Absorption spectrum of CuO single crystal in natural light: *1,2*—before irradiation, *3,4*—after irradiation, at temperatures: *1,3*—300 K, *2,4*—80 K. Inset—ln(K) versus photon energy, *1*—$T=300$ K, *2*—245 K, *3*—80 K.

tion of the experimental curve near $T=205$ K was caused by the appearance of a fine structure at the exciton-like peak in the presence of magnetic ordering. For the irradiated CuO single crystal, the temperature behavior of the optical gap $El_g(T)$ can be investigated by measuring the temperature shift of the absorption edge at values of K above, at, and below the point of intersection of the edges, respectively: 1) $K=1650$ cm^{-1}, 2) $K=1100$ cm^{-1}, and 3) $K=1400$ cm^{-1} (Fig. 1). In natural light the curves $El_g(T)$ for all K decrease monotonically (Fig. 2) and the curve $El_g(T)$, obtained at $K=1100$ cm^{-1} is the closest to $E_g(T)$ for the unirradiated sample. The total variation of $El_g(T)$ in the range 70–300 K is 0.11 eV, as for the unirradiated sample. For polarized light an Urbach treatment of the absorption edge reveals that the curve $El_g(T)$ ceases to be monotonic, and anomalies appear near the magnetic phase transition points at $T_{N1}=213$ K and $T_{N2}=231$ K (T_{N1} is the temperature of the transition from collinear three-dimensional antiferromagnetic ordering to noncollinear and T_{N2} is the temperature of the transition from noncollinear antiferromagnetic ordering to low-dimensional magnetism). With decreasing K, the characteristic features of $El_g(T)$ are intensified, and this is observed most clearly for $E\|c$ and $K=1100$ cm^{-1} (inset to Fig. 2).

The decrease in magnitude and broadening of the edge at the threshold absorption peak observed under electron irradiation of CuO is attributed to an increase in the volume and concentration of phase nuclei of polar centers. An increase in the number of polar centers is caused by a decrease in the number of initial $[CuO_4]^{6-}$ clusters corresponding to the CuO matrix, and leads to redistribution of the intensities of the electric-dipole transitions: a decrease in K at the absorption edge and an increase in the infrared bands associated with transitions to p-type polar Jahn-Teller centers.[4] The disappearance of the fine structure of the exciton-like band near the absorption edge is caused by the broadening of the edge. However, the anomalies of $El_g(T)$ near the magnetic phase transitions may indicate that this fine structure makes some contribution (inset to Fig. 2). Similar but weaker anomalies were observed in the unirradiated sample and were attributed to the appearance of a fine structure at the 1.7 eV exciton-like band.[5]

The appearance of a lengthened tail in the lower part of the absorption threshold of the irradiated sample may be attributed to a lower-intensity band associated with the fine structure and to light scattering at radiation defects. With the exception of the 1.34 eV peak, the difference between the absorption coefficient in the tail before and after irradiation depends linearly on $1/\lambda^4$ which may indicate light scattering by inhomogeneities[7]—inhomogeneous-phase nuclei formed around radiation defects.

To sum up, the formation of additional nucleation centers as a result of electron irradiation of a CuO single crystal

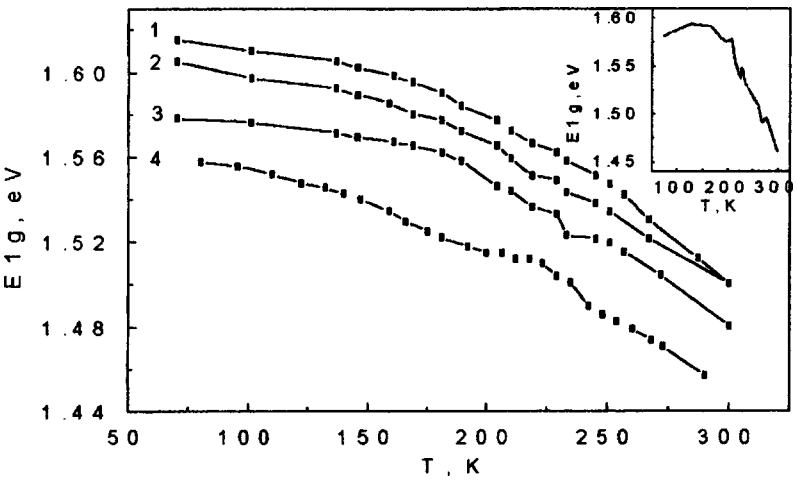

FIG. 2. Temperature dependence of the optical gap of a CuO single crystal in natural light: *1–3*—after irradiation with the absorption coefficient: *1*—$K=1650$ cm^{-1}, *2*—1400 cm^{-1}, *3*—1100 cm^{-1}, and *4*—before irradiation. Inset—temperature dependence of the optical gap for $E\|c$.

gives rise to an exponential fundamental absorption edge, changes in the fine structure at the absorption edge, and light scattering at phase nuclei of polar centers formed around radiation defects.

This work was supported by the Russian Fund for Fundamental Research, Project No. 96-02-16063-a.

[1] A. S. Moskvin, N. N. Loshkareva, Yu. P. Sukhorukov *et al.*, Zh. Éksp. Teor. Fiz. **105**, 967 (1994) [JETP **78**, 518 (1994)].
[2] A. S. Moskvin, *Nature of the Unusual Physical Behavior of Copper Oxides* [in Russian] Urals State University Press, Ekaterinburg (1995).
[3] B. A. Gizhevskiĭ, V. L. Arbuzov, A. A. Samokhvalov *et al.*, Pis'ma Zh. Tekh. Fiz. **20**(7), 1 (1994) [Tech. Phys. Lett. **20**, 259 (1994)].
[4] N. N. Loshkareva, Yu. P. Sukhorukov, B. A. Gizhevskiĭ *et al.*, Fiz. Tverd. Tela (St. Petersburg) **37**, 376 (1995) [Phys. Solid State **37**, 203 (1995)].
[5] Yu. P. Sukhorukov, N. N. Loshkareva, A. S. Moskvin *et al.*, Zh. Éksp. Teor. Fiz. **108**, 1821 (1995) [JETP **81**, 998 (1995)].
[6] T. Skettrup, Phys. Rev. B **18**, 2622 (1978).
[7] H. C. van de Hulst, *Light Scattering by Small Particles* (Wiley, New York, 1957; IL, Moscow, 1961).

Translated by R. M. Durham

Anisotropy of the nonreciprocal linear birefringence in crystals

M. A. Novikov and A. A. Khyshov

Institute of Microstructure Physics, Russian Academy of Sciences, Nizhniĭ Novogorod
(Submitted August 20, 1997)
Pis'ma Zh. Tekh. Fiz. **24**, 13–18 (February 26, 1998)

Results are presented of an experimental investigation of nonreciprocal linear birefringence (a difference between the phase velocities of counterpropagating waves having the same linear polarization) in lithium iodate and potassium dihydrophosphate crystals in a magnetic field. An original double-pass optical measuring system using two linear quarter-wave phase plates (Fresnel rhombs) is used to demonstrate a new method of studying the effect which can give a fairly high sensitivity and avoid accompanying effects. © *1998 American Institute of Physics.* [S1063-7850(98)02002-3]

As we are well aware, allowance for spatial dispersion in crystals leads to qualitatively new optical phenomena,[1] including nonreciprocal linear birefringence (a difference between the phase velocities of counterpropagating waves having the same linear polarization). It was noted in Refs. 2–4 that a similar effect occurs in magnetically ordered crystals, which was recently observed experimentally.[5]

It was shown in a study made by one of the authors[6] that nonreciprocal linear birefringence also occurs in noncentrosymmetric crystals exposed to an external magnetic field, and this was first observed experimentally in Ref. 7 using a laser gyroscope.

This effect is between three and four orders of magnitude weaker than the Faraday effect, and its observation therefore presents major experimental difficulties. This is obviously the reason why very few experimental results have been reported on this topic by other authors in the literature known to us. However, the number of published theoretical studies on this effect is very large indeed. Thus, the development of methods of studying this effect is a matter of some urgency.

The aim of the present study is to develop a new method of investigating nonreciprocal linear birefringence which can ensure fairly high sensitivity and can avoid the influence of accompanying stronger effects. The advantage of this method is demonstrated by measuring the nonreciprocal linear birefringence in lithium iodate (α-$LiIO_3$) and potassium dihydrophosphate (KDP) crystals.

In order to describe optical effects in a static magnetic field with allowance for the spatial dispersion, we use an expansion of the permittivity tensor in the following form:[8]

$$\varepsilon_{ij}(\mathbf{k},\mathbf{H}(0))=\varepsilon_{ij}+A_{ijk}H_k+B_{ijk}k_k+C_{ijkl}k_kH_l(0), \quad (1)$$

where $\mathbf{k}$ is the wave vector and $\mathbf{H}(0)$ is the vector of the static magnetic field. In Eq. (1) the first term of the expansion is responsible for the natural linear birefringence, the second is responsible for the Faraday effect, the third for the natural optical activity, and the fourth for the nonreciprocal linear birefringence. Only the terms in the expansion (1) associated with the tensors A_{ijk} and C_{ijkl} can give rise to nonreciprocal optical effects. The axial tensor C_{ijkl} is symmetric with respect to the first two subscripts and its manifestation depends strongly on the type of anisotropy which may occur in the selected direction of light propagation. It was shown in Ref. 8 that the most favorable situation arises when strong natural linear birefringence is observed in the direction of light propagation. In this case, the Faraday effect makes a small contribution to the nonreciprocal phase shift. Even greater discrimination against the Faraday effect can be achieved if a transverse variant of nonreciprocal linear birefringence is selected and the light is directed perpendicular to the optic axis of a uniaxial crystal. In this case, the induced nonreciprocal linear birefringence is added to the natural linear birefringence. As a result, the ordinary ''o'' and extraordinary ''e'' waves will have different phase shifts for the opposite directions. This configuration was selected to observe nonreciprocal linear birefringence in α-$LiIO_3$ and KDP crystals. The following expressions can be obtained for the anisotropy of the nonreciprocal variation in the refractive index of these crystals:[8]

$$\delta n(\alpha\text{-LiIO}_3)=\Delta n_o^{\pm}-\Delta n_e^{\pm}$$
$$=\pm(C_{2212}-C_{3312})\left(\frac{\pi H(0)}{\lambda}\right), \quad (2)$$

$$\delta n(\text{KDP})=\Delta n_o^{\pm}-\Delta n_e^{\pm}$$
$$=\pm(C_{1122}-C_{1111}-2C_{1212}-C_{3311})$$
$$\times\left(\frac{\pi H(0)}{\lambda}\right)\sin(2\Theta), \quad (3)$$

where C_{ijkl} are the tensor components describing the induced nonreciprocal effect in these crystals, λ is the wavelength, and Θ is the angle between the direction of propagation of light in the crystal and the X axis in a KDP crystal (a crystal cut at 45° to the X axis was used in the experiment). For α-$LiIO_3$ no dependence on Θ is observed.

For the experiments we used a double-pass optical system to measure the nonreciprocal linear birefringence. This system incorporated two quarter-wave phase plates (Fresnel rhombs) in front of the crystal (CR) and a rotating mirror (M) (see Fig. 1). The first and second Fresnel rhombs were

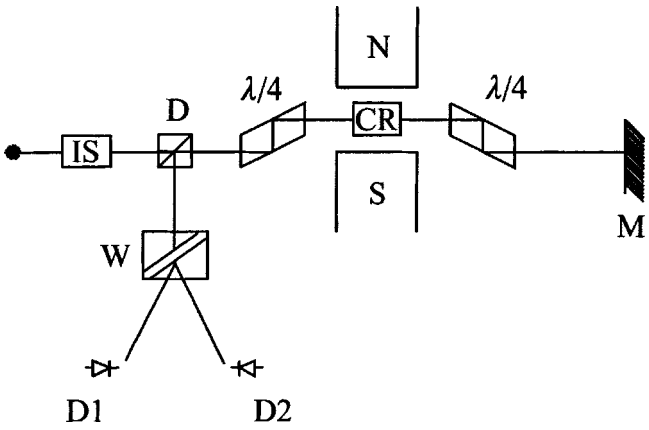

FIG. 1.

oriented at angles of 45° and $-45°$, respectively. It is easy to show that this system eliminates the influence of reciprocal optical effects and isolates the Faraday effect of nonreciprocal linear birefringence in its pure form. The use of a modulation method of measurement can enhance the sensitivity of the measurements and reduce systematic errors, which ultimately provides more reliable data on the nonreciprocal linear birefringence.

The polarization characteristics of the optical system can be conveniently calculated using the well-known Jones method. It is easily shown that the Jones matrix for passage twice through a Fresnel rhomb, crystal, Fresnel rhomb, mirror, and back may be written in the form:

$$\begin{pmatrix} \cos(\delta\varphi) & -\sin(\delta\varphi) \\ \sin(\delta\varphi) & \cos(\delta\varphi) \end{pmatrix}, \tag{4}$$

where $\delta\varphi$ is the nonreciprocal phase difference:

$$\delta\varphi = \frac{2\pi}{\lambda}\delta n d, \tag{5}$$

where d is the crystal length. After passing through a system described by the matrix (4), the angle of inclination of the plane of polarization of the radiation is modulated.

The radiation source was an LGN-302 ($\lambda = 0.63\ \mu$m) helium-neon laser. A nonreciprocal optical isolator (IS) was placed in front of the laser to eliminate any ''reaction'' of the reflected light on this laser (see Fig. 1). To reduce the influence of the laser amplitude noise, we used a differential polarization detector consisting of a Wollaston prism (W) and two photodiodes (D1 and D2). The sensitivity of the measurements was enhanced by means of a synchronous detection method using a variable magnetic field with a frequency of 66 Hz and amplitude up to 2.5×10^5 A/m, generated by an electromagnet. A semitransmitting mirror (D) was used to separate the beam on its return trip. At a laser power of 1 mW the sensitivity of the system was 10^{-6} rad with an averaging time $\tau = 10$ s.

It can be shown that for this optical measuring system, when the laser radiation is vertically polarized, we have

$$|E_{\text{out}}|_2^2 = |E_0|^2\left(\frac{1}{2} - \delta\varphi\right), \tag{6}$$

$$|E_{\text{out}}|_1^2 = |E_0|^2\left(\frac{1}{2} + \delta\varphi\right), \tag{7}$$

where E_0 is the amplitude of the incident optical radiation.

From Eqs. (6) and (7) the signal at the exit from the differential amplifier will be given by

$$\Delta J \sim 2|E_0|^2\delta\varphi, \tag{8}$$

where $\delta\varphi = \delta\varphi_0\cos(\Omega t)$ and Ω is the modulation frequency of the magnetic field generated by the electromagnet. The dependence of $\delta\varphi_0$ on the amplitude of the magnetic field was measured experimentally. As was to be expected from Eqs. (2)–(5), this dependence exhibited linear behavior. The measured values for these crystals were

$$\frac{\delta n}{H}(\alpha\text{-LiIO}_3) = (3.57\pm0.25)\times10^{-15}\left(\frac{\text{A}}{\text{m}}\right)^{-1},$$

$$\frac{\delta n}{H}(\text{KDP}) = (2.32\pm0.5)\times10^{-16}\left(\frac{\text{A}}{\text{m}}\right)^{-1}.$$

During the experiments it was confirmed that the effect did not occur if the magnetic field was parallel to the optic axis of the crystals. In addition, as was to be expected, reversing the direction of the optic axis for both crystals reversed the sign of the effect since α-$LiIO_3$ and KDP crystals are polar. The crystals were shielded with aluminum foil to eliminate the influence of the Pockels electrooptic effect.

These results indicate that the proposed method can considerably increase the scope for studying nonreciprocal linear birefringence which is interesting not only from the physics point of view but also for various applications in laser optics, such the development of nonreciprocal phase elements in optical gyroscopes.

This work was partially supported by the Russian Fund for Fundamental Research (Grant No. 95-02-05653).

[1] V. M. Agranovich and V. L. Ginzburg, *Crystal Optics with Spatial Dispersion, and Excitons*, 2nd ed. (Springer-Verlag, New York, 1984) [Russ. original, earlier ed., Nauka, Moscow, 1965].
[2] R. M. Hornreich and S. Strichmann, Phys. Rev. **171**, 1065 (1968).
[3] V. N. Lyubimov, Kristallografiya **14**, 213 (1969) [Sov. Phys. Crystallogr. **14**, 168 (1969)].
[4] R. V. Pisarev, Zh. Éksp. Teor. Fiz. **58**, 1421 (1970) [Sov. Phys. JETP **31**, 761 (1970)].
[5] B. B. Krichevtsev, V. V. Pavlov, R. V. Pisarev *et al.*, J. Phys.: Condens. Matter **5**, 8233 (1993).
[6] M. A. Novikov, *Abstracts of Papers presented at Nonlinear Optics Conference*, Minsk, 1972 [in Russian].
[7] V. A. Markelov, M. A. Novikov, and A. A. Turkin, JETP Lett. **25**, 378 (1977).
[8] M. A. Novikov, Kristallografiya **24**, 666 (1979) [Sov. Phys. Crystallogr. **24**, 383 (1979)].

Translated by R. M. Durham

Laser interferometer with fine-focused beams to monitor the spatial position of an object

V. P. Ryabukho, V. L. Khomutov, D. V. Lyakin, and K. V. Konstantinov

Institute of Problems in Precision Mechanics and Control, Russian Academy of Sciences, Saratov State University

(Submitted August 12, 1997)
Pis'ma Zh. Tekh. Fiz. **24**, 19–24 (February 26, 1998)

Analogies with interferometers using a light source with low temporal coherence are used to analyze the principles of the construction of laser interferometers with averaging over the photodetector aperture, whose sensitivity to the position of an object being monitored at the maximum of the output signal is as good as that of low-coherence interferometry and tomography.
 [S1063-7850(98)02102-8]

A new trend in optical measurements—low-coherence interferometry—has recently been actively pursued. These techniques can monitor the position of an object (including those in the bulk of a dispersive medium) using the modulus of the degree of temporal coherence of the radiation, i.e., using the maximum of the interference signal, with a sensitivity determined by the temporal coherence length.[1–7] In Ref. 8, the modulus of the spatial coherence function of the radiation was used as the informative parameter. Bearing in mind the space-time analogies in the properties of wave fields, in the present study we consider a laser interferometer which, as in a low-coherence interferometry, is highly sensitive to the spatial position of an object at the maximum of the interference signal, but the laser radiation has a high degree of temporal and spatial coherence.

The equivalence of the processes of temporal and spatial averaging is best shown when the photodetector does not resolve the amplitude-phase spatial distributions in the resultant interference field. In this case, in the classical interference equation for the intensity we need to introduce averaging over the area S_ϕ of the resolving element (or the entire aperture) of the photodetector in addition to averaging over the temporal response of the photodetector τ_ϕ. The power of the recorded field P can then be written as

$$P(\Delta z)=P_1+P_2+2\times\int\int_{S\phi}\tau_\phi^{-1}\int_0^{\tau\phi}\sqrt{I_1(\boldsymbol{\zeta},t)I_2(\boldsymbol{\zeta},t-\Delta t)}\times\cos[\omega_0\Delta t+\Delta\varphi_0(t,\Delta t)+\Delta\Psi(\boldsymbol{\zeta},\Delta z)+\Delta\Phi_S(\boldsymbol{\zeta})]dtd^2\boldsymbol{\zeta}, \quad (1)$$

where P_1 and P_2 are the powers of the interfering light beams, $I_1(\boldsymbol{\zeta},t)$ and $I_1(\boldsymbol{\zeta},t-\Delta t)$ are the instantaneous intensities,[9] determined by averaging over the time τ, which is shorter than the coherence time τ_c, but substantially exceeds the period of the field oscillations $T=2\pi/\omega_0$, $\Delta t=f(\Delta z)$ is the time delay of the waves in the interferometer, Δz is the spatial parameter, $\Delta\varphi_0(\Delta t,t)$ is the difference between the initial phases of the oscillations of the interfering waves, $\Delta\Psi(\boldsymbol{\zeta},\Delta z)$ is the deterministic spatial component of the phase difference which is determined by the configuration of the interferometer system, and $\Delta\Phi_S(\boldsymbol{\zeta})$ is the random phase difference caused, for example, by interference between laser speckle fields.

In low-coherence interferometry the interference signal vanishes for $\Delta t>\tau_c$ when the waves become mutually incoherent, i.e., when the difference between the initial phases of the oscillations $\Delta\varphi_0(\Delta t,t)$ becomes a strongly fluctuating function during the averaging time τ_ϕ. It follows from Eq. (1) that a similar result is obtained if the spatial components of the phase difference $\Delta\Psi(\boldsymbol{\zeta},\Delta z)+\Delta\Phi_S(\boldsymbol{\zeta})$ also vary substantially over the photodetector aperture S_ϕ, for example, as a result of a longitudinal displacement Δz of the object in the interferometer system. If specular surfaces are used in the interferometer, we can assume $\Delta\Phi_S=0$ and the spatial variation of the phase difference $\Delta\Psi(\boldsymbol{\zeta},\Delta z)$ at the photodetector aperture is then determined only by the interferometer configuration and by the phase aberrations of the wave fields. A substantial variation $\Delta\Psi$ at the photodetector aperture (in other words, mismatch between the phase distributions of the interfering waves[10,11]) may be achieved in an interferometer with fine-focused laser beams (Fig. 1) when the curvature of the wave surfaces of the interfering waves at the photodetector aperture differs substantially.

Assuming that spherical waves interfere in the exit arm of the interferometer, we can easily derive an expression for $\Delta\Psi(\boldsymbol{\zeta},\Delta z)$ at the photodetector aperture, $\Delta\Psi\cong(\pi M^2\Delta z/\lambda z^2)\boldsymbol{\zeta}^2$, where M is the transverse magnification of the objective in the object arm of the interferometer, Δz is the longitudinal displacement of the object mirror, and z is the distance between the laser beam constriction and the plane of the photodetector aperture ($z\gg M^2\Delta z$). Integrating in Eq. (1) over the variable ζ within the angular aperture of the laser beams bounded by the objective aperture, we obtain the following expression for the coefficient of modulation β of the interferometer photoelectric signal:

$$\beta=|\sin(u)/u|, \quad u\cong\pi NA^2\Delta z/2\lambda, \quad (2)$$

where the Abbe sine condition is used and NA is the numerical aperture of the objective.

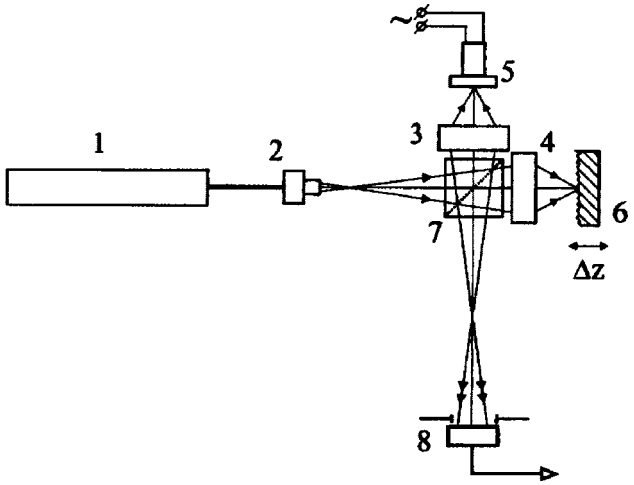

FIG. 1. Laser interferometer with fine-focused beams to monitor the spatial position of the surface of an object using the maximum of the interference signal: *1*—laser, *2*—microscope objective, *3*,*4*—focusing objectives, *5*—reference mirror on piezoelectric element, *6*—object, *7*—beam splitter, and *8*—photodetector with wide aperture diaphragm.

Figure 2a gives experimental values for the signal modulation coefficient normalized to the maximum $\beta/\beta_{\max}$ and theoretical curves for β obtained using Eq. (2) for objectives in the object arm for various numerical apertures NA. Good agreement is observed between the experimental and theoretical data, which shows that the main contribution to the decrease in the interference signal is made by the mismatch of the phase distributions of the waves rather than the amplitude distributions, which were not taken into account to derive relation (2).

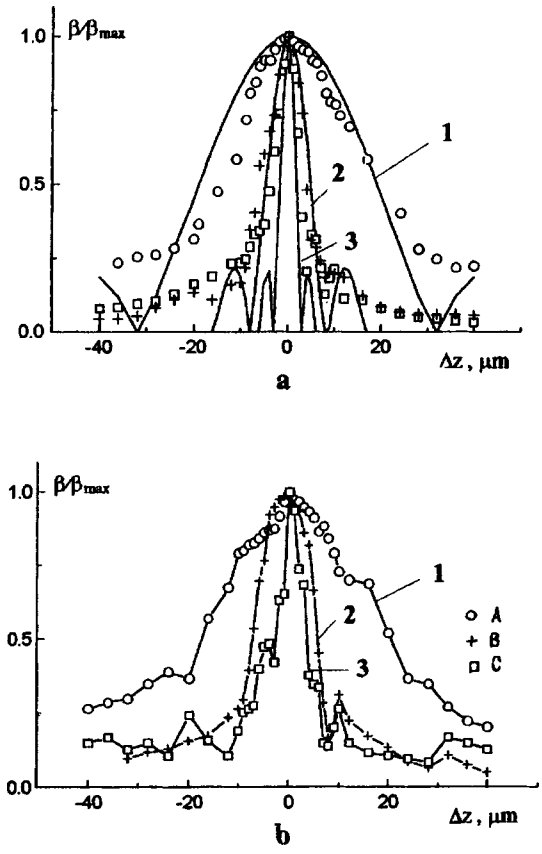

FIG. 2. Normalized coefficient of modulation of photoelectric signal as a function of the longitudinal displacement Δz of an object with specular (a) and rough (b) surfaces for various numerical apertures NA of the objective in the object arm of the interferometer: *1–3*—theoretical (a) and experimental (b) curves, experimental points *A*, *B*, and *C* correspond to $NA=0.20$, 0.40, and 0.65, respectively.

If the object has a rough surface, the object field is speckle-modulated, $\Delta\Phi(\zeta)\neq\text{const}$ which causes an additional mismatch between the random amplitude-phase spatial distributions of the interfering waves and reduces the signal modulation coefficient β, whose value in this case depends on the specific realization of the speckle field at the photodetector aperture. When the surface of the object is displaced from the constriction of the focused laser beam, the diameter of the illuminated region increases, which is accompanied by a reduction in the size of the speckles in the photodetector aperture. This process of mismatch between the interfering waves, added to the mismatch for the deterministic phase difference $\Delta\Psi(\zeta,\Delta z)$, should produce a sharper extremum in the dependence of the signal modulation coefficient $\beta/\beta_{\max}$ on the surface displacement Δz. However, it was observed experimentally that the maxima of the signal modulation coefficient have approximately the same width as for a specular surface for the same numerical apertures of the objective (Fig. 2b). Thus, the dominant contribution to the mismatch of the interfering waves in the interferometer as a function of the displacement of the object Δz is made by the deterministic spatial distribution of the phase difference $\Delta\Psi(\zeta,\Delta z)$ which is found for speckle modulation of the interfering waves.[12]

Equation (2) can be used to estimate the half-width Δz_m of the maximum of the modulation coefficient β: $\Delta z_m\cong 2\lambda/NA^2$, which shows that for $NA\to 1$ the photoelectric signal only contains a few interference oscillations, which are easy to observe experimentally when the amplitude of the reference mirror vibrations is $l_0>\Delta z_m$ and the numerical aperture of the objective in the reference arm of the interferometer is $NA=0.8$. This result corresponds to the practical limit of a low-coherence interferometer.[7] The experiments showed that the error in the determination of the position of the objective was smaller than Δz_m. For example, for $NA=0.4$ the average deviation of the values was $\approx 3\ \mu$m for a specular objects and $\approx 4\ \mu$m for rough objects (with $\Delta z_m=8\ \mu$m).

Thus, an interferometer with fine-focused laser beams has fundamental measuring and diagnostic parameters as good as those of interferometers using light sources with a low degree of temporal coherence. Preliminary experiments have shown that this interferometer may be used to observe and determine the position of a reflecting object in a dispersive medium, i.e., in situations where low-coherence interferometry has the widest application.[7]

The authors would like to thank V. V. Tuchin for useful discussions of low-coherence interferometry and tomography in biomedical applications, and for his interest and support with this work.

[1] I. P. Ivanov, A. P. Chaĭkovskiĭ, and A. A. Kumeĭsha, Zh. Prikl. Spektrosk. **28**, 518 (1978); Dokl Akad Nauk SSSR **23**, 503 (1978).
[2] E. V. Ivakin and A. I. Kitsak, Opt. Spectrosk. **52**, 99 (1982) [Opt. Spektrosk. **52**, 59 (1982)].
[3] A. F. Fercher, K. Mengedoht, and W. Werner, Opt. Lett. **13**, 186 (1988).
[4] C. K. Hitzenberger, Appl. Opt. **31**, 6637 (1992)
[5] A. F. Fercher, C. K. Hitzenberger, and M. Luchem, J. Mod. Opt. **38**, 1327 (1991).
[6] A. F. Fercher, C. K. Hitzenberger, W. Drexler, G. Kamp, I. Strasser, and H. C. Li, in *Medical Optical Tomography: Functional Imaging and Monitoring* (Proc. SPIE **S11**, 1993), pp. 355–370.
[7] *Coherence-Domain Methods in Biomedical Optics*, edited by V. V. Tuchin, Chap. 4: *Low-Coherence-Interferometry and Tomography* (SPIE Press, Washington, 1996), pp. 210–250.
[8] N. G. Vlasov and A. E. Shtan'ko, Opt. Tekh. Vest. SPIE/RUS, No. 4, 12 (1994).
[9] E. Wolf and L. Mandel, Usp. Fiz. Nauk. **87**, 491 (1965) [*sic*].
[10] V. V. Protopopov and N. D. Ustinov, *Laser Heterodyning* [in Russian], Nauka, Moscow (1985).
[11] B. S. Rinkevichyus, *Laser Diagnostics of Fluxes* [in Russian], MÉI, Moscow (1990).
[12] V. P. Ryabukho, I. S. Klimenko, and L. I. Golubentseva, Proc. SPIE **2340**, 513 (1994).

Translated by R. M. Durham

Formation of a diamond-like phase under conditions of preferential deposition of nondiamond carbon in a microwave gas discharge plasma with electron cyclotron resonance

S. Yu. Suzdal'tsev, S. V. Sysuev, and R. K. Yafarov

Institute of Radio Engineering and Electronics, Russian Academy of Sciences, Saratov Branch
(Submitted May 7, 1997)
Pis'ma Zh. Tekh. Fiz. **24**, 25–31 (February 26, 1998)

Films with crystallite sizes up to approximately 0.5 μm were obtained. Results of complex investigations of these films are presented. © *1998 American Institute of Physics.*
[S1063-7850(98)02202-2]

Studies of the conditions and mechanism for the chemical synthesis of diamond films at low pressures and temperatures have important practical and scientific applications.[1] This topic has recently become a matter of far greater urgency with the search by researchers in many countries for methods of developing long-lived, highly stable, inexpensive field electron emitters for planar displays and devices in vacuum microwave microelectronics. A promising material in this respect is carbon, and particularly one of its structural modifications—diamond, which has a most attractive combination of the highest recorded values of various physicochemical parameters and unique electron emission properties. The aim of this investigation was to study the laws governing the nucleation and growth of the diamond-like phase of carbon in its other allotropic modifications.

Carbon films were deposited on a glass substrate using a system described in Ref. 2. The density and characteristic dimensions of the crystallites at the surface of the film were investigated as a function of the substrate temperature at various ethanol vapor pressures and accelerating potentials at the substrate holder. A detailed study of the microtopography of the films was made using a P4-SPM-MDT scanning atomic force microscope.

Figure 1 shows the densities of the crystallites formed during the deposition of carbon films as a function of the substrate temperature, for various ethanol vapor pressures in the microwave discharge plasma. The crystallites had the form of cones or pyramids with base diameters between 0.25 and 0.5 μm and heights between 0.08 and 0.3 μm. These curves correlate with the curves giving the rates of deposition of carbon films as a function of these process parameters, obtained in Ref. 3.

Typical x-ray diffraction patterns obtained at low substrate temperatures revealed no well-defined peaks characteristic of any crystalline phase of carbon, despite the crystalline microprotrusions identified with the atomic force microscope. These films were yellow, did not adhere to the substrate (they were ''friable''), and their electrical resistivity was not determined. The rates of deposition of these films were 80–100 times higher than those for the films obtained at higher temperatures. Since an x-ray structural analysis revealed no crystal structure in these yellow films, they are probably predominantly amorphous polymer formations of carbon.

It can be seen from Fig. 1 that at low temperatures under conditions of preferential deposition of hydrocarbon polymer films, the crystallite densities decreased almost linearly with increasing temperature. The rates of decrease in the densities and the temperature, described by us as the critical temperature, at which isolated microprotrusions and/or their densities could be identified, ceased to vary and depended on the vapor pressure. The optimum pressure at which the highest density of microprotrusions for all temperatures and the highest critical temperature were observed, was 1 Pa. At the minimum process temperature of 50 °C, the maximum density of microprotrusions was around 1 μm^{-2} for 1 Pa, did not exceed 0.1 μm^{-2} for 5 Pa, and was around 0.01 μm^{-2} for $P=0.05$ Pa (Figs. 2a–e). The critical temperature for these pressures was 250, 200, and 150 °C, respectively, and corresponded to the temperatures at which the transition from the deposition of yellow island-like polymer hydrocarbon films to the deposition of continuous transparent films ended.

An analysis of the x-ray diffraction patterns of samples of the transparent carbon films revealed that these predomi-

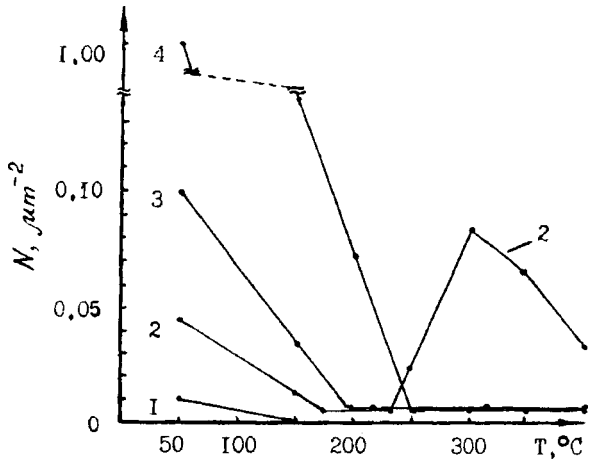

FIG. 1. Crystallite densities versus substrate temperature for various ethanol vapor pressures in an electron-cyclotron-resonance microwave plasma: *1*—0.05 Pa, *2*—0.1 Pa, *3*—5 Pa, and *4*—1 Pa.

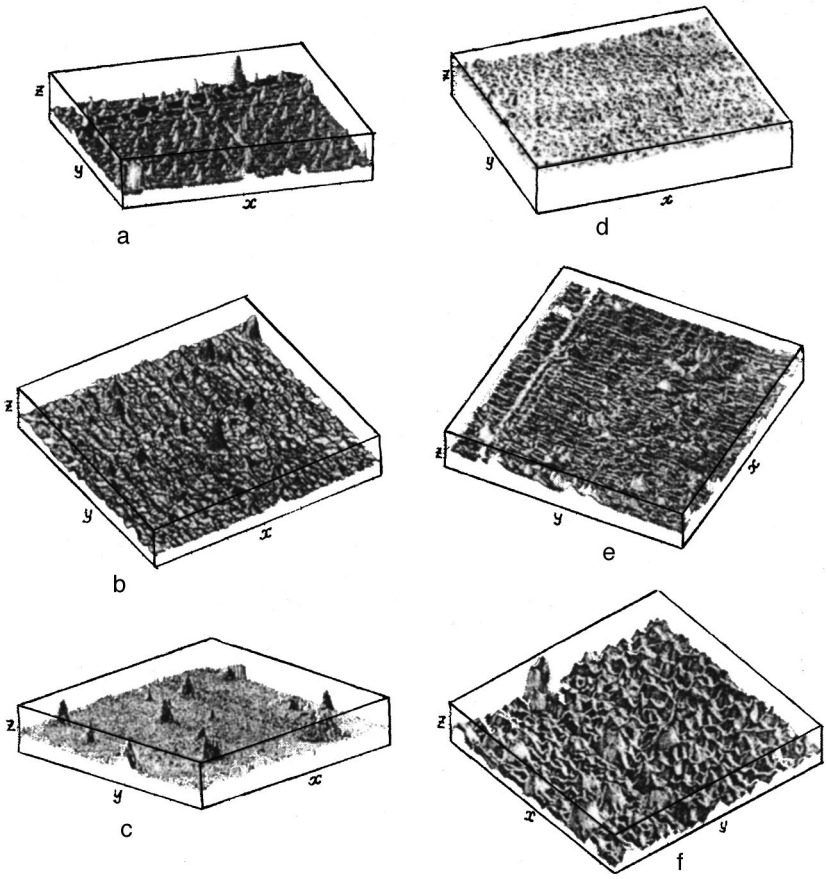

FIG. 2. Typical atomic force microscope images of the microtopography of carbon films obtained in various regimes of electron-cyclotron-resonance microwave plasma deposition: a—polymer: 1 Pa, 50 °C; b—polymer: 5 Pa, 50 °C; c—polymer: 0.1 Pa, 50 °C; *d*—diamond: 1 Pa, 300 °C; e—graphite: 0.1 Pa, 300 °C; f—graphite: 0.05 Pa, 300 °C. Scale: X:1 μm, Y:1 μm, Z:0.01 μm.

nantly contain diamond-like carbon phases with a hexagonal lattice in three different structural modifications (lonsdaleite, C(2OH), and others), they include a (111)-oriented cubic diamond phase, and have small inclusions of the finely crystalline (002) graphite phase. The transparent films possessed high resistivity (up to 10^7 $\Omega \cdot$m) and exhibited good adhesion to the substrate.

For vapor pressures of 0.05 Pa and lower, and above-critical substrate temperatures, the nature of the microprotrusions cannot be identified. This is because at low pressures in the microwave plasma, as the temperature increased, the films were transformed directly from yellow polymer to ''dark'' graphite films (Fig. 2f) whose electrical resistivity did not exceed a few tens of $\Omega \cdot$m. X-ray diffraction patterns of the dark films contain almost no diamond-like phases (except for the C(2OH) phase) but compared with the transparent films, they contain considerably more of the phase which includes (002) finely crystalline graphite with both normal and defect packing of the layers[4]

The temperature dependence of the crystallite density obtained at a vapor pressure of 0.1 Pa is interesting (Fig. 1). Here the maximum crystallite density was identified at a temperature corresponding to the initial stages of the appearance of the dark graphite films (Fig. 2e).

Thus, these experimental results indicate that the deposition of diamond from a microwave gas-discharge plasma with electron cyclotron resonance at low pressures and temperatures is a condensation polymerization process in which various nondiamond modifications of carbon are also formed, these being the products of different chemical reactions which take place in parallel. As a result of various condensation polymerization processes, C–C bonds of a particular polymorphic modification of crystalline carbon (graphite, diamond) or of various macromolecular forms of carbon materials, which do not form a regular crystal lattice, are formed from light, carbon-containing molecules. The initiation of a particular condensation polymerization process depends on the nature of the monomer and characteristics of the kinetic conditions. Depending on these conditions, regimes more favorable for the preferential growth of a particular allotropic carbon phase can be determined.

The formation of a hydrocarbon polymer deposit in a microwave plasma at low temperatures is consistent with known data[5] whereby the condensation of carbon vapor from the gas phase on a cold substrate, activated by an electric discharge, results in the formation of an amorphous carbon layer whose properties differ sharply from those of graphite and more closely resemble those of diamond. Under these conditions, the nucleation and growth of a diamond-like phase is not blocked by the deposition of a graphite film because of the low mobility of the adsorbed carbon atoms, which impedes its ''layered'' growth, and also because of the high solubility of graphite in the atomic hydrogen formed by the dissociation of its molecules in the alcohol vapor of the microwave gas discharge plasma. For these reasons, the density of diamond-phase nuclei at the minimum process temperature of 50° is the highest for all vapor pressures (Fig. 1). Then, in complete agreement with the general theory of the

formation of condensed media from the vapor phase,[6] the number of diamond-like phase nuclei decreases with increasing temperature, their critical size increases, and the deposition of a hydrocarbon film ceases. This can be attributed first to an increased probability of evaporation of atoms from the substrate and second, to the lower evaporation temperature of the polymer hydrocarbon material. The established values of the critical temperatures thus correspond to those temperatures above which atoms of the molecular flux responsible for the formation of the hydrocarbon deposit are completely reflected from the substrate. An increase in the vapor pressure has the result that atoms evaporating from the substrate are trapped by particles of the molecular flux and, being redeposited on the substrate, form condensation nuclei. In addition, an increase in the flux density is accompanied by a reduction in the path length required for the migrating atoms to combine to form critical nuclei. Thus, the critical temperature at which the growth of diamond-like islands is still observed, and also the maximum density of diamond-like phase nuclei will increase with increasing vapor pressure and increasing particle flux density incident on the substrate. The opposite is also true: the lower the flux density, the more rapidly the formation of nuclei of the hydrocarbon and diamond phases of carbon ceases with increasing temperature, as is observed experimentally (curves *1–3* in Fig. 1). An exception to this is the temperature curve of the crystallite density at a vapor pressure of 1 Pa, for which the optimum kinetic conditions for the nucleation and growth of the diamond-like carbon phase are clearly achieved. This regime, as has been determined experimentally, has the highest critical temperature and the highest nucleation density of the diamond-like phase, although the density variation with temperature still shows the same general trend.

The observation of a maximum density of diamond-like phase crystallites at 300 °C for a pressure of 0.1 Pa can be attributed to the same processes of heterogeneous nucleation and growth of films from the gas phase but under conditions of preferential graphite deposition.

[1] A. P. Rudenko and I. I. Kulakova, Vestn. Mosk. Univ. Ser. Khim. **34**, No. 6, (1993).
[2] N. N. Bylinkina, S. P. Mushtakova, V. A. Oleĭnik *et al.*, Pis'ma Zh. Tekh. Fiz. **22**(6), 43 (1996) [Tech. Phys. Lett. **22**, 245 (1996)].
[3] N. N. Bylinkina, S. P. Mushtakova, S. Yu. Suzdal'tsev, and R. K. Yafarov, Pis'ma Zh. Tekh. Fiz. **22**(21), 88 (1996) [Tech. Phys. Lett. **22**, 902 (1996)].
[4] A. R. Ubbelohde and F. A. Lewis, *Graphite and its Crystal Compounds* (Oxford University Press, London, 1960; Mir, Moscow, 1965).
[5] M. D. Blue and G. C. Danielson, J. Appl. Phys. **28**, 583 (1957).
[6] *Thin Films: Interdiffusion and Reactions*, edited by J. M. Poate, K. Tu, and J. Meier (Wiley, New York, 1978; Mir, Moscow, 1982).

Translated by R. M. Durham

Calculation of the optimum parameters of a copper-vapor laser lidar for remote probing of H_2

G. V. Laktyushkin, V. E. Privalov, and V. G. Shemanin

Baltic State Technical University, St. Petersburg
(Submitted November 12, 1996; resubmitted March 18, 1997)
Pis'ma Zh. Tekh. Fiz. **24**, 32–35 (February 26, 1998)

A numerical solution of the lidar equation is obtained for Raman backscattering by hydrogen molecules and the optimum radiation powers of a copper laser are determined at distances of 100–6000 m. © *1998 American Institute of Physics.* [S1063-7850(98)02302-7]

The copper vapor laser is becoming extremely widely used in lidar.[1] The results of Ref. 2 suggest that a copper-vapor laser lidar may be used at wavelengths of 0.5106, 0.2553, 0.5782, and 0.2891 μm with 10 ns pulses (pulse repetition frequency up to 20 kHz) at typical powers $P=10$–150 kW. In the pulse acquisition mode where the signal is recorded by the lidar,[3] a probing distance given by the product $P\sqrt{N}$ may be used.

We obtained a numerical solution of the lidar equation for Raman backscattering by molecules of hydrogen and its isotopes, using copper laser radiation with the parameters given above. The aim of the study is to select the optimum lidar system.

The lidar equation for Raman scattering[4,5] was solved for H_2 molecules. The corresponding wavelengths are given in Table I. The differential cross section for vibrational Raman backscattering was calculated using the well-known formula,[4] which may be simplified to give

$$\frac{d\sigma}{d\Omega}=\frac{A}{\lambda^4}, \tag{1}$$

where the constant A is determined using the known cross section for the wavelength $\lambda_0=488.1$ nm of an argon laser, $(d\sigma/d\Omega)=0.86\times10^{30}$ cm^2/sr, and is $A=4.87138\times10^{12}$ cm^2/sr. For the specific case of our lidar, in the lidar constant K_1 we then isolate the cofactor $\xi_\nu(\lambda)$, which depends on the spectral sensitivity of the photocathode of the photomultiplier, in the form

$$k_1=k_2\xi_\nu(\lambda). \tag{2}$$

The other cofactors in the lidar equation have the following values: distance step $\Delta R=7.5$ m for the measurement time $z=50$ ns, detector area $A_2=0.008$ m^2, $K_2=0.495$ for the 519 nm wavelength, peak laser pulse powers $P_0=1.10$ and 100 kW, probing distance $P=0.1$, 0.5, 1.0, 2.0, 3.0, 4.0, 5.0 and 6.0 km, and molecular concentration 10^{16} cm^{-3}. The spectral sensitivities of the FÉU-79 and FÉU-140 (FÉU-124) photocathodes in the ultraviolet were taken from Ref. 6, and the transmission of the atmosphere was calculated as in Ref. 4 using the formula

$$T(\lambda,R)=\exp\left[-\int_0^R k(\lambda)\cdot dR\right] \tag{3}$$

using the attenuation factors k taken from Ref. 6.

Using the data given above, we calculated the Raman backscattering power using the lidar equation for one of the molecular concentrations, and selected wavelengths and peak powers of the copper laser over a range of probing distances between 0.1 and 6.0 km in order to obtain an optimized lidar system. The results of the calculations for H_2 molecules are

TABLE I. Results of calculations of the Raman backscattering power for H_2 molecules for three wavelengths of a copper laser at powers of 1–100 kW, probing distances of 0.1–6.0 km, and a molecular concentration of 10^{20} cm^{-3}.

km	P_0, kW	1	10	100
0.1	λ, nm	$P(\lambda,R)$, nW	$P(\lambda,R)$, nW	$P(\lambda,R)$, nW
	510	1.646	16.46	164.6
	255	5.439	543.39	543.9
	289	8.928	89.28	892.8
0.5	λ, nm	$P(\lambda,R)$, nW	$P(\lambda,R)$, nW	$P(\lambda,R)$, nW
	510	65.8	0.658	6.58
	255	217.6	2.176	21.76
	289	357.1	3.571	35.71
1.0	λ, nm	$P(\lambda,R)$, nW	$P(\lambda,R)$, nW	$P(\lambda,R)$, nW
	510	16.46	164.6	1.646
	255	54.39	543.9	5.439
	289	89.28	892.8	8.928
2.0	λ, nm	$P(\lambda,R)$, nW	$P(\lambda,R)$, nW	$P(\lambda,R)$, nW
	510	4.11	41.1	0.411
	255	13.60	136.0	1.360
	289	22.32	223.2	2.232
3.0	λ, nm	$P(\lambda,R)$, pW	$P(\lambda,R)$, pW	$P(\lambda,R)$, pW
	510	1.828	18.28	182.8
	255	6.044	60.44	604.4
	289	9.921	99.21	992.1
4.0	λ, nm	$P(\lambda,R)$, pW	$P(\lambda,R)$, pW	$P(\lambda,R)$, pW
	510	1.029	10.29	102.9
	255	3.400	34.00	340.0
	289	5.580	55.80	558.0
5.0	λ, nm	$P(\lambda,R)$, pW	$P(\lambda,R)$, pW	$P(\lambda,R)$, pW
	510	0.658	6.58	65.8
	255	2.176	21.76	217.6
	289	3.571	35.71	357.1
6.0	λ, nm	$P(\lambda,R)$, pW	$P(\lambda,R)$, pW	$P(\lambda,R)$, pW
	510	0.457	4.57	45.7
	255	1.511	15.11	151.1
	289	2.480	24.80	248.0

presented in Table I. It can be seen that an increase in the laser radiation power leads to a proportional increase in the Raman scattering power, while a reduction in the concentration of probed molecules causes a proportional decrease in the Raman scattering power without changing the spectral dependence of the cofactors in the lidar equation. With increasing distance, the Raman scattering signal decreases by two orders of magnitude over the first kilometer, and then by a further two orders of magnitude over the next five kilometers. An analysis of these results shows that 289 nm laser radiation is the optimum for this system, which can give the maximum Raman backscattering power for all the molecules over distances between 0.1 and 6.0 km.

These results therefore demonstrate that an optimum laser wavelength can be selected for probing molecular hydrogen in the atmosphere at a given distance.

[1] V. S. Evtushenko, M. Yu. Kataev, and V. M. Klimkin, Opt. Atmos. Okean. **9**, 777 (1996).
[2] L. P. Vorob'ev, V. S. Evtushenko, V. I. Klimkin *et al.*, Opt. Atmos. Okean. **8**, 1648 (1995).
[3] S. A. Vitsinskiĭ, V. D. Divin, A. V. Keller *et al.*, Opt. Zh. No. 5, 83 (1996).
[4] R. M. Measures, *Laser Remote Sensing: Fundamentals and Applications* (Wiley, New York, 1984; Mir, Moscow, 1987).
[5] *Laser Monitoring of the Atmosphere*, edited by E. D. Hinkley (Springer-Verlag, New York, 1976; Mir, Moscow, 1979).
[6] *Laser Handbook*, edited by A. M. Prokhorov, Vols. 1 and 2 [Russian transl. with changes and additions], Sovet-skoe Radio, Moscow (1978).

Translated by R. M. Durham

Nanostructure of the rapidly quenched magnetic alloy NdFeB

O. A. Velikodnaya, E. I. Lugovskaya, and T. I. Mazilova

''Kharkov Physicotechnical Institute'' National Science Center
(Submitted August 29, 1997)
Pis'ma Zh. Tekh. Fiz. **24**, 36–40 (February 26, 1998)

High-resolution field emission spectroscopy has been used to study the nanostructure of the NdFeB alloy. This revealed a fine banded structure of the grain-boundary phase which is responsible for the high coercivity of the alloy. © *1998 American Institute of Physics.* [S1063-7850(98)02402-1]

Recently NdFeB systems have been used to fabricate permanent magnets with an energy density up to 400 kJ/m^{-3}, which is considerably higher than the theoretical limit for most magnetically rigid materials used previously.[1] Although the nature of the high coercivity of rare-earth metals remains unclear, it has been established that this is associated with extremely small-scale characteristics of the microstructure.[1,2] Here we use one of the highest-resolution structural methods—combined field ion and electron emission microscopy—to study the structure of the alloy NdFeB.[3]

Needle-shaped samples with a radius of curvature of 5–15 nm at the tip were prepared by electrochemical etching from a rapidly quenched $Nd_{11}Fe_{85}B_4$ alloy obtained by a standard technique.[1] The studies were carried out using a double-chamber, low-temperature, ultrahigh-vacuum, field microscope operated in both the ion and electron modes. The required field was generated by applying a positive dc voltage of 10–25 kV and an ac voltage of 6–30 kV to the pointed sample. The amplitude of the ac voltage was selected to produce a field emission current of density 10^3 A/cm^2. Hydrogen at a pressure between 10^{-4} and -10^{-3} Pa was used as the imaging gas. The surface of the samples was polished by field evaporation at an intensity of $1.0-1.05F_e$ where F_e is the threshold field corresponding to? giving a rate of evaporation of 10^{-2} nm/s.

The dependence of the field electron current density J on the local field F is determined by the Fowler–Nordheim equation,[4] from which it follows that

$$\frac{dJ}{J} \cong \varkappa \frac{dF}{F}, \tag{1}$$

where $\varkappa = B\varphi^{3/2}/F$ is the coefficient of field sensitivity of the electron emission.

In our experiments F was varied in the range 3–4 V/nm. Taking φ for the estimates to be the work function of pure iron, 4.4 eV (Ref. 4), we obtain $16 \leqslant \varkappa \leqslant 21$. The high field sensitivity of the electron emission was utilized here to identify comparatively small deviations of the evaporating field F_e caused by ultrasmall-scale characteristics of the alloy structure.

The electric field F_c required for activation-free evaporation of the alloy in the form of n-fold ionized atoms was determined by comparing the threshold evaporation voltages and the voltages giving the best image in the hydrogen ions (2.2×10^{10} V/m). The local field-evaporation energy of the alloy was calculated in the limit of overcoming the barrier created by the superposition of the potential of the image forces of an n-fold ionized atom and the potential of the external electric field:[5]

$$Q_0 = (n^3 e^3 F)^{1/2}, \tag{2}$$

where e is the electron charge.

Most of the samples exhibited a two-phase structure. The magnetically rigid ϕ phases were characterized by a reduced evaporating field strength and the brightness of the image was therefore reduced.[6] Figure 1 shows emission images of the surface of $Nd_{11}Fe_{85}B_4$ alloy obtained by field evaporation in the ion (a) and electron (b and c) modes. The ion image was obtained directly during field evaporation of the surface of the sample at a rate of 10^{-3} nm/s. The electron images of the field-polished surface (Figs. 1b and 1c) were obtained at negative voltages of 1.5 and 1.7 kV, respectively. It can be seen from Fig. 1a that individual atoms and small complexes of them are resolved on the ion images. The electron images exhibit significantly higher contrast and their configuration depends on the electric field strength (Figs. 1b and 1c). The constant-brightness contours of the field electron image correspond to a constant ratio $\varphi^{3/2}/F$. At reduced voltages, the electron-microscopic images reveal a fine structure of a ''bright'' grain-boundary phase surrounding grains of the magnetically rigid $Nd_2Fe_{14}B$ phase and usually identified as Nd_7B_3 (Ref. 6). Bands of enhanced brightness are observed (Fig. 1c and Fig. 2b) which are conserved during prolonged field evaporation. These bands indicate the presence of plate-like inhomogeneities within a neodymium-enriched grain-boundary phase, which are characteristic of the spinoidal decay of rapidly quenched alloys. The system of plates is oriented approximately normal to the boundary with the ϕ-phase. The average distance between the plates is (2.5 ± 1.0) nm and their thickness is 5–8 nm.

The electron images of the surface of magnetically rigid ϕ-phase grains polished by electric field evaporation reveal no emission contrast characteristics which would indicate the presence of intragranular structural and compositional inhomogeneities (Fig. 1). The average diameter of the ϕ-phase grains was (25 ± 6) nm. Around 10% of the grains had di-

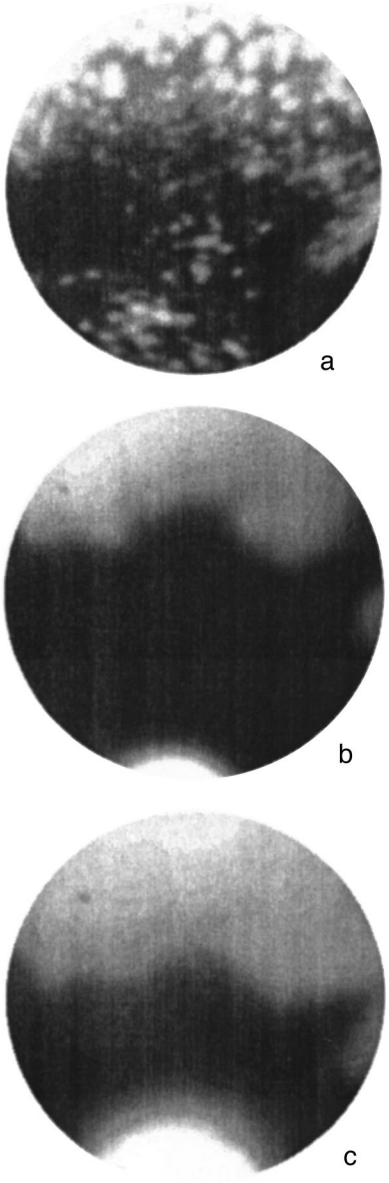

FIG. 1. Field emission photomicrographs of rapidly quenched NdFeB alloy: a—ion image obtained during field evaporation of the sample surface, b and c—electron images of field-polished surface obtained at 1.5 and 1.7 kV, respectively.

mensions exceeding the maximum tip diameter of the needle-shaped sample, ~100 nm. The difference between the local field evaporation energies of the intergranular plates and the material between the plates, calculated using formula (2), was 1.4 eV/atom. This value is clearly substantially greater than the typical values of the specific energies associated with various types of lattice defects. Thus, the observed characteristics of the emission contrast of the grain-boundary phase indicate regular variations in its chemical composition.

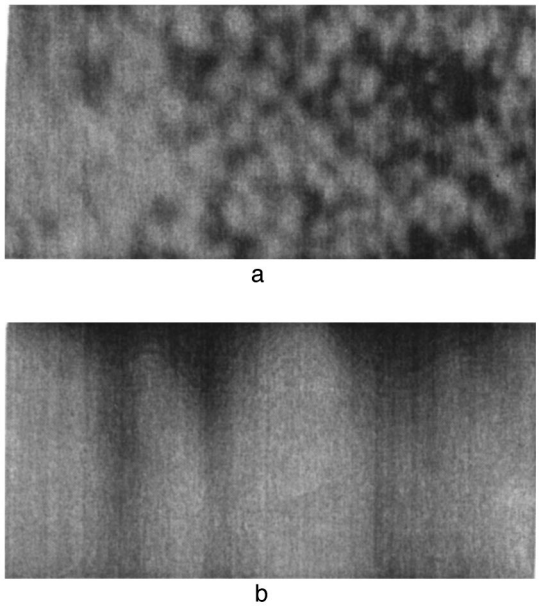

FIG. 2. Ion-microscopic (a) and electron-microscopic (b) images of grain-boundary phase. Traces of parallel plate-like precipitations reaching the surface can be seen

The nanocrystalline structure of the rapidly quenched NdFeB alloy observed in the present study corresponds to a single-domain structure within grains of the main magnetic phase. Significantly, the volume of the resultant inverse magnetic domain, which is determined by the dimensions of the grain-boundary phase plate, is negligible compared with the volume of the entire grain. The uniform contrast of the electron emission images of the magnetically rigid phase grains indicates that there are no intragranular structural and compositional inhomogeneities which could act as pinning centers for the motion of Bloch walls. The fine grain-boundary structure observed in the present study may be attributed to nonequilibrium of the neodymium-enriched phase. These results should be taken into account when constructing a model of nucleation in rare-earth magnetically rigid materials.

[1] K. H. J. Buschow, Rep. Prog. Phys. **54**, 1123 (1991).
[2] H. Kronmuller, K. D. Durst, and M. Sagawa, J. Magn. Magn. Mater. **74**, 291 (1988).
[3] A. S. Bakai, V. B. Kulko, I. M. Mikhailovskij *et al.*, J. Phys.: Condens. Matter **182**, 315 (1995).
[4] A. Modinos, *Field, Thermal, and Secondary Electron Emission Spectroscopy* [in Russian], Nauka, Moscow (1990).
[5] M. Miller and G. Smith, *Probe Analysis in Field Ion Microscopy* [Russian transl.] Mir, Moscow (1993).
[6] A. Hutten and P. Haasen, Acta Metall. Mater. **39**, 1 (1991).

Translated by R. M. Durham

Spontaneous and stimulated emission in microwave oscillators with a virtual cathode

A. E. Dubinov and V. D. Selemir

Russian Federal Nuclear Center, All-Russian Scientific-Research Institute of Experimental Physics, Sarov (Arzamas-16)

(Submitted May 15, 1997)
Pis'ma Zh. Tekh. Fiz. **24**, 41–46 (February 26, 1998)

A one-dimensional model of electron beam emission with a virtual cathode is used to show that spontaneous emission occurs in a reditron while stimulated emission is observed in vircators and negative triodes. However, at a certain stage in the latter, the radiative instability is quenched as a result of the evolution of turbulence in the electron beam. The idea is therefore put forward that this quenching may be eliminated by specially shaping the leading edge of the high-voltage supply pulse to the diode of the microwave oscillator. © *1998 American Institute of Physics.* [S1063-7850(98)02502-6]

The question as to whether spontaneous or stimulated emission occurs in an active electrodynamic system is a key issue for understanding the overall dynamics of a microwave oscillator. For most vacuum and plasma microwave oscillators with high-current electron beams, this issue is fairly well determined.[1] However, for virtual cathode oscillators (such as vircators, negative triodes, and reditrons),[2–4] this issue still remains unresolved.

A one-dimensional model of electron beam emission with a virtual cathode is used to show that spontaneous emission occurs in reditrons, while stimulated emission is observed in vircators and negative triodes. However, at a certain stages in the latter, the radiative instability is quenched as a result of the evolution of turbulence in the electron beam. Thus, the idea was put forward that this quenching could be eliminated by specially shaping the leading edge of the high-voltage pulse supplied to the diode of the microwave oscillator.

We assume that a high-current electron beam is injected through a thin metal foil into a drift tube to which a strong axial magnetic field is applied and we assume that the beam current density is constant in time and given by j_0 (Fig. 1). It is known that if j_0 exceeds a certain critical value j_{cr}, a virtual cathode forms in the beam. It was shown in Ref. 5 that the expression for j_{cr} determined by analyzing the maximum possible steady state of a beam in a drift tube, may be given by

$$j_{cr}=(mc^3/e)(\gamma^{2/3}-1)^{3/2}G, \tag{1}$$

where m and e are the electron charge and mass, c is the velocity of light, γ is the Lorentz factor of the electrons in the injection plane, and G is the geometric form factor.

However, unlike Ref. 5 our analysis is based on the fundamental idea that the critical current density j_{cr} can vary during the evolution of the system, accompanied by the formation of a virtual cathode.

Thus, we consider the current balance in a cross section positioned at a certain distance downstream from the virtual cathode in the direction of the beam motion (Fig. 1). If the difference (j_0-j_{cr}) is not too great, we will have:

—convective current (the frequency Ω is approximately equal to twice the beam plasma frequency in the injection region):

$$j_c=j_{cr}+(j_0-j_{cr})\cos\,\Omega t; \tag{2}$$

—displacement current:

$$j_b=-(j_0-j_{cr})\cos\,\Omega t=\frac{1}{4\pi}\cdot\frac{\partial E}{\partial t}; \tag{3}$$

—total current:

$$j_f=j_c+j_b\equiv j_{cr}. \tag{4}$$

The rest of the electrons (j_0-j_c) are then reflected by the virtual cathode back into the injection plane. In a reditron, where the reflected electrons are immediately absorbed by a foil in the injection plane, this current balance is sustained for an arbitrarily long time.

In vircators and negative triodes, the reflected electrons build up in a ''cathode-virtual cathode'' potential well, creating an electric charge given by (neglecting the losses):

$$q=\int_0^t(j_0-j_c)dt=\int_0^t(j_0-j_{cr})(1-\cos\,\Omega t)dt. \tag{5}$$

As the charge accumulates, the ''degree of suppression'' of the electron beam increases, i.e., j_{cr} decreases. We do not know of any accurate expression for the dependence of j_{cr}

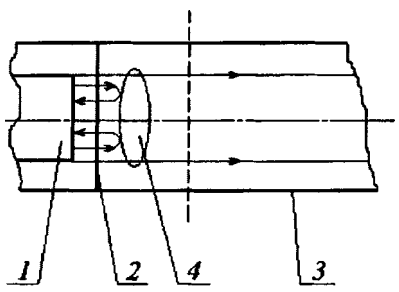

FIG. 1. Geometry of the problem: *1*—cathode, *2*—anode foil, *3*—drift tube, and *4*—virtual cathode (the cross section studied is indicated by the dashed line.

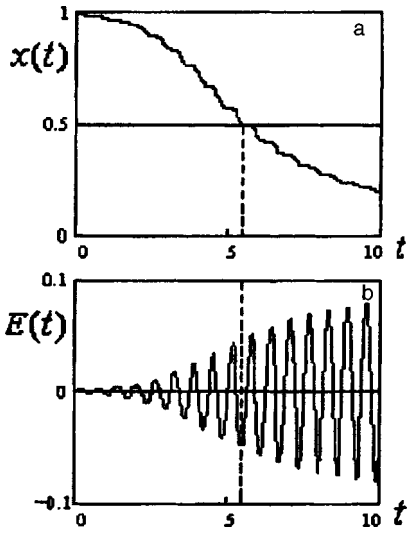

FIG. 2. Evolution of the system with constant injection current: a—$x(t)=j_{cr}(t)/j_0$; b—$E(t)$.

on the accumulated charge q. However, we can draw some general conclusions on this dependence: a it decreases monotonically with $j_{cr}=\infty$ for $q=0$ while $j_{cr}=0$ for $q=\infty$. Thus, we can qualitatively assume

$$q=G' j_{cr}^{-p}, \tag{6}$$

where G' is a certain geometric form factor and $p=\text{const}$.

Substituting Eq. (6) into Eq. (5) and differentiating, we obtain an equation for $x=j_{cr}/j_0$:

$$\frac{dx}{dt}=\frac{x^{p+1}}{pG'}(x-1)(1-\cos\,\Omega t). \tag{7}$$

Equation (7) has the steady-state solution $x=1$. However, this solution is unstable, since for $x(0)=1-\delta$, for small δ the function x diverges rapidly from its initial value. Equation (7) was solved numerically by a fourth-order Runge-Kutta method for various values of p, G', Ω, and δ. The typical evolution of $x(t)$ is plotted in Fig. 2a. The solution of Eq. (7) may be substituted into Eq. (3) to give the evolution of the electric field. In normalized form, we have

$$E(t)=\int_0^t (1-x)\cos\,\Omega t dt. \tag{8}$$

The evolution of $E(t)$ was calculated numerically and is plotted in Fig. 2b. This shows that, as was to be expected (see the qualitative reasoning on phase separation presented in Refs. 2 and 3), radiative instability with stimulated emission develops in an electron beam with a virtual cathode in a vircator and a negative triode, while spontaneous emission is observed in a reditron.

It should be noted that our model of stimulated emission ceases to hold for $x<1/2$ since at certain times $j_c<0$ is then found, which corresponds to return motion of the electrons. Quite clearly, $x<1/2$ corresponds to vortices of the electron beam in longitudinal turbulence[6] which is responsible for quenching of the radiative instability (the time at which x passes through 1/2 is indicated by the dashed line in Fig. 2).

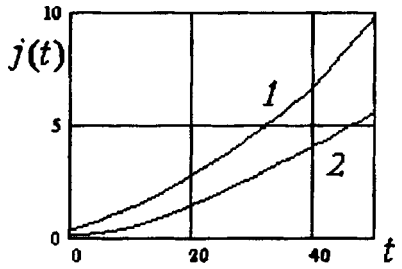

FIG. 3. Evolution of the system with a profiled pulse leading edge: *1*—$j_0(t)$; *2*—$j_{cr}(t)$.

However, this quenching can be avoided by specially shaping the leading edge of the high-voltage supply pulse. The criterion for this profile is that the instantaneous value of the injected current j_0 should not be more than twice the instantaneous value of the critical current j_{cr}. Then, if j_{cr} and j_0 increase synchronously (for example, so that $j_0\approx 1.8 j_{cr}$), in accordance with Eq. (3), the amplitude of the electric field will increase.

Since in the nonrelativistic approximation in the diode of a microwave oscillator we usually find

$$j_0=SU^{3/2}, \tag{9}$$

where S is the perveance of the diode and U is the applied voltage, the oscillation frequency Ω will depend linearly on U. As a result of simple calculations, we obtain a differential equation for j_{cr} for a given profile $U(t)$ similar to Eq. (7):

$$\frac{dj_{cr}}{dt}=\frac{3}{2}\frac{j_{cr}}{pU}\frac{dU}{dt}+\frac{(j_{cr}-SU^{3/2})j_{cr}^{p+1}}{pG''U^{3/2}}(1-\cos\,AUt). \tag{10}$$

Here G'' and A are certain geometric form factors. By selecting $U(t)$, we can find j_0 and j_{cr} from Eqs. (9) and (10), respectively, so that j_0 and j_{cr} increase rapidly and the required relation between them is satisfied. We were able to select several variants of the parameters S, G'', and A for $p=1$ for an exponential voltage pulse profile $U(t)$ in the diode for which the condition $j_0\leqslant 2j_{cr}$ can be satisfied over a fairly long time. As an example Fig. 3 shows one of these variants as graphs of j_0 and j_{cr}. Thus, in a vircator and in a negative triode, stimulated emission can be sustained for almost the entire supply pulse.

[1] M. V. Kuzelev and A. A. Rukhadze, *Electrodynamics of Dense Electron Beams in Plasma* [in Russian], Nauka, Moscow (1990).
[2] B. V. Alyokhin, A. E. Dubinov, V. D. Selemir *et al.*, IEEE Trans. Plasma Sci. **22**, 945 (1994).
[3] A. E. Dubinov and V. D. Selemir, Zarub. Radioelektron. No. 4, 54 (1995).
[4] A. A. Rukhadze, S. D. Stolbetsov, and V. P. Tarakanov, Radiotekh. Elektron. **37**, 385 (1992).
[5] L. S. Bogdankevich and A. A. Rukhadze, Usp. Fiz. Nauk **103**, 609 (1971) [Sov. Phys. Usp. **14**, 163 (1971)].
[6] V. E. Vatrunin, A. E. Dubinov, V. D. Selemir, and N. V. Stepanov, in *Fractals in Applied Physics*, edited by A. E. Dubinov [in Russian], Arzamas-16 (1995), p. 47.

Translated by R. M. Durham

Investigation of superconducting crystals by neutron scattering and nuclear microanalysis

G. A. Evmenenko, V. M. Lebedev, V. T. Lebedev, A. I. Sibilev, and S. A. Churin

B. P. Konstantinov Petersburg Institute of Nuclear Physics, Russian Academy of Sciences, Gatchina
(Submitted July 1, 1997)
Pis'ma Zh. Tekh. Fiz. **24**, 47–51 (February 26, 1998)

A combination of nuclear microanalysis (ion x-ray spectral analysis, Rutherford backscattering, and nuclear reactions) with low-angle neutron diffraction in the bulk of a Y-Ba-Cu-O ceramic rod, recrystallized by zone refining, was used to determine the elemental and phase composition of the initial ceramic, the crystal, and the transition sections. The degree of local homogeneity of the medium was also determined at scales of $\sim 10^1 - 10^2$ nm. © *1998 American Institute of Physics.* [S1063-7850(98)02602-0]

A problem in the technology of high-temperature superconductors is to obtain long crystals with a high critical current. A rod of the required length and cross section is prepared from $YBa_2Cu_3O_x$ ceramic by powder technology (Fig. 1). Melting and crystallization of the blank is carried out in a vertical furnace. As the ceramics melt, they decompose to form solid (Y_2BaCuO_5) and liquid ($\mathscr{L}$: $BaCuO_2$ and CuO) components. The crystals are grown by the peritectic reaction $Y_2BaCuO_5 + \mathscr{L} = YBa_2Cu_3O_x$ in a thermal field with a gradient of 20–50 °C/cm at 1010–1005°. The velocity of the rod in the furnace is 1×10 mm/h^{-1}. Crystals of $YBa_2Cu_3O_x$ several centimeters long with a critical current density $j_c = 10^4 - 10^5$ A/cm^2 at $B = 0$ T and $T = 77$ K were grown at the Institute of Metal Physics of the Russian Academy of Sciences.[1] However, during crystallization the colder upper part of the blank becomes coated with a layer of $BaCuO_2$ with traces of CuO, which leads to shrinkage, loss of stoichiometry, and termination of crystal growth. The lower part is enriched in the Y_2BaCuO_5 phase. There is thus a need to monitor the elemental composition and microproperties of the various parts of the blank during the crystal growth process.

We used nondestructive methods of nuclear microanalysis to determine the elemental composition of the target. The analysis was carried out using the ESU-2 electrostatic accelerator at the St. Petersburg Institute of Nuclear Physics. The elemental composition of yttrium, barium, and copper was determined by Rutherford backscattering and x-ray spectral analysis with proton-excited fluorescence (relative error $\sim 1\%$). The oxygen content in the samples was determined relative to a standard sample using the $^{16}O(d,p)^{17}O$ nuclear reaction.[2] The energies of the accelerated protons and deuterons were $E_p \sim 1$ MeV and 0.9 MeV, respectively, with $\Delta E/E \sim 10^{-4}$. The elemental and phase compositions are presented in Table I. To complete the picture, we investigated another crystal cut from a similar rod (target 2). For these methods, the thickness of the surface layer investigated in the samples is ~ 20 μm.

The crystal (position *2*) is enriched in the $BaCuO_2$ phase, whereas target 2 is enriched in Y_2BaCuO_5 and $BaCuO_2$. The surface layer at positions *3*, *4*, and *5* consists mainly of $BaCuO_2$, which is consistent with data given in Ref. 3.

At position *2* on the rod, and for target 2 in certain positions relative to the direction of the deuteron beam from the accelerator, the proton spectrum (products of the nuclear reaction between deuterons and ^{16}O oxygen) at low energies reveals an intensity dip—deuteron channeling (Fig. 2), which indicates crystallinity in the samples (position *2* on the rod and target 2).

We used low-angle neutron diffraction at the wavelength

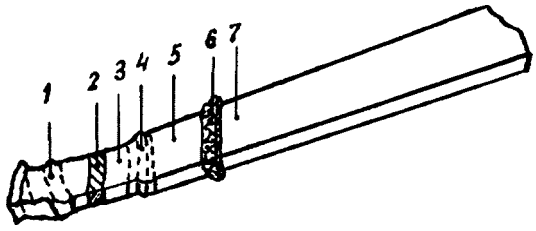

FIG. 1. Sample showing monitoring positions: *1*, *3*, *4*, and *5*—liquid component, *2*—crystal, *6*—transition region, and *7*—initial ceramic.

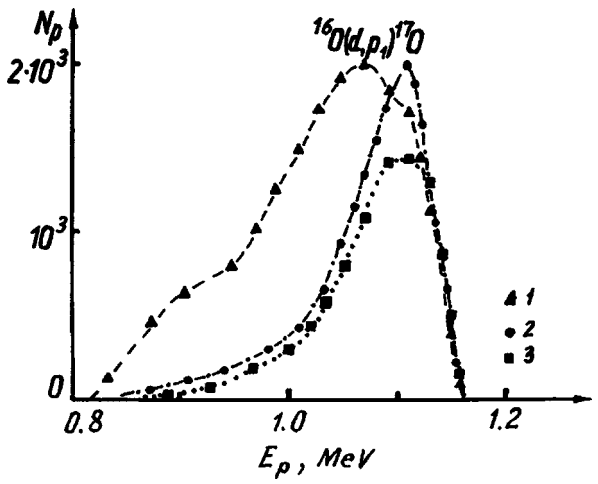

FIG. 2. Proton spectrum using the $^{16}O(d,p_1)^{17}O$ reaction for random (*1*) and oriented (*2*—position *2* in Fig. 1, *3*—target 2) incidence of deuterons on the crystal target.

TABLE I. Elemental and phase composition of samples.

Position	Elemental content in atomic ratios				Phases
	Y	Ba	Cu	O	
1	0.034	1	1.13	2.20±0.02	$(BaCuO_2)+0.036(YBa_2Cu_3O_{6.98})$
2, cryst.	0.90	2	2.91	6.71±0.07	$(YBa_2Cu_3O_{6.98})+0.23(BaCuO_2)$
3	0.056	1	1.07	2.10±0.02	$(BaCuO_2)+0.063(YBa_2Cu_3O_{6.98})$
4	-	1	1.04	2.05±0.02	$(BaCuO_2)+0.04(CuO)$
5	-	1	1.04	2.08±0.02	$(BaCuO_2)+0.04(CuO)$
6	0.134	2	3.05	5.30±0.06	$(BaCuO_2)+0.54(CuO)$ $+0.034(Y_2BaCuO_5)$
7, initial	1.01	2	2.94	6.89±0.07	$(YBa_2Cu_3O_{6.97})+0.018(Y_2BaCuO_5)$
Target 2, cryst.	1.31	2	2.77	7.05±0.07	$(YBa_2Cu_3O_{6.96})+0.19(BaCuO_2)$ $+0.35(Y_2BaCuO_5)$

$\lambda \approx 0.3$ nm ($\Delta\lambda/\lambda \approx 30\%$) to determine microinhomogeneities in the sample. The neutron scattering for imparted momenta $\mathbf{q}=0.05-0.8$ nm^{-1} was measured at several positions on the sample (Fig. 3) and for target 2. Also plotted are the results of approximating the dependence of the scattered neutron intensity (I) on the imparted momentum (q): $I(\mathbf{q}) \sim \mathbf{q}^{-d}$, where the exponent d characterizes the fractal dimension of the object at scales of 10^1-10^2 nm. For the initial ceramic (position *7*) we obtain $d=4.03\pm0.03$, for the intermediate region (position *4*) $d=3.41\pm0.05$, and for the crystal (position *2*) $d=3.23\pm0.03$. For target 2 we obtained a value close to three, $d=3.19\pm0.04$.

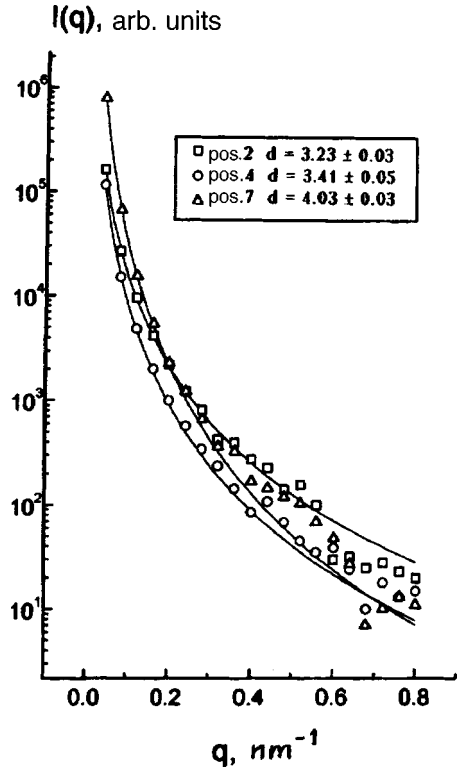

FIG. 3. Investigation of microinhomogeneities by neutron diffraction at positions *2*, *4*, and *7*. The approximating functions are shown together with the parameters d characterizing the fractal dimension of the object at scales of 10^1-10^2 nm.

Thus, the ceramic part of the sample has a well developed granular surface with the dimension $6-d \approx 2$, which gives the Poroda scattering law $I(\mathbf{q}) \sim \mathbf{q}^{-4}$. The exponent $d \approx 3$ indicates a dense medium (polycrystal). The transition region has an intermediate dimension d. These results agree with the elemental and phase composition data and explain the observed deuteron channeling effect (Fig. 2).

These investigations have shown that it is effective to combine low-angle neutron scattering and nondestructive surface-sensitive methods of nuclear microanalysis (Rutherford backscattering, nuclear reactions, ion x-ray spectral analysis, and channeling) to monitor the growth of high-temperature superconducting crystals and optimize their production technology, and to study other similar objects.

This work was carried out as part of the Federal Program ''High-Temperature Superconductivity'' (Grants 96021 and 95032) and was supported by the State Scientific and Technical Program ''Neutron Studies of Materials.''

[1] I. F. Voloshin, L. M. Fisher, Yu. V. Drozov, and S. A. Churin, *Abstracts of Papers presented at 30th Conference on Physics of Low Temperatures, 1994, Part 1* [in Russian], p. 70.

[2] O. I. Kashtanova, V. M. Lebedev, and V. A. Smolin, *Abstracts of Papers presented at Fourth All-Russia Conference on Modification of Properties of Structural Materials by Charged Particle Beams, Tomsk, 1996* [in Russian], pp. 487–489.

[3] S. A. Churin, Pis'ma Zh. Tekh. Fiz. **21**(10), 53 (1995) [Tech. Phys. Lett. **21**, 375 (1995)].

Translated by R. M. Durham

Removal of nitrogen oxides from the air under the action of a microsecond electron beam

G. V. Denisov, Yu. N. Novoselov, and R. M. Tkachenko

Institute of Electrophysics, Ural Branch of the Russian Academy of Sciences, Ekaterinburg
(Submitted September 10, 1997)
Pis'ma Zh. Tekh. Fiz. **24**, 52–56 (February 26, 1998)

The oxidation of nitrogen oxides in a model mixture ionized by a microsecond pulsed electron beam has been investigated experimentally and results are presented. It is shown that when the mixture has a high impurity content, the energy dissipated in the removal of a single toxic molecule is substantially lower than the dissociation energies of nitrogen monoxide and molecular oxygen, being ~ 2 eV. © *1998 American Institute of Physics.* [S1063-7850(98)02702-5]

Oxides of nitrogen NO_x present in large quantities in flue gases discharged from thermal power stations are a major cause of acid rain. At the present time, electrophysical methods of purifying these flue gases are being intensively investigated. These methods involve using electric discharges and electron beams to ionize various types of gas. Reactions to form free radicals such as O, OH, and O_2H take place in this ionized moist gas and these radicals react with nitrogen oxides to form nitric acid. When ammonia is added, the acid forms NH_4NO_3 ammonium salts in solid powder form, which can be removed by various types of filters.[1,2]

From the point of view of obtaining low energy consumption, it is efficient to use electron beams. Continuous accelerators delivering electron beams with current densities of 10^{-9}–10^{-5} A/cm^2 are used for this purpose since they have reached a sufficient level of technical development. These beams give a high degree of purification from nitrogen oxides—up to 98–100%, with the energy dissipated in removing a single toxic molecule being 15–20 eV (Ref. 4). In earlier studies using oxides of sulfur and carbon disulfide[5,6] we demonstrated that the use of pulsed beams can substantially reduce the energy consumption by several factors. It is therefore interesting to examine the possibility of using pulsed beams to remove oxides of nitrogen.

Here we present results of experiments to study the removal of NO and NO_2 molecules from a model mixture exposed to a microsecond pulsed electron beam. Characteristics of the removal of impurities from an air mixture were investigated as a function of their concentration. The experiments were carried out using apparatus similar to that described in Ref. 5. The electron accelerator delivered a radially diverging beam with pulse length of 40 μs, electron energy 250–300 keV, and maximum current density $\sim 10^{-3}$ A/cm^2. The cross section of the beam extracted beyond the foil was 1.44 m^2 and the irradiated volume was 170 liter.

A model mixture containing 10% oxygen, up to 87% nitrogen, 3% water vapor, and between 500 and 6000 ppm oxides of nitrogen was irradiated. The impurity concentration was measured by a conductometric method similar to that used in Ref. 5. The measurement error did not exceed 1%.

During the experiments we determined the absolute change in the concentration of nitrogen oxides and the degree of purification, and also the energy expended in the removal of a single toxic molecule. The degree of purification η and the energy ε dissipated in the removal of a single toxic NO molecule were calculated as

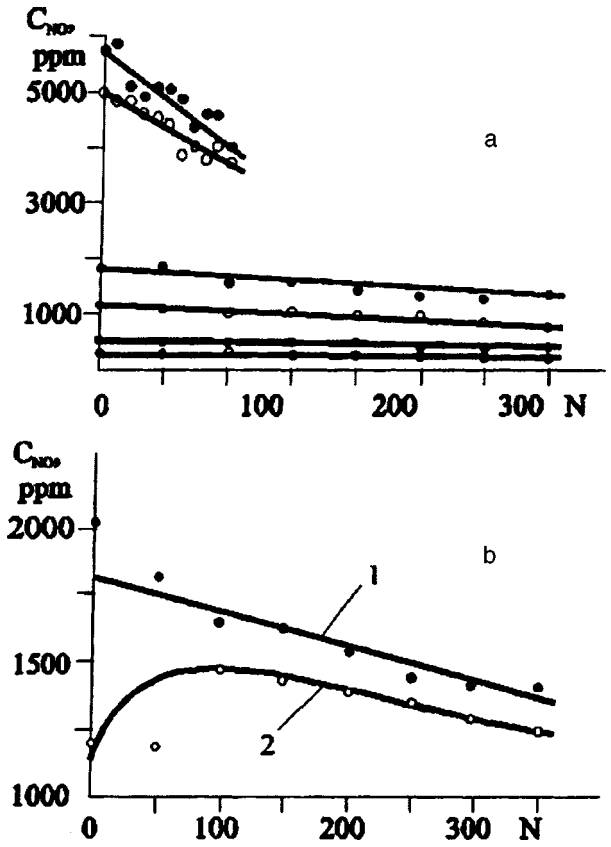

FIG. 1. a—Change in NO concentration versus number of irradiating pulses N; b—change in NO (*1*) and NO_2 (*2*) concentrations versus number N of irradiating pulses.

$$\eta = \Delta[\mathrm{NO}]/[\mathrm{NO}]_0,$$

$$\varepsilon = jD\tau n/e\Delta[\mathrm{NO}](\mathrm{eV/molecule}).$$

Here $\Delta[\mathrm{NO}]$ is the change in the concentration of nitrogen oxides after a series of radiation pulses (cm^{-3}), $[\mathrm{NO}]_0$ is the initial impurity concentration in the mixture (cm^{-3}), j and τ are the beam current density ($\mathrm{A/cm}^2$) and its duration (s), D is the energy dose absorbed by the gas per unit length (eV/cm), n is the number of pulse in an irradiation series, and e is the electron charge (C).

The product $j\tau$ was determined by integrating oscilloscope traces of the beam current pulses and D was measured experimentally by a standard technique using film dosimeters. The measured value of D was compared with that calculated by the Monte-Carlo method. The results of the measurements and calculations differ by no more than 10%. The total measurement error for ε did not exceed 0.3.

The main problem in the removal of oxides of nitrogen is the oxidation of NO to give NO_2 since when water vapor is added to the gas, the NO_2 molecules undergo fairly rapid oxidation to give nitric acid without additional electron beam irradiation of the gas. Figure 1a gives the change in the concentration of nitrogen monoxide as a function of the number n of radiation pulses. It can be seen that the NO concentration decreases linearly with increasing number of pulses. At the same time, attention is drawn to the fact that the rate of decrease in the NO concentration depends on the initial impurity content. Figure 1b gives the NO and NO_2 concentrations as a function of the number of radiation pulses. Whereas a linear dependence is observed for nitrogen monoxide, the behavior of the NO_2 concentration deviates from linear. Under the action of the electron beam on the air, NO becomes oxidized to give NO_2 whose concentration increases with the number of radiation pulses. Subsequently, the NO_2 concentration, like the NO, decreases. This indicates that electron beam ionization of the gas increases the rate of NO oxidation.

The energy characteristic of the process of nitrogen oxide removal is the energy expended in oxidizing a single impurity molecule. Figure 2 gives the dissipated energy ε as a function of the initial NO concentration in the mixture (curve *1*) together with the degree of purification η (curve *2*). The number of radiation pulses was 300 for each point. The

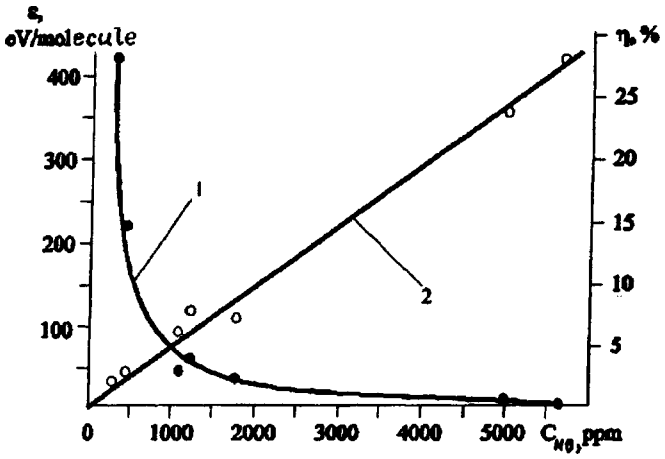

FIG. 2. Dissipated energy ε (*1*) and degree of purification η (*2*) versus initial NO impurity concentration.

change in the dissipated energy ε reflects the curves plotted in Fig. 1a. At low NO concentrations, ε is appreciable, a few tens of electron volts per molecule. For example for $[\mathrm{NO}]_0 \sim 1000$ ppm, the dissipated energy is ~ 50 ev/molecule. An increase in $[\mathrm{NO}]_0$ reduces the value of ε. For example, when the initial concentration of nitrogen monoxide is 5500 ppm, ε is reduced to ~ 2 eV. For comparison we note that the dissociation energy of the NO molecule is 6.5 eV and the dissociation energy of molecular oxygen is 5.12 eV (Ref. 7).

To conclude, it has been shown that microsecond electron beams can oxidize nitrogen oxide impurities, present in air in large quantities, with a low energy consumption.

This work was carried out under the International Scientific-Technical Center Project No. 271.

[1] S. Masuda, Pure Appl. Chem. **60**, 727 (1988).
[2] E. L. Neau, IEEE Trans. Plasma Sci. **22**, 2 (1994).
[3] N. Frank and S. Hirano, Radiat. Phys. Chem. **35**, 416 (1990).
[4] J. C. Person and D. O. Ham, Radiat. Phys. Chem. **31**, 1 (1988).
[5] D. L. Kuznetsov, G. A. Mesyats, and Yu. N. Novoselov, Teplofiz. Vys. Temp. **34**, 845 (1996).
[6] G. V. Denisov and Yu. N. Novoselov, Pis'ma Zh. Tekh. Fiz. **22**(7), 11 (1996) [Tech. Phys. Lett. **22**, 270 (1996)].
[7] A. A. Radtsig and B. M. Smirnov, *Reference Data on Atoms, Molecules, and Ions* [Springer-Verlag, Berlin, 1985; Énergoatomizdat, Moscow, 1986].

Translated by R. M. Durham

Efficient electric-discharge CO_2 laser with a prepulse formed by a generator with an inductive energy storage device

E. Kh. Baksht, V. M. Orlovskiĭ, A. N. Panchenko, and V. F. Tarasenko

Institute of High-Current Electronics, Siberian Branch of the Russian Academy of Sciences, Tomsk
(Submitted July 29, 1997)
Pis'ma Zh. Tekh. Fiz. **24**, 57–61 (February 26, 1998)

Results are presented of experimental investigations of a CO_2 laser pumped by a self-sustained discharge from a generator with an inductive energy storage device and a semiconductor current chopper. It is shown that the energy stored in the inductance of the discharge circuit can form a prepulse capable of depositing most of the energy in the active mixture for near-optimum values of the parameter E/p. A radiation energy of 3 J was achieved in an electric-discharge laser with a 0.181 liter active volume with a 17% efficiency relative to the energy stored in the capacitive storage device. © *1998 American Institute of Physics.* [S1063-7850(98)02802-X]

1. Electric-discharge CO_2 lasers are now being increasingly widely used in various fields of science and engineering. It is therefore of topical scientific and technical interest to improve these lasers still further, and especially to enhance their efficiency. It is known that efficient electric discharge pumping of CO_2 lasers involves conserving discharge uniformity and sustaining the optimum parameter E/p (E is the electric field strength and p is the gas pressure) over the discharge gap in the range $5<E/p<15$ V/cm·Torr, depending on the mixture composition and the pump duration.[1] The range of E/p corresponds to a voltage across the laser gap below the static breakdown voltage[2] and is usually achieved by pumping with a self-sustained discharge for a short time at low currents. Thus, atmospheric-pressure electric-discharge pulsed lasers generally have efficiencies of 5–12% (Refs. 2 and 3). The parameter E/p may be reduced during the exciting pulse by decreasing the charging voltage, but for self-sustained discharge pumping this substantially reduces the energy deposited in the active mixture and may lead to contraction of the discharge. Contraction can be avoided and the deposited energy increased at reduced E/p by using profiled electrodes, which generate a uniform field in the discharge gap, and using a high initial electron concentration from an external ionizer. Intense ultraviolet radiation,[4–6] high-voltage prepulse shaping systems,[7,8] and an electron beam[9] have all been used as ionizers. However, when the ultraviolet radiation intensity increases, the energy expended on preionization becomes comparable with the energy deposited in the active medium from the main storage system and the overall laser efficiency does not increase, remaining $\leqslant 10\%$ (Ref. 3). High-voltage prepulse shaping systems are fairly complex and have not been widely used. The highest CO_2 laser efficiencies have been achieved by pumping with an electron-beam-controlled nonself-sustained discharge[10] but the advantages of this pumping method are only manifest is comparatively large systems with radiation energies higher than 100 J, for which biological shielding is required.

Here we report for the first time the development of an efficient electric-discharge CO_2 laser in which the discharge is formed using a prepulse from a generator with an inductive energy storage system and semiconducting current chopper. We previously used a similar type of generator to pump other types of pulsed lasers (XeCl, nitrogen, Penning plasma neon, and nonchain HF lasers).[11,12]

2. The electrical circuit and the laser design were similar to those used in Ref. 12. The active volume was $V=1\times 3.3\times 55$ cm (interelectrode gap $d=3.3$ cm). Preionization was provided by ultraviolet radiation from a barrier discharge which was formed below a grid anode by discharging a capacitor $C_p=3$ nF. SDL-0,4-800 semiconductor diodes, operated in the current chopping mode, were installed parallel to the laser gap. The capacitances and charging voltage in the circuit where current was preliminarily passed in the forward direction through the semiconducting diodes (buildup circuit) and in the main circuit were $C_0=10$ nF and $C_1=45$ or 90 nF, $U_0=20$ kV and $U_1=15-30$ kV, respectively. The time for preliminary passage of current through the chopper, which is equal to the half-period of the current oscillation in the buildup circuit, was taken to be 800 ns, with the transmitted current being an order of magnitude lower than that in the main circuit. The current pulses in the discharge circuits, the voltages across the laser gap, and the laser radiation pulses were recorded using shunt resistances, a voltage divider, and an FSG-0.22 photodetector, respectively, from which the signals were fed to an S8-14 oscilloscope. The radiation energy was measured with an IKT-1N calorimeter. The active mixtures, consisting of carbon dioxide, nitrogen, and helium, were prepared directly in the laser chamber. The cavity was formed by a spherical copper mirror with $R=5$ m and a plane-parallel KRS-5 plate.

3. The main results are illustrated in Figs. 1 and 2. The inductive energy storage device produced voltage pulses with a steep leading edge and maximum amplitude $U=3U_0$, which could generate a volume discharge in the laser gap at mixture pressures up to 0.5 atm and charging voltages of the capacitative storage device below the static breakdown level.

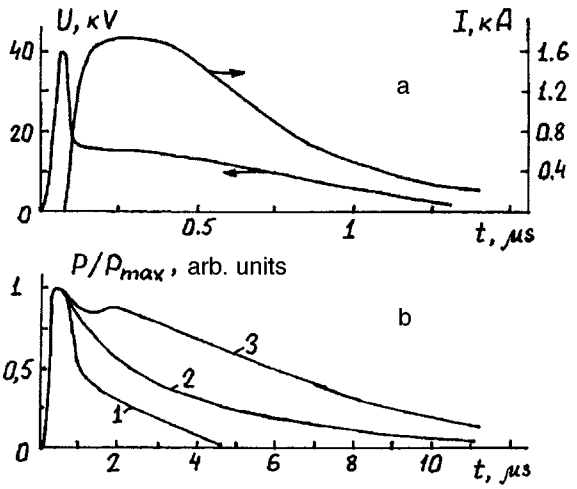

FIG. 1. Oscilloscope traces of voltage pulses across laser gap, discharge current (a) and radiation (b). Mixture He:CO_2:N_2=3:1:1 at p=0.3 atm, C_1=90 nF, and U_1=17 kV (a). Mixtures He:CO_2:N_2=3:1:1 (*1*), He:CO_2:N_2=3:0.7:1.4 (*2*), and He:CO_2:N_2=3:0.4:1.6 (*3*) at p=0.4 atm, C_1=45 nF, and U_1=30 kV (b).

After the volume discharge is ignited, the voltage across the gap drops rapidly, and most of the energy is deposited in the laser active medium within 1.5–2 μs at near-optimum E/p (Fig. 1a). Under these conditions, the maximum operating efficiency of the CO_2 laser was improved to 17% and the pulse radiation energy increased to 3 J (Fig. 2). It should be noted that with this pumping system the duration of the lasing pulses could easily be varied between 4 and 14 μs by varying the nitrogen content in the active mixture (Fig. 1b). Under optimum conditions the delay time of the lasing pulse relative to the discharge current pulse was $\sim$1 μs. When the storage capacitor was reduced, the charging voltage had to be increased considerably to achieve a radiation energy of 2–3 J which increased the voltage across the gas-discharge plasma during pumped and reduced the laser efficiency to $\sim$10%. The same efficiency was obtained by using a normal pumping system with storage and peaking capacitors.

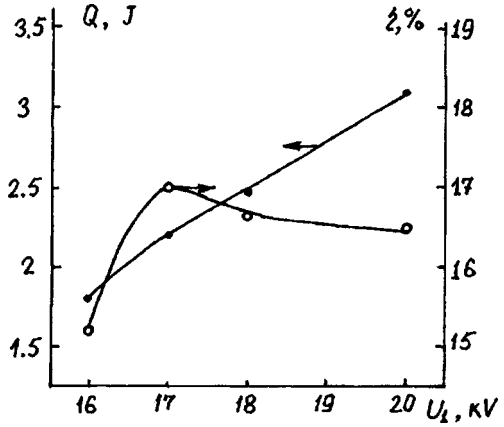

FIG. 2. Radiation energy and efficiency of CO_2 laser versus charging voltage. Mixture He:CO_2:N_2=3:1:1 at p=0.3 atm, C_1=90 nF, and U_1=17 kF.

4. To conclude, we note that a radiation energy of 3 J and an efficiency of 17% relative to the energy stored in the capacitative storage systems has been achieved using an electric-discharge laser with an active volume $V=1\times3.3\times55$ cm, pumped by a generator with an inductive energy storage device and a semiconducting current chopper. It has been shown that the energy stored in the discharge-circuit inductance is used to form a prepulse which can deposit most of the energy into the active mixture at near-optimum values of E/p. It may be predicted that CO_2 lasers pumped by a self-sustained discharge from a generator with an inductive energy storage system and semiconducting current choppers will in future have extensive practical applications.

[1] A. N. Lobanov and A. F. Suchkov, Kvantovaya Elektron. (Moscow) **1**, 1527 (1974) [Sov. J. Quantum Electron. **4**, 843 (1974)].
[2] V. Vitteman, *CO_2 Lasers* [Russian trans.], Mir, Moscow (1990).
[3] G. A. Mesyats, V. V. Osipov, and V. F. Tarasenko, *Pulsed Gas Lasers* (SPIE Press, Washington, 1995).
[4] R. C. Lind, G. Y. Wada, C. I. Dunming *et al.*, IEEE J. Quantum Electron. **QE-10**, 818 (1974).
[5] J. S. Levin and A. Javan, Appl. Phys. Lett. **22**, 55 (1973).
[6] E. J. Morikava, Appl. Phys. **48**, 1229 (1977).
[7] Yu. I. Bychkov, V. V. Osipov, and V. A. Tel'nov, Prib. Tekh. Éksp. No. 4, 165 (1981).
[8] A. M. Orishich, A. G. Ponomarenko, and R. I. Soloukhin, *Gas Lasers* [in Russian], Nauka, Novosibirsk (1977), pp. 298–302.
[9] B. M. Koval'chuk, V. V. Kremiev, and G. A. Mesyats, Dokl. Akad. Nauk SSSR **191**, 76 (1970) [Sov. Phys. Dokl. **15**, 267 (1970)].
[10] S. P. Bugaev, Yu. I. Bychkov, E. K. Karlova *et al.*, Pis'ma Zh. Tekh. Fiz. **1**, 492 (1975) [Sov. Tech. Phys. Lett. **1**, 226 (1975)].
[11] A. N. Panchenko and V. F. Tarasenko, Kvantovaya Elektron. (Moscow) **17**, 32 (1990) [Sov. J. Quantum Electron. **20**, 24 (1990)].
[12] M. I. Lomaev, A. N. Panchenko, and V. F. Tarasenko, Kvant. Elektron. (Moscow) **24**, 499 (1997).

Translated by R. M. Durham

Pyroelectroluminescence of barium beta borate single crystals

V. T. Adamiv, Ya. V. Burak, M. R. Panasyuk, and I. M. Teslyuk

Institute of Physical Optics, Lvov, Ukraine
(Submitted July 29, 1997)
Pis'ma Zh. Tekh. Fiz. **24**, 62–65 (February 26, 1998)

Investigations were made of the pyroluminescence properties of barium beta borate single crystals. The measurements were made at air pressures of 1–10 Pa and temperatures of 80–400 K. Luminescence was observed as isolated flashes over the entire range of experimental conditions. It was observed that the light flashes coincided with the pyrocurrent oscillations.
 [S1063-7850(98)02902-4]

Barium metaborate BaB_2O_4 can exist in two modifications: the low-temperature noncentrosymmetric β-phase with space group $3m$ and the high-temperature centrosymmetric α-phase with space group $\bar{3}m$, with a phase transition at 1198 ± 5 K (Refs. 1 and 2). The β-phase of BaB_2O_4 (BBO) is of major practical interest, since this is a highly promising nonlinear optical material with an extremely high radiation resistance. Thus, the optical and nonlinear-optical properties of BBO have been studied fairly intensively. However, other physical properties of BBO (such as the pyroelectric, piezoelectric, and luminescence properties) have been less well studied. Here we consider the pyroelectroluminescence effect observed in BBO single crystals.

Single crystals of BBO were grown by a modified Czochralski method from a flux onto a seed. The solvent was Na_2O. The composition of the flux used to grow BBO was 78 mol % BaB_2O_4 and 22 mol % Na_2O. Samples in the form of $1.5 \times 4 \times 6$ mm wafers were cut from high-quality sections of the as-grown single crystals.

The measurements were made in a cryostat at a residual air pressure of 1–10 Pa in the temperature range 80–400 K. The pyroelectroluminescence was recorded using an FÉU-39 photomultiplier. The rate of change in temperature during cooling varied in the range 0.08–0.25 K/s (in some cases liquid nitrogen was poured directly into the cryostat) and during heating did not exceed 0.15 K/s.

Figure 1 gives the temperature dependence of the integrated emission of the BBO crystal during cooling (curve *1*) and heating (curve *2*). It can be seen clearly that the luminescence of the BBO crystal, in the form of isolated flashes, is recorded over the entire range of temperatures (80–400 K). The amplitude and repetition frequency of the light flashes vary depending on the rate of change in temperature and the ambient gas pressure, and decrease slightly at high temperatures. When the temperature stabilizes after a change, the light flashes cease. These characteristics of the BBO luminescence with varying temperature indicate that the observed luminescence has a pyroelectric character—pyroelectroluminescence. When conducting contacts were deposited on the sample and the pyrocurrent recorded at the same time as the luminescence intensity, it was observed that

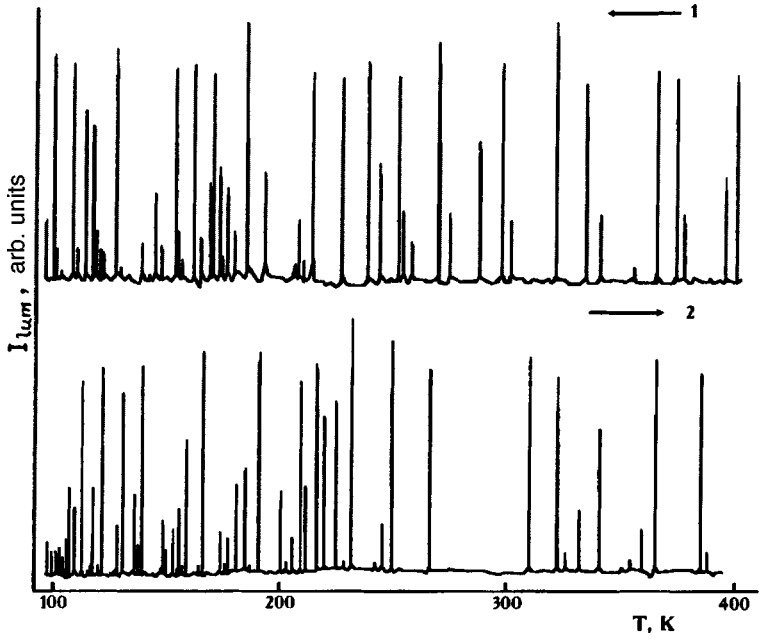

FIG. 1. Temperature curves of I_{lum} for a β-BaB_2O_4 crystal during cooling (curve *1*) and heating (curve *2*). The direction of change in temperature is indicated by the arrows.

the light flashes clearly coincided with the pyrocurrent oscillations.

It is known that the pyroelectroluminescence accompanying a change in the temperature of a pyroactive crystal is associated with electric fields which appear in the crystal as a result of the pyroelectric effect, and has already been observed in many crystals exhibiting the pyroelectric effect, such as $LiNbO_3$, tourmaline,[4] proustite and pyrargyrite,[5] lithium metagermanate,[6] BeO (Ref. 7), $Li_2B_4O_7$ (Ref. 8), and LiB_3O_5 (Ref. 9). The mechanism responsible for this pyroelectroluminescence is assumed to differ for different crystals, ranging from a pure electric gas discharge at the surface of the crystal to the combination of surface breakdown, internal breakdown, and the self-radiation of the crystal, associated for example with photo- or electroluminescence.

The results of Refs. 10 and 11 indicate that BBO single crystals have a fairly high pyrocoefficient (between 14.5 and 15.0×10^{-6} C/m$^2\cdot$K) at room temperature, and this remains almost constant in the range 100–300 K. Simple calculations show that for these values of the pyrocoefficient, a change in the temperature of the BBO crystal by a few degrees (the specific values of ΔT depend on the rate of change in temperature dT/dt) is sufficient to produce electric fields E up to 10^7 V/m as a result of the buildup of pyrocharge. These fields are sufficient to break down air, even at normal atmospheric pressure (10^5 Pa) and especially at the reduced pressures of 1–10 Pa in our case. A separate experiment in which the samples were heated above room temperature at 10^5 Pa, showed that pyroelectroluminescence flashes are still observed, but less frequently and at a lower intensity than those at reduced pressure. Attention is drawn to the complete analogy between the curves $I_{lum}(T)$ for the cooling (Fig. 1, curve *1*) and heating processes (curve *2*), and the absence of background luminescence, unlike lithium borates.[8,9] This behavior may indicate that no structural transformations take place in BBO in the temperature range 80–400 K (pyroelectroluminescence is sensitive to characteristics of the temperature behavior of the physical properties of the crystal and to the existence of phase transitions[9]).

A similar experiment to study pyroelectroluminescence was carried out using the α-phase of BaB_2O_4. However, as was to be expected, no traces of pyroelectroluminescence were identified in α-BaB_2O_4 since α-BaB_2O_4 belongs to the centrosymmetric class of crystals which do not exhibit the pyroelectric effect.

In our opinion, one important conclusion can be drawn from these results. The observation of pyroelectroluminescence at temperatures of 300–400 K indicates that strong electric fields and discharges are formed inside and at the surface of the crystals as the temperature varies in the range of operating temperatures of nonlinear-optical BBO elements. This may be an additional reason for the more frequent (compared with LiB_3O_5) cracking of BBO nonlinear optical elements operating at high laser powers.

[1] D. Eimerl, L. Devis, S. Velsko, E. K. Graham, and A. Zalkin, J. Appl. Phys. **62**, 1968 (1987).
[2] D. N. Nikogosyan, Élektron. Tekh. Ser. Laser. Tekh. Optoélektron. No. 2(54) (1990).
[3] K. A. Mirza, P. D. Townsend, and G. L. Destefanis, Phys. Status Solidi A **47**, K63 (1978).
[4] K. S. V. Nambi, Phys. Status Solidi A **82**, K71 (1984).
[5] S. L. Bravina, L. K. Kadashchuk, N. V. Morozovskiĭ *et al.*, Zh. Tekh. Fiz. **58**, 1404 (1988) [Sov. Phys. Tech. Phys. **33**, 834 (1988)].
[6] S. L. Bravina, L. K. Kadashchuk, N. V. Morozovskiĭ *et al.*, Zh. Tekh. Fiz. **60**(1), 91 (1990) [Sov. Phys. Tech. Phys. **35**, 54 (1990)].
[7] V. V. Shul'gin, A. V. Kruzhalov, I. N. Ogorodnikov *et al.*, Zh. Prikl. Spektrosk. **48**, 286 (1988).
[8] O. T. Antonyak, Ya. V. Burak, I. T. Lyseĭko *et al.*, Opt. Spectrosk. **61**, 550 (1986) [Opt. Spectrosc. (USSR) **61**, 345 (1986)].
[9] Ya. V. Burak, Ukr. Fiz. Zh. **42**, 466 (1997).
[10] Yu. V. Shaldin, R. Popravski, S. Matyyasik *et al.*, Fiz. Tverd. Tela (St. Petersburg) **37**, 1160 (1995) [Phys. Solid State **37**, 630 (1995)].
[11] R. Guo and A. S. Bhalla, J. Appl. Phys. **66**, 6186 (1989).

Translated by R. M. Durham

Extended region of ''anomalous'' acceleration in the cathode jet of a vacuum discharge

S. P. Gorbunov, V. I. Krasov, and V. L. Papernyĭ

Irkutsk State University
(Submitted July 25, 1996; resubmitted July 4, 1997)
Pis'ma Zh. Tekh. Fiz. **24**, 66–70 (February 26, 1998)

It is observed that ''anomalous'' acceleration of ions in a pulsed vacuum discharge is initiated at a certain distance from the surface of the cathode and takes place in the bulk of the cathode jet. It is established that the average ion energy $\overline{\varepsilon_i}$ increases as the length l of the discharge gap increases. © *1998 American Institute of Physics.* [S1063-7850(98)03002-X]

1. The existing model of ion acceleration in various types of vacuum discharges assumes a hydrodynamic mechanism for the entrainment of particles by an electron gas expanding into vacuum.[1] In this case, the ions acquire most of their energy ($\overline{\varepsilon_i} \leqslant 150$ eV) in the collisional part of the flow at a distance of $\leqslant 10^{-2}$ mm from the surface of the cathode[2] and as a result, the ion energy is almost independent of the length of the discharge gap, as has been confirmed by measurements.[3]

In addition, ion fluxes (generated at instants of current ''surges'') with energies up to tens of mega-electronvolts have been observed in high-voltage vacuum discharges[4–6] and these cannot be explained using the existing model. It may be postulated that this ''anomalous'' ion acceleration takes place in the bulk of the cathode jet (see Ref. 7, for example) although this has not been confirmed experimentally.

Characteristics of the ion acceleration mechanism in a low-inductance vacuum spark were investigated in Refs. 8 and 9. An analysis of the results suggested a single acceleration mechanism over a wide range of accelerated ion energies, $\sim 10^2 - 10^7$ eV.

Here we investigate the region of ion acceleration in the cathode jet of a pulsed vacuum discharge under conditions where this anomalous acceleration mechanism is achieved.

2. The experiments were carried out using apparatus similar to that described in Ref. 8. A vacuum spark was formed by discharging a capacitative storage device across an electrode system consisting of a needle-shaped copper cathode 1 mm in diameter and an anode 30 mm in diameter. The anode was a planar stainless steel grid with a mesh size of ≈ 1 mm which could be moved inside the vacuum chamber along the axis of the cathode so that the distance between the electrodes could be varied between 2 and 15 mm. The discharge was initiated by high-voltage breakdown of the keep-alive electrode on the cathode over the surface of a dielectric insert. The residual pressure in the chamber was $< 5 \times 10^{-5}$ Torr. The discharge current was measured with a Rogowski loop. The character of the discharge and its parameters were controlled by the initial voltage U across the capacitative storage system, which could be varied in the range 40–1000 V.

The energy and mass composition of the ions in the plasma jet was analyzed by a time-of-flight method using a single-channel electrostatic analyzer of the ''plane-parallel capacitor'' type, mounted behind the anode on the axis of the discharge. The average energy of the Cu^+ copper ions was determined from the particle energy spectrum measured over a series of ''shots'' at constant U by a method described in detail in Ref. 9.

3. In our previous experiments[8,9] it was shown that the average energy of the accelerated ions in the cathode jet depends on the maximum rate of rise of the discharge current $\dot{I}$. The value of $\dot{I}$ was varied by varying the initial voltage across the storage device U for a fixed discharge-gap length l. In the present study, the average energy of the accelerated particles was also determined for different l to investigate the region of ion acceleration.

Figure 1 gives the curves $\dot{I}(U)$ for various distances between the cathode and the anode. Each experimental point was obtained over twenty shots and the mean-square deviation of $\dot{I}$ did not exceed 7%. It can be seen from Fig. 1 that

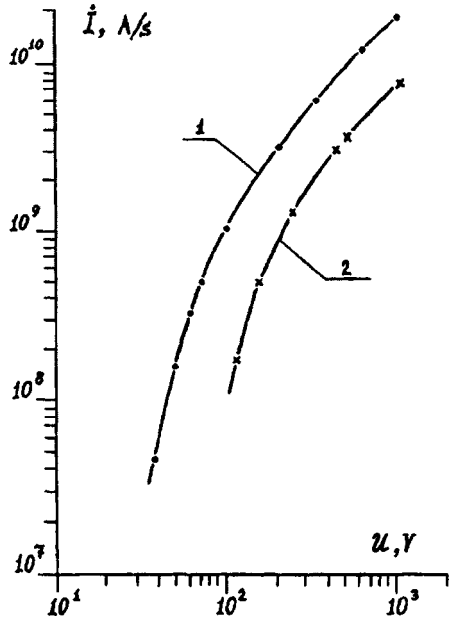

FIG. 1. Maximum rate of current rise $\dot{I}$ in discharge versus voltage U across storage device for various interelectrode gaps l: *1*—$l = 3$ mm, *2*—$l = 15$ mm.

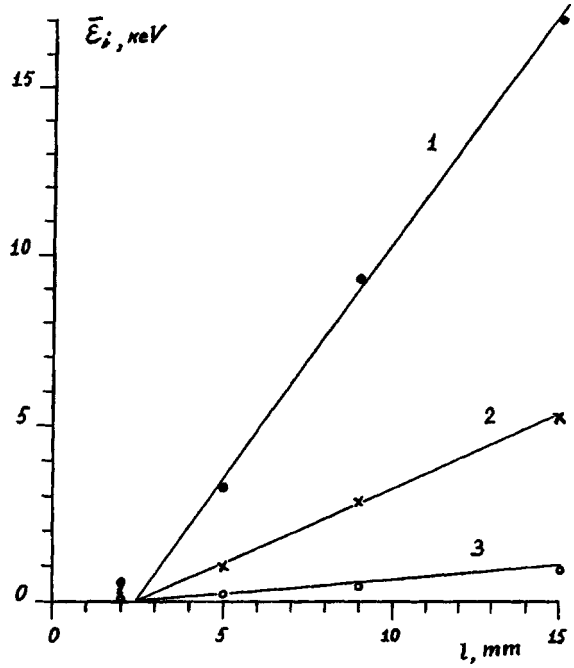

FIG. 2. Average energy of accelerated ions $\bar{\varepsilon}_i$ versus length of interelectrode gap l for various maximum rates of current rise $\dot{I}$ in the discharge.

the value of $\dot{I}$ is uniquely determined by U for fixed l but when the length of the interelectrode gap decreases, the same value of $\dot{I}$ is achieved for lower U.

As a result of measuring the average energy of the accelerated ions, it was observed that for fixed $\dot{I}$ the average energy $\bar{\varepsilon}_i$ depends on the length of the interelectrode gap l. Figure 2 gives curves of $\bar{\varepsilon}_i(l)$ for $\dot{I}=6\times10^9$ A/s (*1*), $\dot{I}=3\times10^9$ A/s (*2*), and $\dot{I}=10^9$ A/s (*3*). Note that the initial voltage across the storage device is the parameter which can be directly regulated experimentally for $l=$const. The required value of $\dot{I}$ was set by suitably selecting U (Fig. 1) and was monitored using the signal from the Rogowski loop. The value of $\dot{I}$ thus obtained was sustained over the ~100 shots required to measure the energy spectrum and the average energy of the accelerated ions $\bar{\varepsilon}_i$. It can be seen from Fig. 2 that for fixed $\dot{I}$, $\bar{\varepsilon}_i$ increases almost proportionately with l and this dependence is initiated at a certain minimum distance from the surface of the cathode $l^*\approx2-3$ mm. The coefficient of proportionality $d\bar{\varepsilon}_i/dx$ increases with $\dot{I}$ up to $d\bar{\varepsilon}_i/dx\approx1370$ eV/mm for $\dot{I}=6\times10^9$ A/s.

4. The experimentally determined dependence of the accelerated ion energy on the length of the interelectrode gap implies that the anomalous acceleration mechanism is only initiated when the plasma jet is some distance from the cathode (i.e., for $l>l^*$) and the particles undergo acceleration over their entire subsequent path to the anode. It is interesting to note that in the previously cited studies[4–6] where anomalous ion acceleration was observed, the distance between the cathode and the anode was fairly large (6–20 mm).

The efficiency of the mechanism can be characterized by the ''force'' $d\bar{\varepsilon}_i/dx$ whose value for this range of parameters remains almost constant over the length of the discharge gap and depends only on the rate of rise of the discharge current $\dot{I}$.

This ion acceleration in the bulk of the cathode jet may be caused by magnetohydrostatic forces associated with the flowing current and leading to compression of the jet by the self-induced magnetic field (see Ref. 10, for example). To examine this possibility, we consider Ref. 11 where this effect was observed for a pulsed vacuum discharge with parameters similar to those for which the present results were obtained. During compression of the plasma jet a cylindrical current channel of diameter $d\approx2-3$ mm was formed at a distance from the cathode close to d. This implies that in this region the magnetic forces begin to have a strong influence on the motion of the plasma jet. Bearing in mind that the anomalous ion acceleration begins at the same distance from the cathode, it may be postulated that the ion acceleration is associated with the action of magnetic forces.

This work was supported by the Russian Fund for Fundamental Research (Grant No. 95-02-04026a).

[1] I. A. Krinberg, M. P. Lukovnikova, and V. L. Papernyĭ, Zh. Éksp. Teor. Fiz. **97**, 806 (1990) [Sov. Phys. JETP **70**, 451 (1990)].
[2] I. A. Krinberg, Pis'ma Zh. Tekh. Fiz. **20**, 81 (1994) [Tech. Phys. Lett. **20**, 759 (1994)].
[3] G. A. Mesyats and D. I. Proskurovskiĭ, *Pulsed Electric Discharge in Vacuum* [in Russian], Nauka, Novosibirsk, (1984).
[4] E. D. Korop and A. A. Plyutto, Zh. Tekh. Fiz. **41**, 1055 (1971) [Sov. Phys. JETP **16**, 830 (1971)].
[5] E. D. Korop and A. A. Plyutto, Zh. Tekh. Fiz. **40**, 2534 (1970) [Sov. Phys. JETP **15**, 1986 (1970)].
[6] L. P. Bradly and G. W. Kuswa, Phys. Rev. Lett. **29**, 1441 (1972).
[7] M. V. Nezlin, *Beam Dynamics in Plasma* [in Russian], Énergoatomizdat, Moscow (1981).
[8] N. V. Astrakhantsev, A. V. Vanteev *et al.*, Pis'ma Zh. Tekh. Fiz. **21**(11), 37 (1995) [Tech. Phys. Lett. **21**, 412 (1995)].
[9] N. V. Astrakhantsev, V. I. Krasov, and V. L. Paperny, J. Phys. D: Appl. Phys. **28**, 2514 (1995).
[10] A. E. Blaugrund and G. Cooperstein, Phys. Rev. Lett. **34**, 461 (1975).
[11] D. F. Alferov, N. I. Korobova, and I. O. Sibiryak, Fiz. Plazmy **19**, 399 (1993) [Plasma Phys. Rep. **19**, 207 (1993)].

Translated by R. M. Durham

A possible method of computer-aided design of materials with a highly porous matrix structure based on the method of moving cellular automata

S. G. Psakh'e, D. D. Moiseenko, A. I. Dmitriev, E. V. Shil'ko, S. Yu. Korostelev, A. Yu. Smolin, E. E. Deryugin, and S. N. Kul'kov

Institute of Physics of Strength of Materials and Materials Science, Siberian Branch of the Russian Academy of Sciences, Tomsk

(Submitted July 3, 1997)
Pis'ma Zh. Tekh. Fiz. **24**, 71–76 (February 26, 1998)

The method of moving cellular automata was used to model a sample of ZrO_2 ceramic with a matrix structure under conditions of uniaxial compression. Studies were made of the strength and type of damage to the initial structure and its modifications. Particular attention was devoted to studying the influence of characteristics of the matrix structure on the formation and suppression of internal stress macroconcentrators. It is shown that the method of moving cellular automata can be used for the computer-aided design of matrix materials with a complex structure by specifically influencing the formation and evolution of stress macroconcentrators. © *1998 American Institute of Physics.* [S1063-7850(98)03102-4]

Studies of the mechanical properties of materials with a matrix structure are of considerable interest not only for classical problems in biomechanics,[1,2] but also for other fields of mechanics, such as determination of the optimum weight/strength ratio (materials used in transport) or the optimum absorbed energy/movement ratio (sound insulators, vibration absorbers).

Experimental studies of the strength and other properties of matrix materials not only involve considerable effort and expenditure of materials, but frequently encounter fundamental difficulties because of the need to study the dynamics of the fracture process in local regions of the matrix. The impossibility of making a detailed investigation of the process leads to distortion, and even loss of information on the influence of the topological characteristics of the matrix structure on its operating performance.

This aspect is usually studied theoretically using mesh methods of the mechanics of continuous media, but discrete approaches are now beginning to be used.[3] In particular, one of the most advanced discrete methods is the method of moving cellular automata (MCA).[3–7]

In this method, the material being modeled is represented as an ensemble of elements interacting between themselves according to specific rules. As a result of the mobility of the various elements, this approach can model various processes taking place in a real heterogeneous material, including penetration effects, mass transfer, fragmentation effects, damage formation, crack propagation, and so on. By setting the conditions at the boundaries, it is possible to simulate different mechanical loading regimes (compression, tension, shear strain, and so on).

Here this method is used to solve problems involved in studying the response (as far as fracture) of matrix structures. A sample of ZrO_2 ceramic with a matrix structure was modeled under conditions of uniaxial compression.

To generate the matrix structure, we developed a special algorithm for constructing arbitrary matrix structures with predefined statistical topological characteristics. The sample modeled here was a highly porous ($\sim$46% porosity) structure (Fig. 1a) measuring 1.86×2.05 cm. The response function of the automaton for these problems is determined by the mechanical properties of the material being modeled.[3,4] One of these parameters is Young's modulus which in the present case (for the matrix elements) corresponded to Young's modulus for a sintered ceramic (the samples were sintered from nanocrystalline ZrO_2 powder), being 2×10^{12} dyn/cm^2. The loading of the sample was simulated by assigning constant rates of 10 cm/s to the elements of the upper layer (Fig. 1a).

The calculated loading diagram is shown in Fig. 2. It can be seen that the strength of this structure was 8×10^8 dyn/cm^2. Note that for a continuous sample of the same dimensions with the same parameters of the elements, the calculations yielded a strength of 1.4×10^{10} dyn/cm^2. These results show fairly good agreement with the experimental results: the strength of nonporous ceramic is $\sim 1.3\times 10^{10}$ dyn/cm^2 while that for 50% porosity is $\sim 6\times 10^8$ dyn/cm^2. Extrapolation shows that the quantitative difference between the calculated and experimental results does not exceed 15–20%.

In practice, the strength characteristics of matrix materials are usually enhanced by introducing a special filler in the open pores (i.e., those reaching the surface).

Using the advantages of the MCA method, we modeled the fracture of a sample with filler in the surface pores. The modeled filler was plastic with a Young's modulus of 5×10^{10} dyn/cm^2.

It can be seen from the calculated loading diagram (Fig. 2) that the strength of the sample increased to 11.5×10^8 dyn/cm^2 (almost 1.5 times). Typically, the theoretical strength of plastic with the parameters used in the calculations is 1.5 times lower than the strength of the ceramic, and the relative volume of the filler was 21.8% of the volume of the matrix material. This is consistent with current thinking

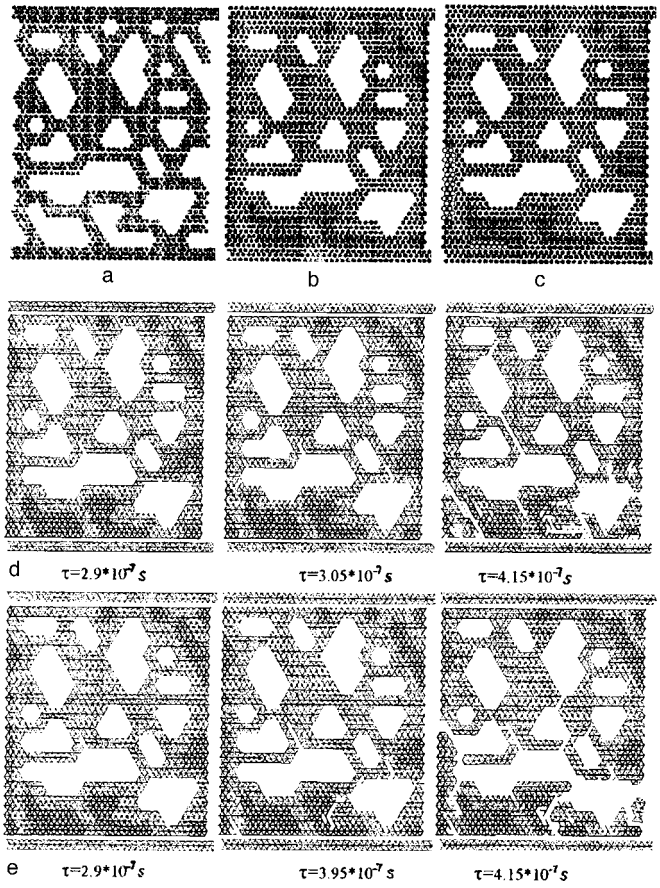

FIG. 1. a—Initial structure, b—matrix with filler in open pores, c—matrix with inclusions, d—fracture dynamics for sample with filler, and e—fracture dynamics for sample with filler and corundum plates.

on the influence of the surface layers on the strength characteristics of materials with a matrix structure.

The dynamics of the evolution of fracture for a sample with a surface filler is shown in Fig. 1d. It can be seen that the complex topology of the sample structure leads to the formation of stress macroconcentrators. This resulted in the formation of a main crack (Fig. 1d, $\tau = 4.15 \times 10^{-7}$) in the bottom left corner of the sample, and therefore, resulted in a loss of carrying capacity. It should be noted that the first damage appeared considerably earlier. It can be seen from Fig. 1d ($\tau = 3.05 \times 10^{-7}$) that this damage has a complex distribution over the sample, releasing and redistributing its elastic energy.

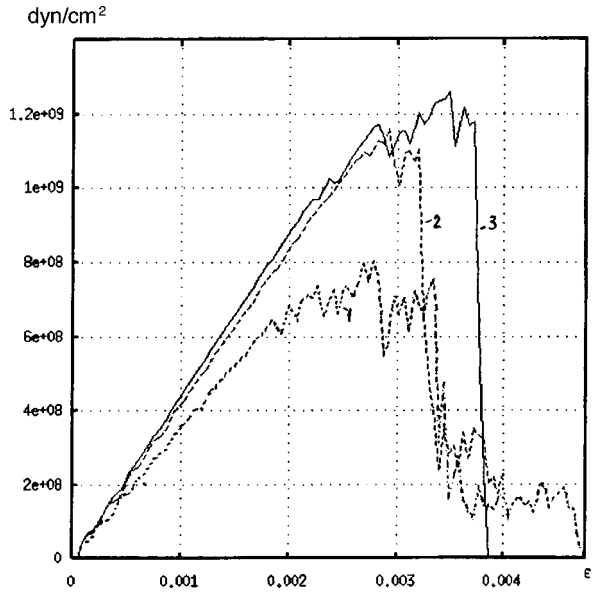

FIG. 2. Loading diagram (load—relative elongation): *1*—initial structure, *2*—structure with surface filler, and *3*—structure with strengthening inclusions.

One possible method of improving the compressive strength involves locally changing the properties of this matrix structure. This requires a knowledge of the evolution of the initial sample as far as fracture. Here we modeled the fracture of a sample with the matrix structure shown in Fig. 1c, where two ''strengthening'' corundum (Al_2O_3) inclusions were located at the sites where the main crack reaches the surface. The relative volume of the inclusions was less than 2%. The results of the calculations revealed completely different fracture dynamics for the modeled structure. In particular, it can be seen from Fig. 1e that the incorporation of inclusions had the following results:

1) it changed the stress redistribution pattern during loading;

2) it blocked the evolution of a macroconcentrator;

3) it changed the spatial pattern of the elastic energy release;

4) it changed the dynamics of the formation and evolution of the damage;

5) it suppressed the propagation of the main crack.

Ultimately, as can be seen from the loading diagram shown in Fig. 2, the strength of the sample increased to 13×10^8 dyn/cm^2. Note that total fracture of the sample occurred at 0.35% strain whereas for the empty matrix this value was 0.28%, and for the partially filled matrix 0.29%. It can be seen from the loading diagrams that despite the low percentage of inclusions, blocking of the concentrator produced an overall change in the effective Young's modulus of the sample.

To sum up, it has been shown that in addition to strengthening samples with a matrix structure by total or partial filling, another possible method of strengthening involves identifying and suppressing the formation and propagation of macroconcentrators. Thus, the method of moving cellular automata can be used to design components and structural elements made of materials having a highly porous matrix structure by suitably selecting the filler material, and specifically influencing the formation of macroconcentrators. Note that the formation of stress macroconcentrators in samples with a complex internal structure is a fairly complex one and requires a detailed analysis in each specific case.

[1] P. J. Rubin, R. L. Rakotomanana, P. F. Leyvraz, P. K. Zysset, A. Curnier, and J. H. Heegaard, J. Biomech. **26**, 725 (1993).
[2] J. H. Heegaard and A. Curnier, Int. J. Numer. Methods Eng. **36**, 569 (1993).
[3] S. G. Psakh'e, Ya. Khori, S. Yu. Korostelev, A. Yu. Smolin, A. I. Dmitriev, E. V. Shil'ko, and S. V. Alekseev, Izv. Vyssh. Uchebn. Zaved. Fiz. No. 11, 58 (1995).
[4] S. G. Psakh'e, A. Yu. Smolin, S. Yu. Korostelev, A. I. Dmitriev, E. V.

Shil'ko, and S. V. Alekseev, Pis'ma Zh. Tekh. Fiz. **21**(20), 72 (1995) [Tech. Phys. Lett. **21**, 849 (1995)].
[5] S. G. Psakh'e, E. V. Shil'ko, A. I. Dmitriev, S. Yu. Korostelev, and A. Yu. Smolin, Pis'ma Zh. Tekh. Fiz. **22**(2), 90 (1996) [Tech. Phys. Lett. **22**, 88 (1996)].
[6] S. G. Psakh'e, E. V. Shil'ko, A. I. Dmitriev, S. Yu. Korostelev, A. Yu. Smolin, and E. N. Korosteleva, Pis'ma Zh. Tekh. Fiz. **22**(12), 69 (1996) [Tech. Phys. Lett. **22**, 511 (1996)].
[7] S. G. Psakhie, A. Yu. Smolin, E. V. Shilko, S. Yu. Korostelev, A. I. Dmitriev, and S. V. Alekseev, J. Mater. Sci. Technol. **13**, 69 (1997).

Translated by R. M. Durham

Efficiency of the generation of characteristic radiation by stopping low-energy electron beams

V. I. Bespalov, V. V. Ryzhov, and I. Yu. Turchanovskiĭ

Tomsk Polytechnic University; Institute of High-Current Electronics, Siberian Branch of the Russian Academy of Sciences, Tomsk

(Submitted August 4, 1997)
Pis'ma Zh. Tekh. Fiz. **24**, 77–79 (February 26, 1998)

The Monte Carlo method is used to calculate the generation of characteristic radiation by stopping low-energy electrons in converters made of low-Z materials and it is shown that this method of generating characteristic radiation can compete with Z-pinches in terms of conversion efficiency. © *1998 American Institute of Physics.* [S1063-7850(98)03202-9]

When low-energy electrons are stopped in a material, a significant fraction of the beam energy may be emitted as characteristic radiation, which is produced as a result of photoabsorption of bremsstrahlung and as a result of electron-impact ionization of inner atom shells. Since the cross section for the second process increases with decreasing atomic number Z, highly efficient generation of characteristic radiation may be achieved by stopping electrons in converters made of low-Z materials.

We used a program which simulates the evolution of an electron-photon cascade in a converter by the Monte Carlo method, in order to investigate the optimum conditions for the generation of characteristic radiation and to select efficient converters. To calculate the spectral distribution of the radiation beyond the converter, we developed a version of the program[1] which takes into account the generation of characteristic radiation as a result of ionization of the K-shell by bremsstrahlung photons and by electrons. The cross section for electron impact K-ionization was taken from Ref. 2.

Figure 1 gives the calculated yield of characteristic radiation (curve *3*), bremsstrahlung (curve *2*), and the total x-ray radiation yield (curve *1*) when electrons with various initial energies E_0 are stopped in a planar layer of argon. The layer thickness d was selected to give the maximum yield of characteristic radiation from the converter for a given energy E_0. It can be seen from Fig. 1 that when low-energy electrons ($E_0<100$ keV) are stopped, a considerable fraction of the energy is emitted as characteristic radiation. The bremsstrahlung energy ΔE_{Br} emitted in the continuum only becomes equal to the characteristic radiation energy ΔE_K emitted on the lines for $E_0>120$ keV.

An analysis of the calculated results indicated that the electron energy E' for which $\Delta E_K=\Delta E_{Br}$ depends linearly on the atomic number Z of the material:

$$E'=236-5.6\times Z(\mathrm{keV}).$$

It follows from this formula that for converters with $Z>42$ the bremsstrahlung yield is always higher than the characteristic radiation yield.

Figure 2 gives the results of calculating the maximum efficiency of characteristic radiation generation relative to the energy of the beam electrons $\eta_K=\Delta E_K/E_0$ for convert-

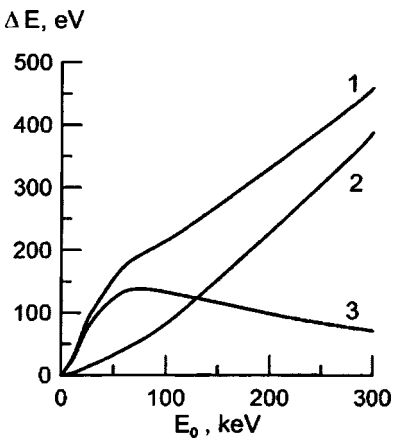

FIG. 1. Total yield of x-ray radiation energy (curve *1*) and its components: bremsstrahlung (curve *2*) and characteristic radiation (curve *3*) from argon as a function of initial electron energy. (The results of the calculations are normalized to a single incident electron.)

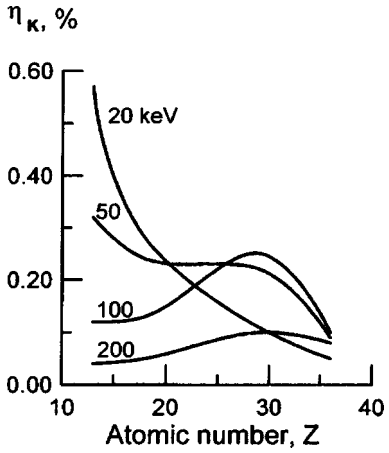

FIG. 2. Efficiency of the generation of characteristic radiation versus atomic number of converter material for various initial electron energies E_0, keV (the energies are given on the curves). (The results are normalized to a single incident electron.)

ers with $13 \leqslant Z \leqslant 36$ (between Al and Kr). It can be seen thatthe highest efficiency is achieved for the stopping of low-energy electrons in Al ($\eta_K = 0.57$ for $E_0 = 20$ keV). In this case, the spectrum contains very little bremsstrahlung.

To conclude, when low-energy electron beams with $E_0 < E'$ are stopped, most of the energy is emitted in the form of characteristic radiation (line spectrum), so that this method of generating characteristic radiation can be considered to be an efficient method of obtaining x-ray line radiation in the kilo-electronvolt energy range.

[1] S. D. Korovin, V. V. Ryzhov, I. Yu. Turchanovsky, and V. I. Bespalov, in *Proceedings of the Tenth IEEE International Pulsed Power Conference*, Albuquerque, NM, (1995), Vol. 1, pp. 75–79.
[2] H. Kolbenstvedt, J. Appl. Phys. **38**, 4785 (1967)

Translated by R. M. Durham

Influence of working gas pressure on the properties of thin films of high-temperature superconductors obtained by magnetron sputtering

A. K. Vorob'ev, S. V. Gaponov, S. A. Gusev, Yu. N. Drozdov, E. B. Klyuenkov, and V. I. Luchin

Institute of Microstructure Physics, Russian Academy of Sciences, Nizhniĭ Novgorod
(Submitted August 18, 1997)
Pis'ma Zh. Tekh. Fiz. **24**, 80–85 (February 26, 1998)

The surface morphology, composition, microstructure, and electrical properties of thin films of $YBa_2Cu_3O_{7-x}$ high-temperature superconductors, obtained by inverted magnetron sputtering, have been studied as a function of the pressure of the working gas mixture and results are presented. The main parameters of the magnetron discharge plasma near the substrate were determined by analyzing the characteristics of Langmuir probes. Changes in the properties of the films are considered to be caused by bombardment of the growing film with plasma ions accelerated in the floating potential field of the substrate. Films obtained at a pressure of 28 Pa and substrate temperature of 630 °C had a superconducting transition end temperature $T_{c,\mathrm{off}}=89$ K and a critical current density $j_c=2$ MA/cm^2 (at 77 K) and were free from secondary phase particles larger than 10 nm. [S1063-7850(98)03302-3]

The problem of obtaining single-phase films must be solved to achieve further improvements in devices based on thin films of high-temperature superconductors. As a result of deviations from stoichiometry during the single-stage (*in situ*) growth of $YBa_2Cu_3O_{7-x}$ (YBCO) high-temperature superconducting films, a heterogeneous system is usually formed, consisting of the 1–2–3 phase and phases enriched in various components. These secondary-phase particles may have a high surface density and sizes far in excess of the characteristic dimensions of the devices fabricated using YBCO films.[1,2] An understanding of the importance of this problem has stimulated an intensive search for technologies to produce YBCO films with a highly homogeneous phase composition and smooth surfaces.[3–6]

It is known that the properties of a YBCO condensate are determined to a considerable extent by the method and conditions of deposition. In particular, when magnetron sputtering is used, the working gas pressure may have a substantial influence on the properties.[7]

Here we investigate the surface morphology, composition, microstructure, and electrical properties of thin films of $YBa_2Cu_3O_{7-x}$ high-temperature superconductors prepared by inverted magnetron sputtering, as a function of the pressure of the working gas mixture (Ar/O_2 in the ratio 1:1). The design and operating characteristics of the magnetron sputtering system were described in detail in Ref. 8. We investigated the properties of YBCO films on finite substrates. The critical parameters of the YBCO films were determined by methods described in Ref. 9. The quality of the crystal structure was monitored by x-ray diffraction measurements using a DRON-4 diffractometer. The surface morphology of the YBCO films and their chemical composition were studied using a JEM-2000 EX II electron microscope fitted with an energy-dispersive spectrometer.

Figure 1a gives the superconducting transition end temperature $T_{c,\mathrm{off}}$ and the critical current density j_c (at 77 K) for YBCO films obtained at a substrate temperature $T_d=660$ °C, as a function of the working gas pressure p. Figure 2 shows secondary-electron images of the surface of the films obtained at various pressures p. It can be seen from Figs. 1 and 2 that the films with the highest transport properties contain secondary-phase particles. The chemical composition, possible causes, and characteristics of the formation of these particles were described by us in detail in Refs. 9 and 10. The particles visible in Fig. 2 consist mainly of copper. It can be seen from Fig. 2 that as the pressure p decreases, the smoothness of the film surface improves. The films formed at pressures of 28 Pa are free from visible secondary-phase particles larger than 10 nm. Figure 1b gives the intensity ratio $I_{\mathrm{Cu}}/I_{\mathrm{Ba}}$ of the characteristic x-ray radiation lines of the copper and barium atoms, which show the change in the concentration of these components in the YBCO films, plotted as a function of the pressure p. As p decreases, the relative copper content in the film decreases. For the smooth films we find $I_{\mathrm{Cu}}/I_{\mathrm{Ba}}=0.54$ and for our standard YBCO single crystal we find $I_{\mathrm{Cu}}/I_{\mathrm{Ba}}=0.46$. The x-ray diffraction data show that the microstructure of the films remains approximately constant in this pressure range. The lattice parameter is $c=1.167-1.169$ nm and the full width at half maximum of the rocking curve is FWHM(005)YBCO $=0.4-0.6°$ for all films. By optimizing the substrate temperature ($T_d=630$ °C) at a pressure of 28 Pa, we obtained YBCO films having the parameters $T_{c,\mathrm{off}}=89$ K, $j_c=2$ MA/cm^2 (at $T=77$ K), free from secondary-phase particles larger than 10 nm.

In Refs. 7, 11, and 12, the observed changes in the surface morphology, composition, and properties of YBCO films are attributed to bombardment of the growing film by negative oxygen ions, accelerated in the field of the target.

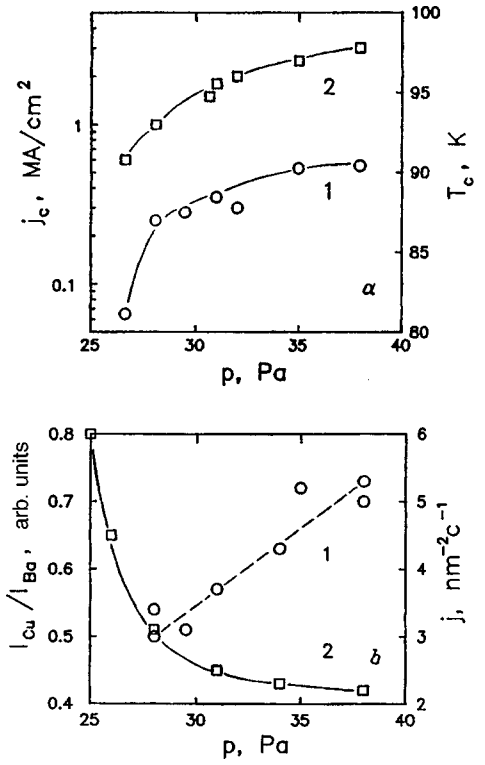

FIG. 1. a—Superconducting transition end temperature $T_{c,\mathrm{off}}$ (*1*) and critical current density j_c (at 77 K) (*2*); b—intensity ratio $I_{\mathrm{Cu}}/I_{\mathrm{Ba}}$ of the characteristic x-ray radiation of copper and barium atoms (*1*) and density of ion flux to substrate positioned 50 mm from the target; (*2*), plotted as a function of the gas pressure p.

However, calculations of the ion mean free path before thermalization under our conditions give a value of the order of 1 mm, which is much less than the distance between the target and the substrate (50 mm). We attribute the influence of pressure on the properties of the YBCO condensate to bombardment of the growing film by plasma ions accelerated in the floating potential field of the substrate.[13,14]

In order to confirm this hypothesis, we determined the main parameters of the magnetron discharge plasma near the substrate by analyzing the characteristics of Langmuir probes (normal and double cylindrical probes 0.1 mm in diameter and 14 mm long and a 10×10 mm planar probe). It was established that the concentration of charged particles in the plasma varies between 7.6×10^{10} cm^{-3} and 2.2×10^{10} cm^{-3} in the pressure range 25–47 Pa. The electron temperature and the floating potential of the substrate do not depend on pressure and are 0.22 eV and -1.8 V relative to the plasma potential (the floating potential of the substrate was determined from the characteristic of a planar probe whose position and size corresponded to those of the substrate). It should be noted that the electron temperature and floating potential were determined more accurately compared with the preliminary data given in Ref. 13. Figure 1a gives the density of the ion flux to the substrate at the floating potential, obtained from the ion current to the planar probe, plotted as a function of pressure. Ions accelerated in the floating potential field of the substrate and bombarding the surface of condensation at energies up to 1.8 eV clearly exist. This energy exceeds the 1.3 eV activation energy for the desorption of YBCO components.[15,16] As a result, selective desorption of adatoms may take place, leading to changes in the composition of the condensate (Fig. 1b).

To conclude, these result show that during in situ growth in an inverted magnetron sputtering system the properties of YBCO films may be strongly influenced by bombardment of the condensation surface by plasma ions accelerated in the floating potential field of the substrate.

This work was carried out under the KGNT Program ''Topical Trends in the Physics of Condensed Media'' (''Su-

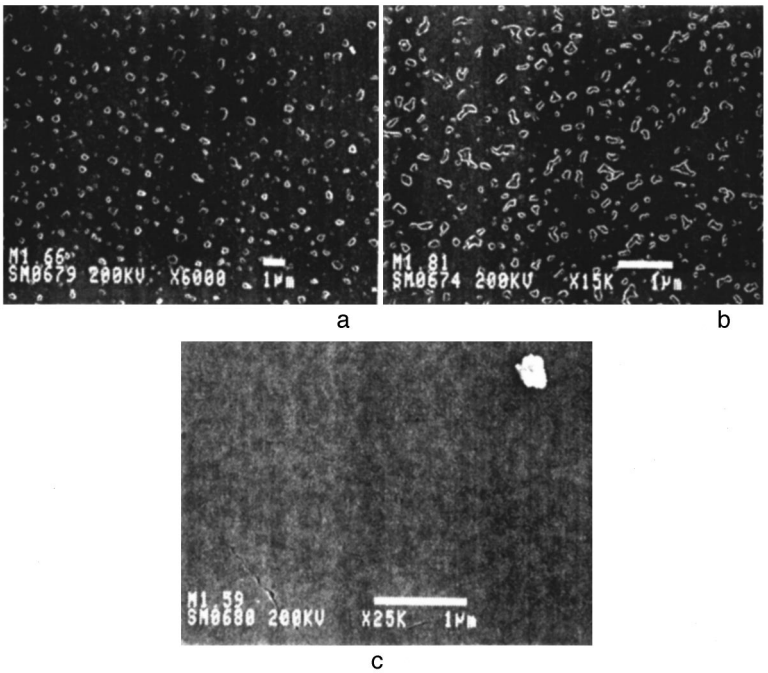

FIG. 2. Secondary-electron image of the surface of YBCO films obtained at various gas pressures p: a—38 Pa, b—30 Pa, and c—28 Pa.

perconductivity'' Research, Project 95043) and was supported by the Russian Fund for Fundamental Research (Grant No. 96-02-16993) and INTAS (Project 94-3912).

[1] E. Waffenschmidt, K. H. Waffenschmidt, F. Arndt *et al.*, J. Appl. Phys. **75**, 4092 (1994).
[2] J. Hudner, O. Thomas, E. Mossang *et al.*, J. Appl. Phys. **74**, 4631 (1993).
[3] W. Rauch, H. Behner, G. Gieres *et al.*, Physica C **198**, 389 (1992).
[4] A. Kuhle, J. L. Skov, S. Hjorth *et al.*, Appl. Phys. Lett. **64**, 3178 (1994).
[5] J. Auge, M. Jansen, H. G. Roskos *et al.*, Appl. Phys. Lett. **64**, 3166 (1994).
[6] C. N. L. Johnson, U. Helmersson, L. D. Madsen *et al.*, J. Appl. Phys. **77**, 6388 (1995).
[7] K. Sakuta, M. Iyori, Y. Katayama *et al.*, Jpn. J. Appl. Phys. **29**, L611 (1990).
[8] A. K. Vorob'ev, E. B. Klyuenkov, V. V. Talanov *et al.*, Pis'ma Zh. Tekh. Fiz. **19**(17), 12 (1993) [Tech. Phys. Lett. **19**, 537 (1993)].
[9] R. K. Belov, B. A. Volodin, A. K. Vorob'ev *et al.*, Fiz. Tverd. Tela (St. Petersburg) **37**, 785 (1995) [Phys. Solid State **37**, 426 (1995)].
[10] Yu. N. Drozdov, S. V. Gaponov, S. A. Gusev *et al.*, Supercond. Sci. Technol. **9**, 166 (1996).
[11] X. X. Xi, T. Venkatesan, Q. Li *et al.*, IEEE Trans. Magn. **27**, 982 (1991).
[12] J. Geerk, X. X. Xi, H. C. Li *et al.*, Philos. Mag. B **3**, 923 (1989)
[13] Yu. N. Drozdov, S. V. Gaponov, S. A. Gusev *et al.*, IEEE Trans. Appl. Supercond. **7** (1997), in press.
[14] Yu. N. Drozdov, S. V. Gaponov, S. A. Gusev *et al.*, Book of extended abstracts of papers presented at ISEC'97, Berlin 1997, Vol. 2, p. 49.
[15] V. V. Mamutin, Pis'ma Zh. Tekh. Fiz. **20**(15), 13 (1992) [*sic*].
[16] I. K. Marmorcos and S. Das Sarma, Surf. Sci. Lett. **237**, L411 (1990).

Translated by R. M. Durham

Computer modeling of the migration properties of oxygen in $Ba_{1-x}K_xBiO_3$

N. V. Moseev

Institute of Metal Physics, Russian Academy of Sciences, Ekaterinburg
(Submitted April 24, 1997; resubmitted October 12, 1997)
Pis'ma Zh. Tekh. Fiz. **24**, 86–88 (February 26, 1998)

A molecular statics method is used to calculate the energy barriers for the migration of oxygen ions in $BaBiO_3$ and $Ba_{1-x}K_xBiO_3$ Vacancy and interstitial mechanisms of diffusion are considered. The lowest energy barrier was obtained for the vacancy mechanism. © *1998 American Institute of Physics.* [S1063-7850(98)03402-8]

The oxide $BaBiO_3$ started to attract interest following the discovery by the authors of Ref. 1 that this oxide becomes superconducting when doped with potassium. It was shown that potassium replaces barium, and $T_c \sim 30$ K was observed in the compound $Ba_{0.6}K_{0.4}BiO_{2.90}$ which has a cubic structure.[1]

In Ref. 2, computer modeling was used to investigate ionic and electronic defects in $Ba_{1-x}K_xBiO_3$. The authors calculated the defect formation energies, but they did not determine the migration properties of the defects. The present author is not aware of any experimental investigations of oxygen diffusion in this oxide. The aim of this study is to calculate the energy barriers for defect migration in the oxygen sublattice, to determine the most probable mechanisms for the diffusion of oxygen.

The calculations were made using the MOLSTAT computer program[3] which implements the molecular statics method for ionic crystals. This program incorporates a procedure which automatically searches for the saddle point as a defect migrates between equilibrium positions. The migration energy barrier E_M is given by:

$$E_M = E_S - E_D,$$

where E_S is the defect energy at the saddle point and E_D is the defect energy in the equilibrium position.

The ion–ion interaction potentials for pure $BaBiO_3$ were taken from Refs. 4 and 5. The K^{1+}–O^{2-} interaction potential was taken from Ref. 2. With these potentials, the crystal structure of the oxide $Ba_{0.7}K_{0.3}BiO_3$ determined experimentally in Ref. 6 was correctly reproduced: after relaxation of the model crystallite, the ion coordinates of a unit cell corresponded to those determined experimentally.

First, the migration energy barriers were calculated for undoped cubic $BaBiO_3$. Table I gives the migration energies of oxygen ions for different diffusion mechanisms. Migration path *A* implies hopping of an oxygen ion by a vacancy mechanism between nearest positions. Migration path *B* assumes hopping by a vacancy mechanism between second nearest neighbor positions, and migration path *C* implies an interstitial diffusion mechanism. An interstitial oxygen ion in position [0.0 0.0 0.5] hops to the nearest interstitial position [0.0 0.5 0.0]. All these migration paths are shown in Fig. 1. It can be seen from Table I that the energy barrier for migration path *A* has the lowest value. Thus, from the energy point of view, the vacancy mechanism of oxygen diffusion is the most probable in undoped $BaBiO_3$.

The influence of potassium doping on the migration properties of the oxygen ions was then investigated. A single barium ion was replaced by a potassium ion. The energy barriers for the migration of oxygen ions by atomic mechanisms similar to those described above were then calculated near this substitution. The results are presented in Table I. It can be seen that in this case, the vacancy diffusion mechanism *A*, having the lowest migration energy, is the most probable. In addition, on comparing the data for $BaBiO_3$ and $Ba_{1-x}K_xBiO_3$, we find that potassium doping reduces the migration energy barrier for the vacancy mechanism and increases this barrier for the interstitial mechanism.

To sum up, it has been shown that in $BaBiO_3$, the vacancy mechanism of oxygen diffusion is the most probable

TABLE I. Migration energies of oxygen ions in $BaBiO_3$ and $Ba_{1-x}K_xBiO_3$.

	Energy barrier E_M, eV	
Migration path	$BaBiO_3$	$Ba_{1-x}K_xBiO_3$
A	0.96	0.80
B	3.70	2.55
C	2.94	5.20

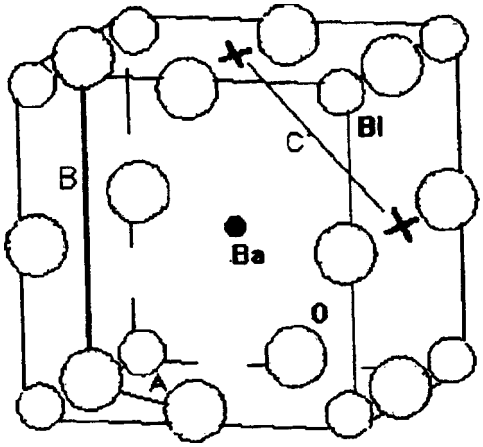

FIG. 1.

from the energy point of view. Potassium doping does not alter the type of energetically favored diffusion mechanism but lowers its energy barrier.

This work was partly financed by the Program for State Assistance to Leading Scientific Schools in the Russian Federation (Grant No. 96-15-96515).

[1] R. J. Cava, B. Batlogg, J. J. Kradjewski *et al.*, Nature (London) **332**, 814 (1988).
[2] X. Zhang and C. R. A. Catlow, Physica C **173**, 25 (1991).
[3] J. L. Gavartin, C. R. A. Catlow, A. L. Shluger *et al.*, Mod. Simul. Mater. Sci. Eng. **1**, 29 (1992).
[4] J. Prade, A. D. Kulkarni, F. W. de Wette *et al.*, Phys. Rev. B **39**, 2771 (1989).
[5] A. D. Kulkarni, J. Prade, F. W. de Wette *et al.*, Phys. Rev. B **40**, 2642 (1989).
[6] M. T. Weller, J. R. Grasmeder, P. S. Lanchester *et al.*, Physica C **156**, 265 (1988).

Translated by R. M. Durham

Multistable generation of monochromatic radiation in solid-state lasers

K. P. Komarov

Institute of Automation and Electrometry, Siberian Branch of the Russian Academy of Sciences, Novosibirsk
(Submitted May 5, 1997)
Pis'ma Zh. Tekh. Fiz. **24**, 89–92 (February 26, 1998)

It is shown that a solid-state laser with unpumped sections of action medium which act as a saturable absorber, may operate in a stable, single-mode cw lasing regime. The establishment of lasing in a particular mode under steady-state conditions depends on the initial conditions of transient evolution. © *1998 American Institute of Physics.* [S1063-7850(98)03502-2]

Studies of stable single-mode lasing regimes in solid-state lasers are attracting interest because of the new possibilities which are emerging for the development of reliable, practical, and convenient-to-use sources of high-power narrow-band radiation with controllable parameters. It was shown theoretically and experimentally in Refs. 1 and 2 that single-mode emission from a solid-state laser may be stabilized by inserting a slow-response saturable absorber and a negative feedback system in the laser cavity. The grating burned by the standing-wave field of the intracavity radiation in the losses of the saturable absorber plays the role of a nonlinear narrow-band selector which produces single-mode lasing, while the negative feedback system prevents the evolution of instability associated with the giant pulse emission caused by bleaching of the saturable absorber and thereby stabilizes the cw regime. Which particular mode is involved in the steady-state lasing depends on the initial conditions of the transient process. It is shown here that similar multistable lasing may be achieved without using negative feedback if unpumped sections of the active medium with negative population inversion are used as the saturable absorber.

An investigation is made of a model in which the active medium is close to one of the mirrors of a linear laser cavity. Population inversion is only established near the mirror. For emission of the ith mode, the population difference between the upper and lower lasing levels of the active medium is given by

$$N(x)=\frac{N^e(x)}{1+\eta I_i \sin^2(i\pi x/L)}, \tag{1}$$

where $N^e(x)$ is the population difference between the levels in the absence of the field. In the pumped region $0<x<l_g$ the inversion is positive $N^e(x)=N_g=\text{const}$. In the unpumped region $l_g<x<l$ the inversion is negative and the medium is absorbing $N^e(x)=-N_a=\text{const}$ (l is the length of the entire medium). The parameter η determines the reciprocal saturation intensity of the gain and the absorption, I_i is the intensity of the emitted mode, the function $\sin(i\pi x/L)$ describes the spatial distribution of the field of the ith mode, i is the number of antinodes in the standing wave of the corresponding (ith) mode, x is the longitudinal coordinate, and L is the optical length of the cavity.

The total gain for the kth mode $\mathscr{G}_k$ is determined by the difference between the gain in the region of positive inversion G_k and the losses in the region of negative inversion S_k. When a small-scale inhomogeneity in the inversion, described by expression (1),is created preferentially by generation of the ith mode, $\mathscr{G}_k$ is given by

$$\mathscr{G}_k=G_k-S_k=2\mathscr{D}\int_0^l N(x)[\sin^2(k\pi x/L)-\sin^2(i\pi x/L)]dx$$
$$=\frac{\eta I_i\mathscr{D}}{3}\left\{(N_g^e+N_a^e)l_g\left[1-\frac{\sin[2\pi(k-i)l_g/L]}{2\pi(k-i)l_g/L}\right]\right.$$
$$\left.-N_a^e l\left[1-\frac{\sin[2\pi(k-i)l/L]}{2\pi(k-i)l/L}\right]\right\}, \tag{2}$$

where $\mathscr{D}$ is the Einstein coefficient for the lasing transition. The saturation parameter ηI_i was assumed to be small $\eta I_i \ll 1$ to derive expression (2). The gain G_k is determined by the first term in braces (2) while the losses S_k are determined by the second term. Curves of G_k and S_k as a function of the mode number k are plotted in Fig. 1.

Modes whose frequency detuning from the lasing mode is up to a value of the order of the reciprocal length l_g^{-1} cm^{-1} of the positive inversion region ($N^e(x)>0$) have similar spatial field distributions in the pumped part of the active region and therefore the gain for these modes in this region is similar to that of the ith lasing mode (Fig. 1). However, for $l_g \ll l$ in a considerable part of the absorption region, the spatial configurations of the modes differ substantially and the losses for the nonlasing modes exceed those for the lasing mode by $\sim \eta I_i \mathscr{D} N_a^e l/3$. As a result, in the spectral range $\sim l_g^{-1}$ cm^{-1} modes with low radiation intensities (compared with the lasing mode) are suppressed near the frequency of the ith lasing mode (these modes make a negligible contribution to the formation of a spatial grid in the gain and the losses). If the spectral range in which the low-intensity modes are suppressed is broader than the spectral gain profile (or the spectral band of the additional intracavity linear selector which narrows the emitted radiation spectrum), the cw single-mode lasing is stable with respect to the excitation of other modes. Is this cw single-mode regime stable with respect to the buildup of relaxation oscillations of the lasing mode intensity? As we know, the answer to this question is affirmative for spatially uniform pumping.[3] It is

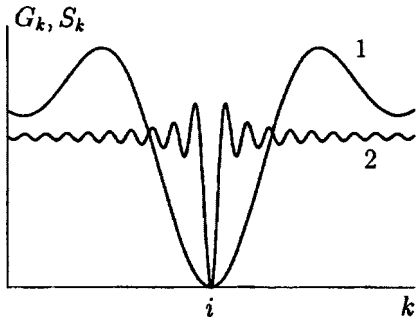

FIG. 1. Gain G_k (curve 1) and losses S_k (curve 2) versus mode number k with spatially nonuniform saturation of the pumped and unpumped sections of the active medium by the standing wave field of the ith mode ($l/l_g \approx 7$; $lN_a^e/l_g N_g^e \approx 0.7$).

easy to appreciate that for single-mode lasing the intensity distribution is determined by the function $I_i \sin^2(i\pi x/L)$ and the displacement of any fragment of the active medium inside the cavity along its axis by an amount which is a multiple of half the wavelength, does not alter the parameters of the interaction between this fragment and the field, i.e., the lasing dynamics is invariant with respect to this type of translation (it should be noted that this is not the case for two-mode lasing). By means of a series of these translations, this particular spatially nonuniform pumping problem can clearly be reduced to the uniform pumping problem whose solution is described in Ref. 3. Thus, this single-mode steady state is stable with respect to any type of small perturbations. The number of these stable single-mode steady states is determined by the cavity length L, the length of the active medium l, and its pumped region l_g, and also by the width of the active-medium gain profile (or the spectral band of the additional intracavity linear selective element).

The threshold conditions can be satisfied in this system with $l_g \ll l$ by using a four-level active medium in which the lower lasing level is not too high above the ground level so that it becomes significantly populated as a result of thermodynamic exchange, and thus the absorption in the unpumped part of the active medium is fairly high. This situation can also be achieved in a three-level system with a fairly low density of active centers in the unpumped region.

[1] K. P. Komarov, Kvant. Elektron. (Moscow) **21**, 1049 (1994).
[2] K. P. Komarov, A. S. Kuch'yanov, and V. D. Ugozhaev, Kvant. Elektron. (Moscow) **24**, 657 (1997).
[3] Ya. I. Khanin, *Laser Dynamics* [in Russian], Sovet-skoe Radio, Moscow (1975), p. 192.

Translated by R. M. Durham

Activation energy for the formation of oxygen vacancies in undoped nonstoichiometric indium oxide films

A. M. Orlov, B. M. Kostishko, and L. I. Gonchar

Ulyanovsk State University
(Submitted July 15, 1997)
Pis'ma Zh. Tekh. Fiz. **24**, 1–5 (February 12, 1998)

An analysis is made of the temperature dependence of the electrical conductivity of undoped nonstoichiometric indium oxide films. Activation energies are obtained for the formation of oxygen vacancies and for the mobility of quasifree carriers. © *1998 American Institute of Physics.* [S1063-7850(98)00102-5]

The widespread use of nonstoichiometric indium oxide films (for instance, as transparent electrodes in solar cells) has stimulated considerable interest in studies of their electrical properties.[1–5] Since these films conduct electricity by means of a vacancy mechanism, it is extremely relevant to identify the relation between the activation energy for conduction and the energy characteristics of the oxygen vacancies. However, in the literature dealing with this topic, the resultant (apparent) conduction activation energy W (Refs. 6 and 7) is usually given without analyzing the contribution of its components.

The aim of the present study was to determine the activation energy E_f for the formation of oxygen vacancies in undoped nonstoichiometric indium oxide films. The contribution made to the conduction activation energy by various processes taking place in indium oxide heated to $T=393-573$ K was analyzed by studying the temperature dependence of the conductivity of samples quenched from the annealing temperature.

Samples of undoped indium oxide films were prepared in the working chamber of a VUP-5 system by thermal deposition of metallic indium (99.999% pure) from a resistively heated tantalum evaporator ($T_i=923$ K) in an oxygen atmosphere with a partial pressure $p=10^{-2}$ Pa. The films were deposited for 5 min on glass substrates which were maintained at room temperature. The thickness of the resultant films was 0.54 μm, which corresponds to a deposition rate of 1.8 nm/s. To improve the crystal structure of the films, the samples were annealed for 5 min at $T=473$ K. The chemical composition of the indium oxide was determined by Auger electron spectroscopy using a 09IOS-10-005 Auger spectrometer. According to these data, a continuous InO_x film with stoichiometric index in the range 1.1–1.2 formed on the surface of the glass substrate.

The temperature dependence of the conductivity $\sigma(T)$ was determined by subjecting the samples to isothermal annealing in a resistively heated furnace. The concentration of oxygen vacancies N_v decreased with time since oxygen diffused from the surrounding medium into the film, filling some of the vacancies. Consequently, the resistivity of the film decreased. The vacancy concentration decreased until it reached equilibrium for the particular annealing temperature, usually 10–12 h after annealing. After the equilibrium value N_v^T had been reached, further holding did not increase the resistivity of the film.

According to the conventional model,[1] each oxygen vacancy supplies two electrons to the conduction band. The number density n (m^{-3}) of quasifree electrons is then related to the activation energy E_f for the formation of oxygen vacancies and is determined by the relation given in Ref. 8:

$$n(T)=p_{\mathrm{O}}^{-1/6}(2K_0)^{-1/3}\exp(E_f/3kT), \tag{1}$$

where p_{O} is the oxygen pressure (Pa), K_0 is the equilibrium constant for the vacancy formation reaction, k is the Boltzmann constant, and T is the temperature (K). However, it was noted in Ref. 1 that the conductivity is also influenced by the temperature dependence of the carrier mobility $\mu_e(T)$:

$$\mu_e(T)=CT^{-1/2}\exp(-E_\mu/kT), \tag{2}$$

where C is the size constant and E_μ is the mobility activation energy. The expression for the temperature dependence of the conductivity σ_1 (S/m), measured at the annealing temperature, is then given by $\sigma_1=en(T)\mu_e(T)$, which with allowance for Eqs. (1) and (2), has the form

$$\begin{aligned}\sigma_1(T)&=eCT^{-1/2}p_{\mathrm{O}}^{-1/6}(2K_0)^{-1/3}\exp(W/3kT)\\&=\sigma_0T^{-1/2}\exp(W/3kT),\end{aligned} \tag{3}$$

where e is the electron charge. Assuming that the electron density n decreases with temperature and their mobility increases, the apparent conduction activation energy W will be given by

$$W=E_f-3E_\mu. \tag{4}$$

By annealing the film at $T=373-573$ K until a steady-state value of σ_1 was reached and measuring this value directly at the annealing temperature, we obtained the temperature dependence of the steady-state conductivity $\sigma_1(T)$. It can be clearly seen (see Fig. 1, curve *1*) that the conductivity is thermally activated with the apparent activation energy $W=0.62\pm0.01$ eV. This value agrees qualitatively with the data given in Ref. 6 where the authors obtained the estimate $W=0.79$ eV in a similar temperature range. This result was

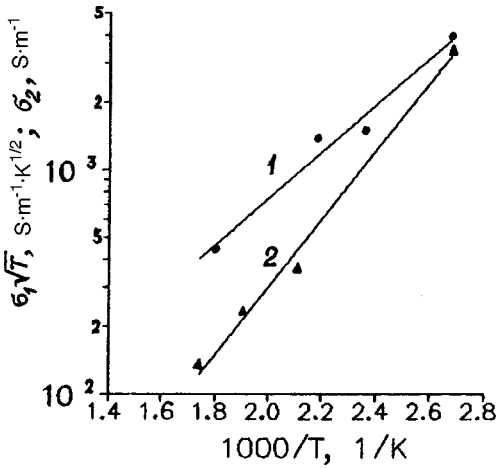

FIG. 1. Temperature dependences: *1*—$\sigma_1\sqrt{T}=f(1/T)$; *2*—$\sigma_2=f(1/T)$.

obtained for films 0.160 μm thick formed by vacuum evaporation of a pellet of stoichiometric indium oxide.

The activation energy E_f was determined by placing the samples in a furnace where they were held for a long time under isothermal conditions in air at a given temperature. The holding time was determined by the time taken for the system to reach the steady state, which was taken to be when σ varied by less than 5%. The samples were then cooled rapidly at a rate of 200 deg/min. Quenching the sample helped to maintain at room temperature the equilibrium concentration of oxygen vacancies established at the isothermal annealing temperature. Since the same measurement temperatures for σ_2 guarantee constant μ_e, the temperature dependence of the film conductivity σ_2 is determined only by the vacancy concentration established as a result of annealing, and may be described by

$$\sigma_2(T)=e\mu_e p_{\mathrm{O}}^{-1/6}(2K_0)^{1/3}\exp(E_f/3kT). \tag{5}$$

Relation (5) was used to determine the activation barrier as $E_f=1.00\pm0.01$ eV, using the experimentally measured dependence of the conductivity σ_2 on the annealing temperature, which varied in the range 373–573 K (see Fig. 1, curve *2*). The activation energy E_μ for the mobility of quasifree electrons, calculated using Eq. (4), was 0.13 ± 0.01 eV.

To sum up, we have determined the activation energy $E_f=1.00$ eV for the formation of oxygen vacancies in undoped nonstoichiometric indium oxide films. It has been shown that in addition to oxidation, the temperature dependence of the carrier mobility influences the change in the conductivity of the film with increasing temperature, and the mobility activation energy ($E_\mu=0.13$ eV) has been determined.

[1] A. L. Dawar and J. C. Joshi, J. Mater. Sci. **19**, 1 (1984).
[2] Z. M. Jarzevski, Phys. Status Solidi A **71**(13), 29 (1982).
[3] M. Higuchi, S. Uecusa, R. Nakano, and K. Yokogawa, Jpn. J. Appl. Phys. **33**, Part 1, 302 (1994).
[4] J. R. Bellingham, M. Graham, C. J. Adkins, and W. A. Phillips, J. Non-Cryst. Solids **137–138**, 519 (1991).
[5] J. C. Manifacier, Thin Solid Films **90**, 297 (1982).
[6] J. George and C. S. Menon, Indian J. Pure Appl. Phys. **33**, 700 (1995).
[7] K. B. Sundaram and G. K. Bhagavat, Phys. Status Solidi A **63**, 15 (1981).
[8] P. Kofstad, *Nonstiochiometry, Diffusion, and Electrical Conductivity in Binary Metal Oxides* (Wiley, New York, 1972; Mir, Moscow, 1975).

Translated by R. M. Durham

Control of ion beams by surface ion-acoustic wave fields

N. A. Azarenkov, A. A. Bizyukov, A. V. Gapon, and I. B. Denisenko

Kharkov State University
(Submitted April 22, 1997)
Pis'ma Zh. Tekh. Fiz. **24**, 6–11 (February 12, 1998)

It is shown for the first time that surface ion-acoustic waves may be used for polishing, etching, and depositing coatings. The proposed method of treatment is simple and convenient since the apparatus required is not cumbersome and is easy to fabricate. Compared with conventional ion beams, the proposed method of surface treatment can deliver high particle currents at the surface, which should enhance the efficiency of the material treatment. In addition, the excited surface ion-acoustic waves are natural waves, which reduces the energy consumption.
 [S1063-7850(98)00202-X]

Surface-wave plasma systems are potentially extremely useful for applications in plasma technologies.[1–3] Here we investigate the use of surface waves to control ion beams directed from a plasma onto a surface to optimize ion-plasma polishing, etching, and coating processes.

We assume that a homogeneous plasma occupies the half-space $x<0$ and a vacuum fills the region $x>0$. The surface being treated is positioned at a distance $x=1/\mathscr{K}$ from the plasma–vacuum interface, where $1/\mathscr{K}$ is the depth of penetration of the surface wave field into vacuum. Note that in this position, the surface will have a negligible influence on the surface wave field since the latter decreases e-fold at the distance $1/\mathscr{K}$. Under actual conditions, instead of a vacuum layer between the plasma and the surface, there is a transition layer which, to a first approximation, is frequently modeled by a vacuum region,[4] as we do here.

We shall consider surface wave perturbations propagating along the plasma–vacuum interface (the z axis), whose amplitude decreases with increasing distance from this interface. We take the dependence of these perturbations on the time t and spatial coordinate z in the form $A(\bar{r},\bar{t})=A(x)\exp(i(k_3z-\omega t))$, where k_3 is the projection of the wave vector on the z axis and ω is the wave frequency. If the electron temperature T_e is much higher than the ion temperature T_i, a surface ion-acoustic wave (SIAW)[4] can propagate in this structure in the frequency range $\omega<\Omega_i/\sqrt{2}$ (where $\Omega_i=\sqrt{4\pi e^2n_0/m_i}$ is the plasma ion frequency, and e, n_0, and m_i are the charge, density, and mass of the plasma ions, respectively). The dispersion equations for SIAWs in this structure have the form

$$k_3\approx-\varepsilon_i q_1, \tag{1}$$

where $\varepsilon_i=1-\Omega_i^2/\omega^2$; $q_1^2=k_3^2+1/(r_D^2\varepsilon_i)$, $r_D=v_{\mathrm{Te}}/\Omega_e$, $\Omega_e=\sqrt{4\pi e^2n_0/m_e}$, m_e is the electron mass, $v_{\mathrm{Te}}=(\gamma T_e/m_e)^{1/2}$ is the average thermal velocity of the electrons, and γ is the adiabatic exponent.

Using the Maxwell equations and the equations of quasihydrodynamics, we can derive systems of equations describing the ion motion in an SIAW field with allowance for an auxiliary extracting field concentrated in the vacuum region:

In vacuum ($x>0$),

$$m_i\frac{d^2x}{dt^2}=e\varepsilon_iB\,\exp(-k_3x)\cos(k_3z-\omega t)+eE_0,$$

$$m_i\frac{d^2z}{dt^2}=e\varepsilon_iB\exp(-k_3x)\sin(k_3z-\omega t); \tag{2}$$

in the boundary region,

$$m_i\frac{d^2x}{dt^2}=e\frac{B}{2}(\varepsilon_i\,\exp(-k_3x)+\exp(q_1x))\cos(k_3z-\omega t)+eE_0/2,$$

$$m_i=\frac{d^2z}{dt^2}=-eB\frac{k_3}{q_1}\exp(q_1x)\sin(k_3z-\omega t); \tag{3}$$

in the plasma ($x<0$),

$$m_i\frac{d^2x}{dt^2}=eB\,\exp(q_1x)\cos(k_3z-\omega t),$$

$$m_i\frac{d^2z}{dt^2}=-eB\frac{k_3}{q_1}\exp(q_1x)\sin(k_3z-\omega t), \tag{4}$$

where B is the wave amplitude.

The existence of a potential difference between the plasma and the surface being treated means that the parameters of the ion beam extracted from the SIAW plasma can also be varied.

The systems (2)–(4), and (1) were used to investigate the ion motion in a SIAW field for an argon plasma.

Figure 1 shows the energy distribution functions $f(\varepsilon)$ of particles reaching the surface being treated for different ratios of the SIAW amplitude to the extracting field ($\int_0^\infty f(\varepsilon)d\varepsilon$ is the ratio of the number of particles reaching the surface to the total number of accelerated particles). All the curves were obtained for the following parameters: $\omega/2\pi=4\times10^4$ Hz, $A^v=300$ eV, $n_0=10^{12}$ cm^{-3}, and $T_e=3$ eV, where $A^v=|e\varepsilon_iB|$. The particle energy distribution in the absence of an extracting field is given by curve *1*. When the extracting field is increased to $E_0=0.5A^v$ (curve *2*), the distribution function is almost the same as before, but the average energy of the particles reaching the surface increases and the peak of the distribution function is shifted

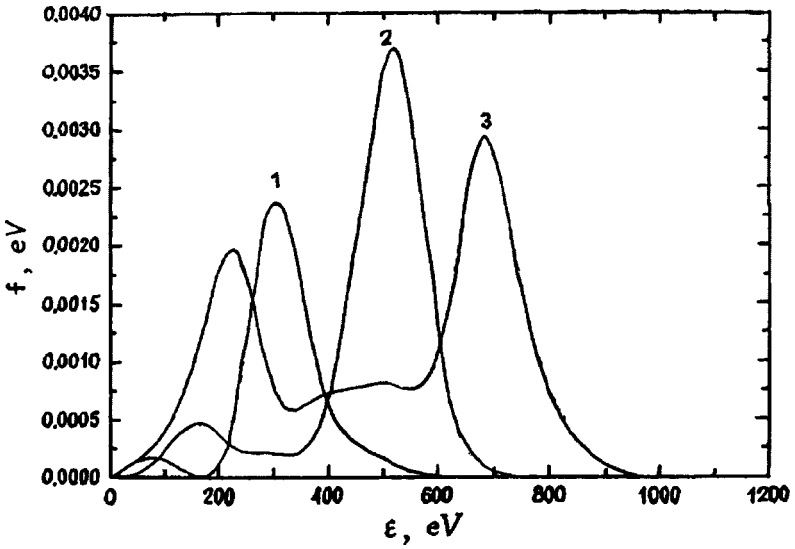

FIG. 1. Energy distribution function of ions incident on surface being treated.

toward higher energies, The number of particles reaching the surface is almost doubled compared with the case with no extracting field. Applying the extracting field $E_0=A^v$ changes the form of the distribution function, which now has two peaks (curve *3*).

Figure 2 shows the distribution functions $f(\varphi)$ plotted against the angles of incidence on the surface. In this case, $\int_0^{\pi/2} f(\varphi)d\varphi$ is the ratio of the number of particles reaching the surface to the total number of accelerated particles. The functions $f(\varphi)$ are plotted for the same parameters as in Fig. 1. Curves *1*, *2*, and *3* correspond to the cases $E_0=0$, $E_0=0.5A^v$, and $E_0=A^v$, respectively. It can be seen that in the absence of an extracting field, the dependence $f(\varphi)$ is almost constant, i.e., for $E_0=0$ there is no single clearly defined direction of particle motion. When the accelerating field $E_0=0.5A^v$ is applied, no particles with angles of incidence greater than 75° are observed but the total number of particles incident on the surface increases. In this case, the distribution function is almost constant in the range $5<\varphi<60°$. When the extracting field is increased further to $E_0=A^v$ (curve *3*), the particles reach the surface at angles less than 50° and a fairly large number are incident at angles close to 40°.

Thus, the results of this study of ion motion in an SIAW field indicate that a plasma-transition layer-surface structure with propagation of an SIAW is an efficient ion-optical system for a wide range of ion beam parameters. By suitably selecting the SIAW frequency, charged particle concentration, electron temperature, SIAW wave amplitude, and auxiliary extracting field strength, it should be possible to produce ion beams with different angular parameters and average energy at the surface.

1) In the absence of an auxiliary extracting field, of order 50% of the total number of particles reach the surface and bombard it almost uniformly over the entire angular range. The ion beam in this case is particularly efficient for ion-plasma polishing of surfaces.[5]

2) If the extracting field is less than half the SIAW amplitude, an ion beam is formed in which more than half the

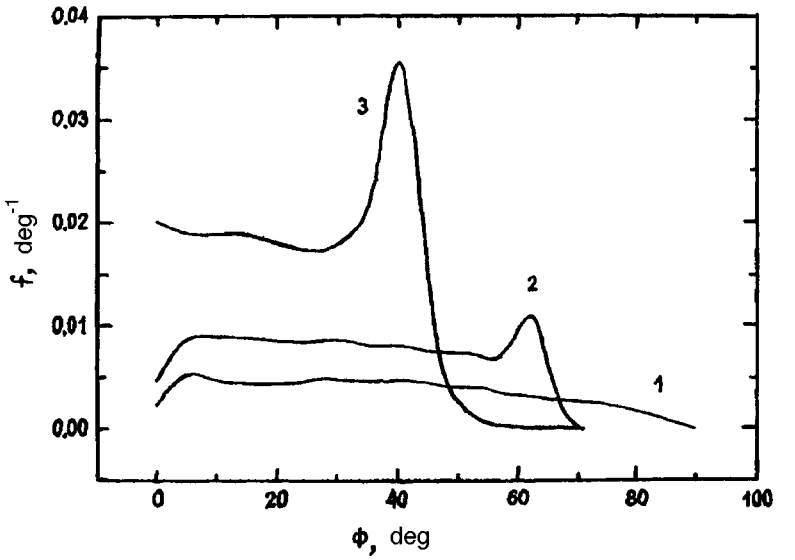

FIG. 2. Distribution function of angles of incidence on surface being treated.

ions pulled from the plasma reach the surface at angles of 30–70°. Ion beams with these angles of incidence are suitable for ion etching of surface holographic gratings with an oblique-angled profile.[6]

3) When the extracting field is on the order of the surface wave amplitude, an ion beam is formed in which most of the particles reach the surface at angles of 10–40°. The use of ion beams with these angles of incidence in technologies involving the plasma-stimulated deposition of thin films may well solve the problem of depositing thin films on profiles with sharp steps, typical of the technological relief of microelectronics devices. Using ion beams with a preferential angle of incidence of 10–40° to etch thin films eliminates the formation of grooves and overdeposition of material at perpendicular steps on a relief with a vertical etching profile.[7,8]

[1] J. Margot and M. Moisan, in *Microwave Discharges: Fundamentals and Applications*, edited by C. M. Ferreira and M. Moisan, NATO ASI Series, Series B, Physics, Vol. 302 (Plenum Press, New York, 1983), p. 141.
[2] Yu. M. Aliev, K. M. Ivanova, M. Moisan, and A. P. Shivarova, Plasma Sources Sci. Technol. **2**, 145 (1993).
[3] C. F. M. Borges, M. Moisan, and A. Gicquel, Diamond Relat. Mater. **4**, 149 (1995).
[4] A. N. Kondratenko, *Surface and Bulk Waves in a Confined Plasma* [in Russian], Énergoatomizdat, Moscow (1985).
[5] B. A. Heath and T. M. Mayer, in *Plasma Processing for VLSI*, edited by N. G. Einspruch and D. M. Brown, Vol. 8 of VLSI Electronics (Academic Press, New York, 1984; Mir, Moscow, 1987).
[6] S. Matsui, T. Yamamoto, H. Aritome, and S. Namba, Jpn. J. Appl. Phys. **19**, L126 (1980).
[7] S. Somekh, J. Vac. Sci. Technol. **13**, 1003 (1976).
[8] R. E. Lee, J. Vac. Sci. Technol. **16**, 164 (1979).

Translated by R. M. Durham

Entropy of glass transition and polymorphism

M. D. Bal'makov, L. N. Blinov, and N. S. Pocheptsova

St. Petersburg State Technical University
(Submitted May 22, 1997)
Pis'ma Zh. Tekh. Fiz. **24**, 12–17 (February 12, 1998)

An analysis is made of the change in entropy in the glass transition process. It is shown that although the entropy of glass transition is less than that of melting, it is no more than two orders of magnitude smaller. The main results are obtained without using the conditions of local equilibrium, which are not satisfied for the glassy state. © *1998 American Institute of Physics.* [S1063-7850(98)00302-4]

The theory of disordered system is by no means complete, with many problems still to be completely resolved. For instance, the change in entropy at the glass transition point during cooling of a liquid is a topic under discussion.[1] Does the entropy $S(T)$ change abruptly (Fig. 1a) or continuously (Fig. 1b) at the glass transition temperature T_g?

In the first case, we can talk of a glass transition entropy ΔS_g (Ref. 2) which is equal to the difference between the ordinates of points B and A (Fig. 1a) which define the limits of the glass transition range. Point A is the end point of curve g, which describes the entropy $S(T)$ of glass, and similarly point B is the end point of curve l corresponding to a metastable liquid (Fig. 1). Clearly, it is difficult to determine the nature of the glassy state,[3] without considering the glass transition entropy ΔS_g. This is not the only reason why ΔS_g is important. It is also related to various unsolved problems in physics and chemistry, as will be shown subsequently.

In the second case (Fig. 1b), which is the only alternative to the first (Fig. 1a), there is no glass transition entropy $(\Delta S_g = 0)$, since points A and B coincide. This implies that the transition from the liquid to the glassy state and the reverse is an equilibrium process. Numerous experimental and theoretical data[3] indicate precisely the opposite, that the glass transition is a nonequilibrium process. Thus, this alternative (Fig. 1b) should be eliminated from the analysis.

Other facts also support this viewpoint.[2] For instance, a liquid, unlike glass, exhibits fluidity and this requires a substantially larger number G of accessible[4] quantum states compared with that for a solid. Thus, the following inequality is satisfied

$$G_l > G_g, \tag{1}$$

where G_l is the number of permissible quantum states for a liquid and G_g is that for glass. Assuming that the entropy S expressed in absolute units is given by[4]

$$S = \ln G, \tag{2}$$

we obtain the following relations for the glass transition entropy ΔS_g

$$\Delta S_g = \ln \frac{G_l}{G_g} > 0, \tag{3}$$

where G_l and G_g are the numbers of permissible quantum states of liquid and glass, respectively, at temperatures close to the glass-transition temperature T_g. The fact is that the abscissas of points A and B (Fig. 1a) are only the same and equal to T_g in the limiting case, when a liquid undergoes infinitely slow cooling to T_g followed by instantaneous quenching. These abscissas differ slightly depending on the results of each specific experiment.

It is not so easy to obtain a numerical value of ΔS_g (3). First, ''Even the problem of defining entropy outside the state of equilibrium is clearly a subject which goes beyond macroscopic thermodynamics'' (Ref. 5, p. 29). ''... For equilibrium systems a definition of entropy was given by Gibbs, for nonequilibrium systems no definition is known as yet ...'' (Ref. 6, p. 1907). Note that the glass transition is a nonequilibrium process. Such processes are conventionally indicated by bars because of their indeterminacy (Fig. 1a). The glassy state itself is also nonequilibrium.[3] Thus, before applying methods of linear nonequilibrium thermodynamics, it must be demonstrated that conditions of local equilibrium are satisfied for the glassy state,[5] which so far has not been accomplished.

Secondly, entropy cannot be measured directly like temperature or volume—entropy meters do not exist. Indirect methods of calculating entropy are by no means always accurate.[2] This particularly applies to nonequilibrium processes, since we cannot in principle use calculation methods based on the well-known relation[4]

$$dS = \frac{\delta Q}{T}, \tag{4}$$

which can be used to find the differential dS of the entropy with respect to the energy release δQ of an elementary equilibrium process. Thus, the change in entropy ΔS_g in the glass transition range cannot be calculated merely using calorimetric data. Different approaches must be adopted.[2]

Such approaches are based on the Boltzmann definition of entropy S (Ref. 4)

$$S = -\sum_i P_i \ln P_i; \tag{5}$$

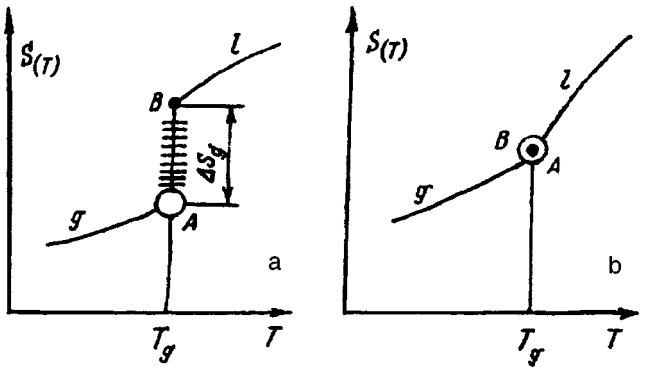

FIG. 1. Temperature dependences of the entropy $S(T)$.

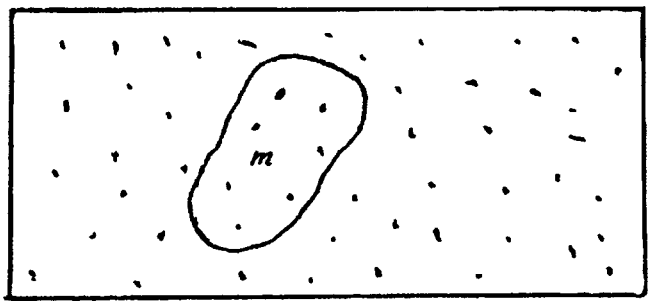

FIG. 2. Single fragment containing m atoms. The dots indicate the centers of regions of localization of atomic nuclei.

here, summation is performed over all steady quantum states whose probabilities of realization are P_i. Naturally, the definition (5) does not solve all the entropy problems in nonequilibrium systems.[5,6] In this context, we also note the paradox of the negative production of entropy.[7]

For temperatures significantly greater than absolute zero, the entropy S (5) of a condensed system may be approximated by the sum[2]

$$S \approx S^{(c)} + S^{(\mathrm{ph})} \tag{6}$$

of the configurational entropy $S^{(c)}$ and the entropy $S^{(\mathrm{ph})}$ attributable to the kinetic energy of the atomic nuclei

$$S^{(\mathrm{ph})} = \sum_k P_k S^{(\mathrm{ph})}_{k_\parallel}. \tag{7}$$

Here P_k is the probability of realization of the kth configuration, which corresponds to the kth minimum $\mathbf{R}_k$ of the adiabatic electronic term $U_m(\mathbf{R})$ (Refs. 3 and 8), and $S_k^{(\mathrm{ph})}$ is the entropy of the phonon subsystem for the case where the atomic nuclei are localized near the minimum $\mathbf{R}_k$.

The glass transition process essentially involves ''freezing'' of various configurational degrees of freedom. Thus, the main contribution to the glass transition entropy ΔS_g (Fig. 1a) is made by the change in the configurational entropy $S^{(c)}$ (6). If the change in S^{ph} (7) during the glass transition process can be neglected, we have the following estimate for the glass transition entropy (3):

$$\Delta S_g \approx S_l^{(c)} - S_g^{(c)}, \tag{8}$$

where $S_l^{(c)}$ and $S_g^{(c)}$ are the configurational entropies of liquid and glass at temperatures close to T_g (Fig. 1).

Relation (8) can be conveniently used with the partition theorem,[3] according to which any disordered system can be represented as a set of fragments, each containing m atoms. We select a sufficiently small fragment (Fig. 2) such that only one short-range order can be realized within this fragment, with most of the atomic nuclei external to this fragment in a fixed position. This fixing does in fact occur in glasses, whose atomic nuclei in most cases only undergo small vibrations near the equilibrium positions.

In liquids, on the other hand, the atomic nuclei exhibit both vibrational and translational motion. This mobility means that for liquids in general, different short-range orders can be established within this particular fragment (Fig. 2). These correspond to different polymorphic forms[9] whose number is denoted by j. Relation (8) can then be represented in the form

$$\Delta S_g \approx \ln j C_l - \ln C_g, \quad C_l > C_g \geqslant 1, \tag{9}$$

where the cofactors C_l and C_g allow for the possibility of liquid and glass with different structures having the same short-range order being realized in the fragment (Fig. 2), respectively. Note that the same short-range order generally corresponds to a large number of different structures (the minimum of the potential $U_m(\mathbf{R})$) (Ref. 3).

Relation (9) can be used to estimate the ratio of the glass transition entropy ΔS_g to the melting entropy ΔS_m. The melting entropy ΔS_m, expressed in absolute units[4] relative to a single atom, is contained within a comparatively narrow range 0.8–1.7 (Ref. 10). Thus, the estimate $\Delta S_m \approx 1.2m$ is valid. From Ref. 9 for $j \geqslant 2$ we then have

$$\frac{\Delta S_g}{\Delta S_m} \approx \frac{\ln j \dfrac{C_l}{C_g}}{1.2m} > \frac{\ln 2}{1.2m}. \tag{10}$$

Since the fragment under study (Fig. 2) is fairly small ($m < 50$), we obtain from expression (10)

$$\frac{\Delta S_g}{\Delta S_m} > 0.01. \tag{11}$$

Inequality (11) is in complete agreement with the hypothesis put forward in Ref. 2, whereby the glass transition entropy ΔS_g is smaller than the melting entropy ΔS_m but by no more than a factor of a hundred. This approach may be useful for assessing the possibility of developing new disordered materials, especially those based on fullerenes, and also for understanding the role of polymorphic modifications in the glass transition process.[9,11]

[1] S. M. Stishov, Usp. Fiz. Nauk **154**, 93 (1988) [Sov. Phys. Usp. **31**, 52 (1988)].
[2] M. D. Bal'makov, Glass Phys. Chem. **22**, 344 (1996).
[3] M. D. Bal'makov, *The Glassy State of Matter* [in Russian], St. Petersburg State University Press, St. Petersburg (1996).
[4] C. Kittel, *Thermal Physics*, 2nd ed., Freeman, San Francisco (1980).
[5] P. Glansdorff and I. Prigogine, *Thermodynamic Theory of Structure, Stability and Fluctuations* (Wiley, New York, 1971; Mir, Moscow, 1973).
[6] G. A. Martynov, Zh. Éksp. Teor. Fiz. **107**, 1907 (1995) [JETP Lett. **80**, 1056 (1995)].
[7] M. D. Bal'makov, Vestn. St. Petersburg. Gos. Univ. Ser. 4. No. 1(4), 133 (1996).

[8] L. N. Blinov, M. D. Bal'makov, and N. S. Pocheptsova, Pis'ma Zh. Tekh. Fiz. **22**(21), 69 (1996) [Tech. Phys. Lett. **22**, 894 (1996)].
[9] L. N. Blinov, M. D. Bal'makov, and N. S. Pocheptsova, Pis'ma Zh. Tekh. Fiz. **14**(1), 86 (1988) [Sov. Tech. Phys. Lett. **14**, 39 (1988)].
[10] J. M. Ziman, *Models of Disorder: the Theoretical Physics of Homogeneously Disordered Systems* (Cambridge University Press, Cambridge, 1979; Mir, Moscow, 1982).
[11] L. N. Blinov, *Glassy Semiconductors* [in Russian], Nauka, Leningrad (1985), pp. 176–177.

Translated by R. M. Durham

Investigation of the properties of $CuGaTe_2$ thin films

I. V. Bodnar', V. F. Gremenok, I. A. Viktorov, and D. D. Krivolap

Belarus State University of Informatics and Radioelectronics, Minsk, Belarus; Institute of Solid-State and Semiconductor Physics, Minsk, Belarus

(Submitted July 11, 1997)
Pis'ma Zh. Tekh. Fiz. **24**, 18–23 (February 12, 1998)

Thin films of the ternary compound $CuGaTe_2$ were prepared by pulsed laser-assisted evaporation. Their structure and unit cell parameters were determined by an x-ray method. The transmission spectra near the fundamental absorption edge were used to determine the energies of the interband optical transitions, and the crystal (Δ_{cr}) and spin-orbit (Δ_{∞}) splittings were calculated. © *1998 American Institute of Physics.* [S1063-7850(98)00402-9]

The ternary compound $CuGaTe_2$ belongs to the class of I–III–VI_2 compounds which crystallize to form a chalcopyrite structure (space group $D_{2d}^{12}-142d$) and is a promising material for various optoelectronics devices.[1] This compound has been little studied because of the difficulties involved in producing high-quality single crystals and films. In Ref. 2, we studied the electrical, optical, and thermal properties of $CuGaTe_2$ crystals obtained by a two-temperature method.

Here we report the results of a study of the structure and optical properties of thin $CuGaTe_2$ films prepared by pulsed laser-assisted evaporation. Crystals synthesized by directional crystallization of a melt were used as the target.[3]

The films were deposited in a vacuum of $(2-4)\times10^{-5}$ Torr using a Nd:YAG laser ($\lambda=1.06$ μm, $\tau_p=10^{-3}$ s, and $E_p=150-180$ J) (Ref. 4). The substrates were chemically purified glasses whose temperature was maintained at $\sim$690 K. The thickness of the $CuGaTe_2$ films was 0.6 μm.

The composition of the films was determined by microprobe x-ray spectral analysis. The data indicate that the atomic composition (to within $\sim$4%) is consistent with the formula $CuGaTe_2$ and was reproduced in diagnostics of different sections of the film.

The structure and parameters of the crystals and films were determined by an x-ray technique. Diffraction patterns were recorded with a DRON-3M x-ray diffractometer using Cu K_α radiation and a nickel filter. These studies showed that the diffraction patterns of the films (like the $CuGaTe_2$ crystals) exhibited a system of lines consistent with a chalcopyrite structure. The unit cell parameters, calculated from the reflections for which $2\Theta>65°$, are $a=6.023\pm0.005$ Å and $c=11.92\pm0.01$ Å, which agrees with the data for bulk crystals ($a=6.024\pm0.005$ Å and $c=11.93\pm0.01$ Å) (Refs. 2, 3, and 5).

Electrical measurements of the $CuGaTe_2$ films showed that these possessed p-type conductivity and a resistivity of $\sim4\times10^{-2}$ $\Omega\cdot$cm.

For these $CuGaTe_2$ films we also measured the spectral distribution of the transmission and reflection coefficients near the fundamental absorption edge. The spectra were recorded using Beckman-5270 and Specord-GINIR spectrophotometers at 293 K in the spectral range 500–2000 nm. The absorption coefficient was calculated using the formula:

$$\alpha=\frac{1}{d}\ln(A+\sqrt{A^2+R^2}), \tag{1}$$

where d is the thickness of the sample, $A=(1-R)^2/2T$, T is the transmission, and R is the reflection coefficient in the range 0.5–1.3 μm, which is constant at $\sim$30% (Ref. 6).

Figure 1a shows the transmission spectrum of the $CuGaTe_2$ films. The fairly high transmission near the fundamental absorption edge (above 40%) and the distinct interference pattern indicate that the deposited films are of high quality.

Figure 1b gives the spectral dependence of the optical absorption coefficient (α) as a function of the photon energy. It can be seen that these $CuGaTe_2$ films exhibit a high absorption coefficient in the range under study (10^4-10^5 cm^{-1}) and the fundamental absorption edge has a complex structure which, in accordance with the Hopfield model[7] for I–III–VI_2 compounds, is caused by p-d hybridization of the valence band in these compounds.

An analysis of this curve reveals that the main contribution to the absorption structure of the $CuGaTe_2$ films is made by the direct allowed transitions given by

$$\alpha=\frac{A}{h\nu}(h\nu-E_g)^{1/2}. \tag{2}$$

Figure 2 gives $(\alpha\cdot h\nu)^2$ as a function of the photon energy used to determine the energies of the interband transitions. We obtained the following optical transition energies for $CuGaTe_2$: $E_{g1}=1.35\pm0.01$ eV, $E_{g2}=1.43\pm0.01$ eV, $E_{g3}=1.88\pm0.01$ eV, which agrees with the results[5] of studying the photoluminescence of bulk crystals.

On the basis of our results and the data given in Refs. 5 and 6, we can conclude that the transition with $E_{g1}=1.35$ eV corresponds to the $\Gamma_7^V-U_6^C$ valence–conduction band transition. The transition $E_{g2}=1.43$ eV is attributed to the splitting (Δ_{cr}) of the valence band under the action of the crystal lattice field $\Gamma_6^V-\Gamma_6^C$ and the transition $E_{g3}=1.88$ eV is attributed to the spin-orbit splitting (Δ_s) of the valence band $\Gamma_7^V-\Gamma_6^C$.

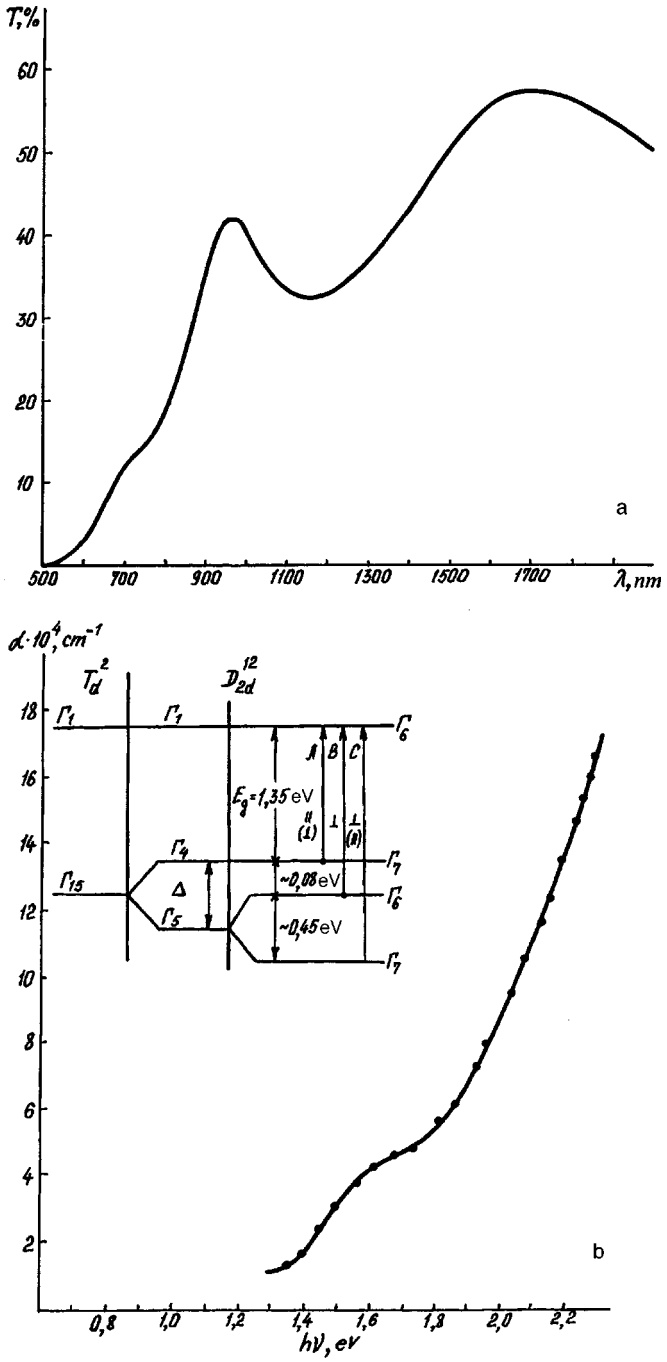

FIG. 1. a—Transmission spectra of $CuGaTe_2$ films, 0.6 μm thick; b—absorption coefficient (α) versus photon energy ($h\nu$).

In accordance with the quasicubic Hopfield model, the energies of the crystal and spin-orbit splitting of the valence band were calculated as follows:[6]

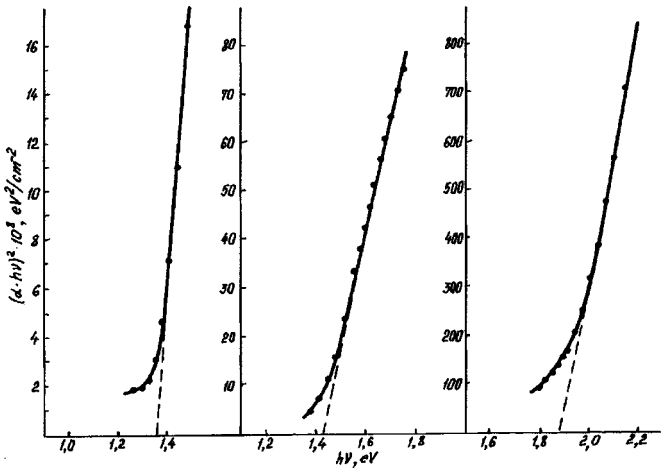

FIG. 2. Spectral dependence of $(\alpha h\nu)^2$ on photon energy.

$$\Delta_{cr}=\frac{E_2+E_1}{2}-\frac{1}{2}[(E_2+E_1)^2-6E_1E_2]^{1/2}, \tag{3}$$

$$\Delta_{so}=\frac{E_2+E_1}{2}+\frac{1}{2}[(E_2+E_1)^2-6E_1E_2]^{1/2}, \tag{4}$$

where $E_1=E_{g1}-E_{g2}$; $E_2=E_{g3}-E_{g2}$.

For $CuGaTe_2$ films these values are $\Delta_{cr}=-0.115$ eV and $\Delta_{so}=0.485$ eV.

CONCLUSIONS

The structural and optical properties of ternary $CuGaTe_2$ films prepared by laser-assisted evaporation have been investigated. It has been shown that like the bulk crystals, $CuGaTe_2$ films crystallize in a chalcopyrite structure. The unit cell parameters have been determined for these crystals and films and the interband transition energies have been calculated together with the crystal and spin-orbit splittings.

[1] T. Coates and J. Mikin, *Contemporary Problems in Semiconductor Photoenergetics* [Russ. transl., Mir, Moscow, 1988], p. 307.
[2] I. V. Bodnar', Neorg. Mater. **27**, 2068 (1991).
[3] I. V. Bodnar and N. S. Orlova, Cryst. Res. Technol. **21**, 1091 (1986).
[4] I. V. Bodnar, V. P. Gremenok, E. P. Zaretskaja, and I. V. Victorov, Thin Solid Films **207**, 54 (1992).
[5] G. Massé, K. Djessas, and L. Yarzhou, J. Appl. Phys. **74**, 1376 (1993).
[6] J. L. Shay and J. H. Wernick, *Ternary Chalcopyrite Semiconductors: Growth, Electronic Properties and Applications* (Pergamon Press, Oxford, 1975), p. 244.
[7] J. L. Shay, B. Tell, H. M. Kasper, and L. M. Schiovane, Phys. Rev. B **5**, 5003 (1972).

Translated by R. M. Durham

Background doping of films in molecular beam epitaxy of silicon

B. Z. Kanter, A. I. Nikiforov, and O. P. Pchelyakov

Institute of Semiconductor Physics, Siberian Branch of the Russian Academy of Sciences, Novosibirsk
(Submitted July 14, 1997)
Pis'ma Zh. Tekh. Fiz. **24**, 24–29 (February 12, 1998)

Unique results obtained as a result of the development of epitaxial silicon layers with an extremely low concentration of background impurities for infrared photodetectors with blocked impurity photoconduction are analyzed and generalized. Changes in the type and concentration of electrically active background impurities in films grown by molecular beam epitaxy were investigated at all stages in the operation of the system, from initial startup to the fabrication of films having an extremely low level of background impurities $<4\times10^{13}$ cm^{-3}. The laws governing the changes in the type and level of background doping during operation of the system and the mechanism responsible for these changes are established. © *1998 American Institute of Physics.* [S1063-7850(98)00502-3]

The development and industrial application of molecular beam epitaxy have shown that this is the best method of growing multilayer epitaxial structures with atomically smooth boundaries and precise layer thickness, composition, and doping profile. However, when molecular beam epitaxy is implemented in high-vacuum systems, the quality of the structures is limited by the degree of vacuum and by the efficiency of the pumping system. The parameters of the films are adversely influenced if the vacuum chamber walls have developed surfaces which accumulate and then release components of the molecular beams and the residual gas atmosphere. In order to overcome these shortcomings, the idea of transferring an unenclosed molecular beam epitaxy system into space in the ''wake'' region of a molecular screen has recently been successfully implemented.[1–3] An analysis of trends in the development of integrated circuit technology and related equipment, including high-vacuum cluster systems, yields the conclusion that the future of fully integrated production lines lies in transferring them to space.[4]

In order to produce extremely high-quality epitaxial structures on Earth and in space, we need to know the laws determining the type and level of accidental background doping. Here we report the first investigations of background doping in the molecular beam epitaxy of silicon, which is accompanied by change in the type and concentration of carriers in the films (electrons N_n and holes N_p). The investigations were carried out at all stages in the operation of the Katun'-S system: from initial startup to growth of films with an extremely low background impurity level $N_p<4\times10^{13}$ cm^{-3}. Direct measurements of molecular fluxes of background impurities were almost eliminated because of their low intensity, and information on sources of these impurities and their transport processes was derived from systematic measurements of N_n and N_p.

The growth chamber contained two electron-beam evaporators for silicon and germanium, as well as two resistively-heated sources of molecular impurities. After all the equipment had been assembled, the growth chamber was outgassed at 300 °C and evacuated to 10^{-8} Pa using magnetic discharge and sublimation pumps. Prior to epitaxy, the surface of the 60 mm diameter KÉF-5 (100) and KDB-30 (111) silicon substrates was purified by heating to 800 °C in a weak silicon flux.[5] The films were grown at substrate temperatures of 500–900 °C. The thickness of the films was 3–5 μm. The concentration of electrically active impurities was estimated by measuring N_n and N_p using a C-V profilometer; the results are plotted in Fig. 1. The arrows indicate the times when the growth chamber was opened to atmosphere and the heating cycle repeated. At times ''1'' and ''2'' small components were replaced in the growth chamber, at time ''3'' the molecular sources containing Sb and B_2O_3 were installed, and at time ''4'' the B_2O_3 source was removed.

The sources were not switched on for the entire investigation. The maximum concentration of background impurities (around 10^{16} cm^{-3}) was observed in films grown immediately after assembly and outgassing of the chamber. During operation the concentration N_n in the films decreased at around an order of magnitude per 10–15 wafers, which corresponds to an as-grown silicon layer with a total thickness of 50 μm. In the initial stage of operation (wafers 1–35), N_n rose sharply on each occasion after the chamber was opened up and new components or assemblies inserted, although the maximum and the rate of decay of N_n gradually decreased and p-type impurities began to predominate in the films. Then, opening up the growth chamber and subsequent annealing did not give rise to any n-type impurities in the films (times ''3'' and ''4''). Unlike the n-type impurities, the concentration of p-type impurities varied only slightly, approaching 10^{14} cm^{-3}. After the molecular source containing B_2O_3 had been installed (time ''3'' in Fig. 1), the concentration N_p increased by two orders of magnitude and decreased very slowly during the operating process. Removing the B_2O_3 source from the chamber caused N_p to fall rapidly to a constant level of 4×10^{13} cm^{-3}.

An analysis of the epitaxy results at various temperatures and growth rates (Fig. 2) shows that N_n is almost independent of the epitaxy temperature and proportional to the

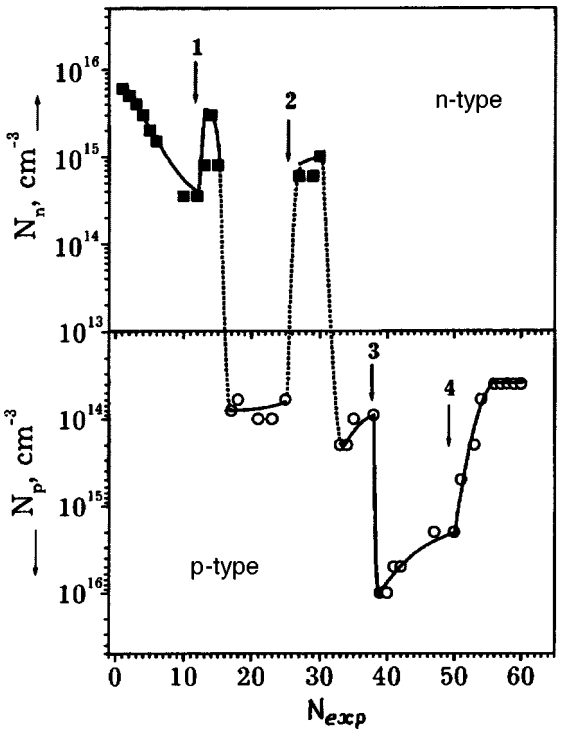

FIG. 1. Concentration of electrically active donor (N_n) and acceptor (N_p) impurities in silicon films grown at 800 °C. The estimates were based on C-V measurements. The wafer numbers of the silicon substrates, which follows the sequence of experiments, are given on the abscissa.

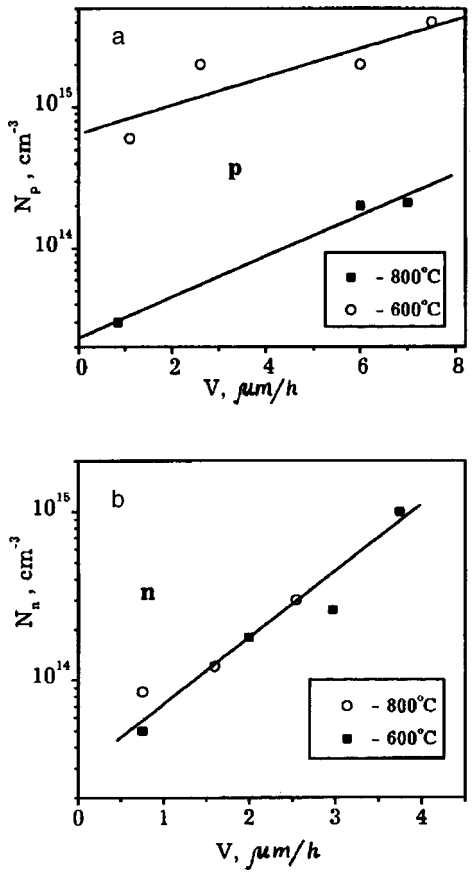

FIG. 2. Dependences of N_n and N_p on the substrate temperature (a) and growth rate (b).

growth rate (Fig. 2a). Conversely, N_p depends strongly on the growth temperature and the activation energy for the incorporation of acceptor impurities is 1.1 eV (Fig. 2b). Histograms linking the film and substrate parameters show that the type and level of doping of the films does not depend on the type and concentration of impurities in the substrate, i.e., the self-doping process is not a decisive factor in this case. The presence of a cold Sb source in the chamber did not significantly influence the measurable carrier concentration in the films. These results yield the following conclusions.

1. Two main background doping regimes are observed: a transition regime after assembly and startup, during which the epitaxial films are doped by n-type background impurities whose level decreases monotonically, and a steady-state regime where p-type background impurities predominate, whose level subsequently varies negligibly.

2. The background doping in the transition regime is caused by an influx of impurities from the surface of the chamber walls and installed components. The most likely impurities are phosphorus or manganese incorporated in the stainless steel. A comparison with the results of Refs. 6 and 7 gives an estimated flux of background impurities to the film of 10^{11}–10^{12} atoms/cm^2·s immediately after assembly and startup. In the steady-state regime the flux is reduced by three orders of magnitude.

3. Doping of the films with acceptor impurities in the steady-state regime is most likely caused by the presence of boron-containing components on the substrate surface prior to epitaxy and by boron being generated at heated ceramic components and then transported via the chamber walls.

4. When the baffle is closed, impurities are transported from the B_2O_3 source to the growing film across the surface of the chamber walls by means of repeated evaporation-condensation cycles involving highly volatile impurity components.

These results suggest that when films are grown in space using an unenclosed molecular beam epitaxy system, background doping will be reduced substantially because of the absence of chamber walls and the enhanced pumping efficiency. An efficient means of reducing the time taken for transition to the steady state may involve preparing the technological apparatus on Earth by depositing a film of silicon or another efficient sorbent on its inner surfaces.

This work was supported by the State Scientific-Technical Programs ''Fundamental Space Research'' (Epitaxy Project), ''Physics of Solid-State Nanostructures'' (Project 2-011), and the Russian Fund for Fundamental Research (Grant No. 97-02-18409).

[1] J. E. Hieser and F. J. Brock, J. Vac. Sci. Technol. **13**, 702 (1976).
[2] A. Ignatiev, Earth Space Rev. **2**(2), 10 (1995).
[3] O. P. Pchelyakov, L. V. Sokolov, A. I. Nikiforov, V. I. Berzhaty, L. L. Zvorikin, A. I. Ivanov, V. P. Nikitsky, V. Yu. Antropov, V. M. Biriukov, E. V. Markov, and Yu. N. Djakov, in *Proceedings of the Joint Tenth European and Sixth Russian Symposium on Physical Sciences in Microgravity*, St. Petersburg, Russia, 1997, p. 119.

[4] K. Valiev and A. Orlikovskiĭ, Elektronika Nauka Tekhnol. Biznes No. 5–6, 3 (1996).
[5] A. Ishizaka, K. Nakagawa, and Y. Shiraki, Jpn. J. Appl. Phys. , 183 (1982).
[6] A. Yu. Andreev, N. B. Gudkova, V. P. Kuznetsov, V. S. Krasil'nikov, R. A. Rubtsova, and V. A. Tolomasov, Izv. Akad. Nauk SSSR, Neorg. Mater. **24**, 1423 (1988).
[7] A. V. Rzhanov, S. I. Stenin, O. P. Pchelyakov, and B. Z. Kanter, Thin Solid Films **139**, 169 (1986).

Translated by R. M. Durham

Concentration dependence of the influence of strain rate on the yield stress of doped NaCl crystals under uniaxial compression in the temperature range 77–773 K

R. P. Zhitaru, N. A. Palistrant, and V. A. Rakhvalov

Institute of Applied Physics, Moldavian Academy of Sciences, Kishinev
(Submitted June 10, 1997)
Pis'ma Zh. Tekh. Fiz. **24**, 30–37 (February 12, 1998)

Anomalies in the dependence of the yield stress of sodium chloride crystals on the strain rate are described for varying composition and impurity concentration and varying temperature. Explanations are proposed for these anomalies based on specific characteristics of dislocation motion in an impurity atmosphere. © *1998 American Institute of Physics.* [S1063-7850(98)00602-8]

It has been established that as the strain rate $\dot{a}$ of alkali halide crystals under uniaxial compression increases, the yield stress σ_y increases.[1–4] However, this rate dependence of the yield stress is not always found for doped crystals. In addition to the usual behavior of $\sigma_y(\dot{a})$, under certain test conditions and for certain dopant concentrations NaCl crystals have an unusual dependence in which the yield stress decreases rather than increases with increasing strain rate.[5,6] Results obtained for doped crystals in Refs. 3 and 7 are also contradictory in many cases. This is because comparatively few studies have been made of the influence of the strain rate on deformation processes in crystals containing different types of impurity defects. In view of this, we studied how the type and concentration of impurities influences the dependence of the yield stress on the testing rate over a wide range of temperature to gain a deeper understanding of the mechanism for the plastic deformation of crystals.

We studied NaCl crystals doped with Ca, Pb, and Sr, grown by the Czochralski method at Tomsk Polytechnic Institute. The impurity concentration C_m in the melt varied between 10^{-4} and 3×10^{-1} mol %. However, the impurity concentration C in the crystal differed from C_m, depending on the type of impurity, and varied in the following ranges: for Ca between 10^{-3} and 1.6×10^{-1} mol %, for Pb between 2×10^{-4} and 1.65×10^{-2} mol %, and for Sr between 2×10^{-4} and 1.8×10^{-2} mol %. The samples for the tests were cut along the cleavage planes and had dimensions of $4\times4\times12$ mm. The crystals were uniaxially compressed along the [001] axis using an Instron machine at rates between 6.6×10^{-5} and 3.4×10^{-3} s^{-1}. The deformation temperature varied in the range 77–773 K.

Figure 1 gives the results of measurements of the yield stress σ_y as a function of the shear strain rate $\dot{a}$ for NaCl:Sr crystals containing different strontium concentrations C. It can be seen that the behavior of $\sigma_y(\dot{a})$ varies substantially with concentration. The usual dependence $\sigma_y(\dot{a})$, i.e., an increase in the yield stress with increasing strain rate, is only observed for samples containing the lowest impurity concentration (Fig. 1, curve *1*). The other samples show anomalous behavior: σ_y decreases at high rates (Fig. 1, curves *2* and *3*).

The impurity concentration also has a significant influence on the rate dependence of the yield stress for the other systems studied.

Figure 2 shows how the yield stress of NaCl:Ca single crystals depends on concentration at different strain rates and temperatures. It can be seen that at all deformation temperatures for NaCl:Ca crystals, the influence of the strain rate on the yield stress depends strongly on the impurity concentration: this influence is appreciable for $C\geqslant10^{-2}$ mol % and almost absent for low $C(C<10^{-2}$ mol %).

It is known that as the impurity content C increases, its state in the crystal matrix changes[1)] (Refs. 8 and 9). Bearing this factor in mind, we can conclude that the different influence of the strain rate on σ_y is evidently attributable to the inadequate state of the impurity defects at low impurity concentrations and also at high concentrations. Thus, these results indicate that the influence of the strain rate on the yield stress is controlled to a considerable extent by the structural state of the impurity defects which is determined by the impurity concentration.

The influence of the impurity concentration and state on $\sigma_y(\dot{a})$ was also observed for NaCl:Pb crystals (Fig. 3). It can be seen that the usual behavior, where an increase in $\dot{a}$ is accompanied by an increase in σ_y, is only observed for the lowest Pb^{2+} concentration. This relation was found at almost all the temperatures studied. A different picture emerged for other lead concentrations C (Fig. 3). It was found that the test temperature plays an important role: in many cases a change in temperature produced sharply opposing effects. For instance, the same change in strain rate between 6.6×10^{-5} and 3.4×10^{-3} s^{-1} produced an increase in the yield stress at 293 K (Fig. 3a, curves *1* and *2* lie above curve *3*) and a decrease at 220 K (Fig. 3b, $C\sim10^{-2}$ mol %, curves *2* and *1* lie below curve *3*). In addition, a decrease in σ_y at 373 K was replaced by the opposite effect at 673 K. It should be noted that for all the Pb^{2+} and Ca^{2+} concentrations studied at $T=673$ K where the impurities are dispersed, an increase in strain rate is accompanied by a regular increase in the yield stress, i.e., the usual behavior of $\sigma_y(\dot{a})$ is observed (Fig. 4).

Summarizing these results obtained for NaCl systems, we can conclude that $\sigma_y(\dot{a})$ is controlled by the structural

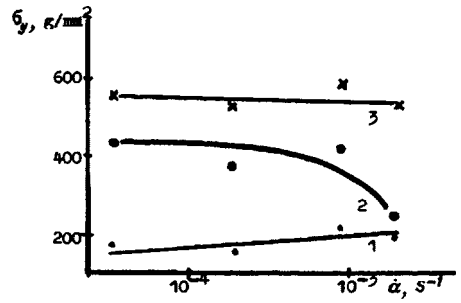

FIG. 1. Rate dependence of the yield stress for NaCl:Sr crystals: C, mol %: 3.7×10^{-4} (*1*), 6×10^{-3} (*2*), and 1.8×10^{-2} (*3*).

state of the impurity defects, which is determined by the impurity concentration and test temperature.

However, these data show that the influence of the strain rate on the variation of the plasticity parameters is determined not only by the state of the impurities but also by the shear strain rate.

An unusual dependence of σ_y on $\dot{a}$ is observed for NaCl:Ca crystals with $C\geqslant10^{-2}$ mol % (Fig. 2). For samples

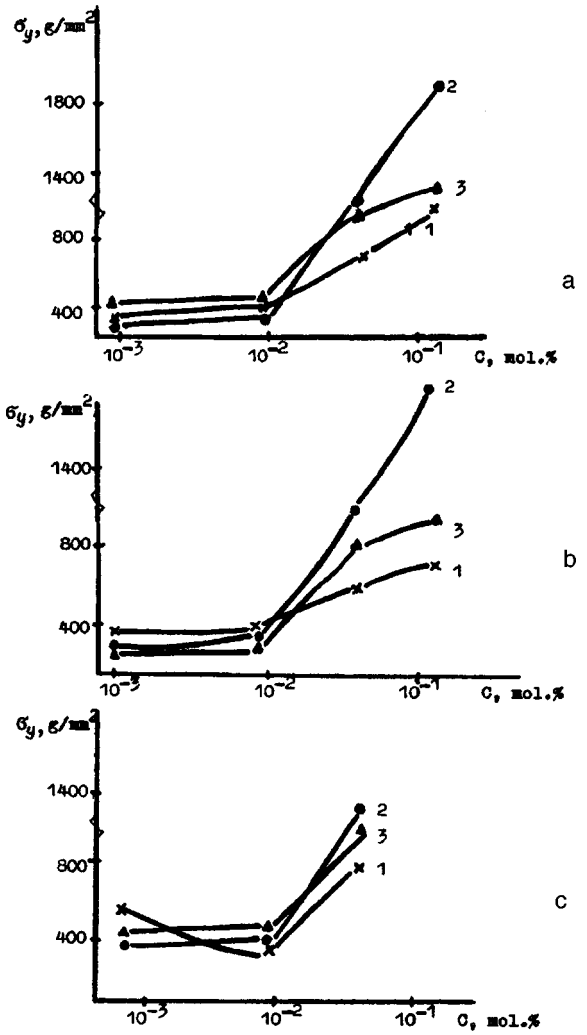

FIG. 2. Concentration dependences of the yield stress for NaCl:Ca crystals at various rates of shear strain: $\dot{a}$, s^{-1}: 3.4×10^{-3} (*1*), 3.4×10^{-4} (*2*), and 6.6×10^{-5} (*3*). Deformation temperature T, K: 373 (a), 293 (b), and 150 (c).

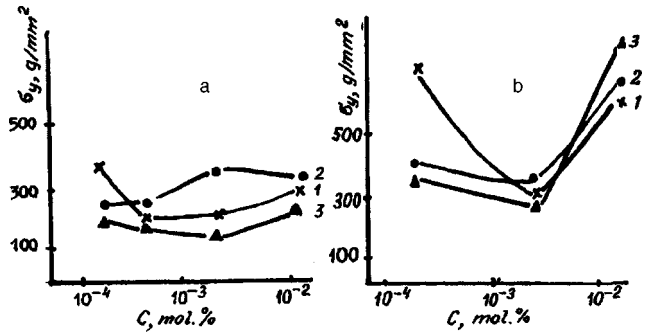

FIG. 3. Concentration dependences of the yield stress for NaCl:Pb crystals at various rates of shear strain: $\dot{a}$, s^{-1}: 3.4×10^{-3} (*1*), 3.4×10^{-4} (*2*), and 6.6×10^{-5} (*3*). Deformation temperature T, K: 293 (a) and 220 (b).

containing the same calcium concentrations (and thus being in the same state in the matrix), an increase in $\dot{a}$ initially leads to an increase in σ_y (Fig. 2, curves *2* lie above curves *1*), which is quite regular. In contrast, a further increase in $\dot{a}$ does not cause an additional increase in σ_y but a sharp drop (curves *3* lie below curves *2* and *1*). This feature of the rate dependence of the yield stress of NaCl:Ca crystals is typical of all temperatures and results for various T are plotted in Figs. 2a–2c. The usual behavior of $\sigma_y(\dot{a})$ is only observed at $T=673$ K (Fig. 4a). It has been noted that at this high temperature the state of the impurities changes abruptly and they become more dispersed. Thus, an analysis of these results suggests that the strain rate has an unusual influence on the yield stress when the Ca^{2+} impurities comprise large aggregates and intricate complexes, as is the case at high concentrations C and high temperatures when the impurities are not sufficiently broken down into small aggregates.

A particularly interesting result is that opposite effects are observed for the same structural state of the impurity defects (vertical cross section in Fig. 2): an increase in σ_y

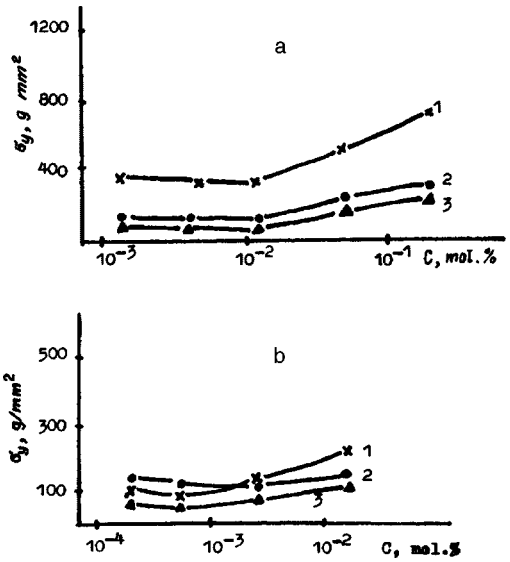

FIG. 4. Concentration dependences of the yield stress for NaCl:Ca (a) and NaCl:Pb (b) crystals at various rates of shear strain: $\dot{a}$, s^{-1}: 3.4×10^{-3} (*1*), 3.4×10^{-4} (*2*), and 6.6×10^{-5} (*3*). $T=673$ K.

with increasing strain rate is replaced by a sharp drop. This behavior of σ_y at high strain rates is most likely caused by a significant change in the mechanism of interaction between moving dislocations and the impurity center, which is probably caused by a difference in the velocities of the dislocations at different rates of shear strain. A mechanism is proposed to explain this sharp drop in σ_y at high $\dot{a}$. Assuming that the strain rate $\dot{\varepsilon}$ is expressed in the form $\dot{\varepsilon}=\mathbf{b}\dot{\rho}\bar{v}$, where **b** is the Burgers vector, ρ is the density of mobile dislocations, and $\bar{v}$ is the average dislocation velocity, it may be inferred that the increase in the strain rate $\dot{\varepsilon}$ at the yield stress stage is either caused by an increase in the average dislocation velocity $\bar{v}$ or by an increased rate of multiplication $\dot{\rho}$ of mobile dislocations.[11] However, the second method is less dominant in our case, since specific investigations have shown that at high $\dot{\varepsilon}$ the density of new dislocations is two or three orders of magnitude or more lower than ρ for low $\dot{\varepsilon}$. Thus, the dislocation multiplication rate $\dot{\rho}$ under deformation is lower at high rates of plastic deformation compared with that at low $\dot{\varepsilon}$. This behavior suggests that for these doped NaCl crystals, the increase in strain rate is mainly caused by an increase in the average velocity of the mobile dislocations. Taking this factor into account, we can explain the present results as follows. An increase in the rate of shear strain $\dot{a}$ leads to an increase in the kinetic energy of a dislocation, enabling this dislocation to become partially separated from the impurity atmosphere.[2)] However, the dislocation is not completely separated, since it still does not have sufficient energy to be finally released from the atmosphere but the atmosphere cannot keep up with the dislocations, which causes substantial additional hardening. This clearly explains the observed increase in the yield stress with increasing $\dot{a}$ in the range 10^{-5}–10^{-4} s^{-1} (Fig. 2, curve *2*).

Nevertheless, as the shear strain rate is increased further to $\dot{a}\sim 10^{-3}$ s^{-1}, the dislocation energy increases and may be sufficient to completely separate the dislocation from the impurity atmospheres, which makes it significantly easier for the dislocation to migrate and is accompanied by reduced motion stress. Thus, the separation of dislocations from impurity atmospheres may explain the sharp drop in the yield stress of NaCl:Ca crystals at high rates of shear strain (Fig. 2, curve *1*).

To sum up, we have identified two different factors having a separate influence on the yield stress of NaCl crystals: a) the structural state of the impurity defects and b) the shear strain rate. We have established that the influence of the shear strain rate on σ_y depends very much on the structural state of the impurity defects, which is determined by the impurity concentration and the test temperature. We identified two ranges of impurity concentration: low C, where σ_y is barely influenced and high C, where $\dot{a}$ has a substantial influence on σ_y.

For NaCl:Ca crystals we observed that, depending on the strain rate, impurities in the same structural state have opposite effects: the yield stress increases with increasing $\dot{a}$ and then falls sharply with a further increase in strain rate. A mechanism for interaction between a fast moving dislocation and defects is proposed to explain this extremely different behavior of σ_y with increasing $\dot{a}$.

[1)]At low concentrations Ca impurities in the crystal matrix are mainly in the form of impurity–cationic vacancy dipoles and their aggregates; at high C they are mainly in the form of complexes and precipitates.[8,9]

[2)]It is known that the nucleus of a dislocation in doped alkali halide crystals is surrounded by clouds of impurity defects (Cottrell, Suzuki, Snoeck clouds).[11] At high C the defect atmosphere around the dislocation most likely consists mainly of {310} and {111} plate-like complexes.[12]

[1] B. I. Smirnov, *Dislocation Structure and Hardening of Crystals* [in Russian], Nauka, Leningrad (1981).
[2] R. P. Zhitaru, O. V. Klyabin, and B. I. Smirnov, Izv. Akad. Nauk. Mold. SSR Ser. Fiz. Tekh. Mat. Nauk No. 2, 39 (1972).
[3] E. Orozko and F. Aguló-López, Acta Metall. **34**, 1701 (1986).
[4] A. A. Urusovskaya, E. V. Darinskaya, R. Voszka *et al.*, Cryst. Res. Technol. **16**, 597 (1981).
[5] Yu. S. Boyarskaya, R. P. Zhitaru, and N. A. Palistrant, Fiz. Tverd. Tela (Leningrad) **32**, 769 (1990) [Sov. Phys. Solid State **32**, 453 (1990)].
[6] Yu. S. Boyarskaya, R. P. Zhitaru, and N. A. Palistrant, Fiz. Tverd. Tela (Leningrad) **32**, 3433 (1990) [Sov. Phys. Solid State **32**, 1989 (1990)].
[7] Yu. I. Golovin and A. A. Shibkov, Fiz. Tverd. Tela (Leningrad) **28**, 3492 (1988) [Sov. Phys. Solid State **28**, 1964 (1988)].
[8] L. M. Soĭfer, *Physics of the Condensed State* No. 24 [in Russian], FTINT, Kharkov (1973), pp. 45–64.
[9] G. A. Andreev and B. I. Smirnov, Problemy Prochnosti No. 10, 122 (1971).
[10] E. Orozko, A. Mendoza, J. Soullard, and J. Rubio, Jpn. J. Appl. Phys. **21**, 249 (1982).
[11] I. I. Novikov, *Crystal Lattice Defects in Metals* [in Russian], Metallurgiya, Moscow (1988).
[12] E. M. Orozco, I. Soullard, C. Zaldo *et al.*, Philos. Mag. A **50**, 425 (1984).

Translated by R. M. Durham

Transfer of electronic excitation energy in a solid glassy phosphor activated with europium (III) and titanium (III)

I. M. Batyaev, A. M. Tinus, and E. V. Kleshchinov

A. I. Gertsen Russian State Pedagogical University, St. Petersburg
(Submitted June 26, 1997)
Pis'ma Zh. Tekh. Fiz. **24**, 38–41 (February 12, 1998)

A phosphor was synthesized using potassium aluminosilicophosphate glass activated with europium (III) and titanium (III). It is shown that the europium luminescence is quenched by titanium ions in this glass. © *1998 American Institute of Physics.* [S1063-7850(98)00702-2]

Problems involved in enhancing the energy efficiency of solid-state phosphors and lasers utilizing them are attracting increasing attention. Progress along many lines of research in modern science depends on the combination of results obtained in this field. In consequence, particular attention is being paid to the study of active media whose optical and energy characteristics may well be enhanced by nonradiative ''donor→acceptor'' transfer of excitation energy. Transfer of electronic excitation energy has been widely used in lasers because, rather than supplying excitation energy directly to those particles whose emission is desired, it is frequently far more advantageous to supply this energy to those particles which readily absorb it, do not emit themselves, and freely transfer their excitation to the required particles.

Here we investigate the interaction in a Eu^{3+}–Ti^{3+} system in potassium aluminosilicophosphate glass. Titanium (III) ions are used as an independent activator[1–4] and as a sensitizer for the luminescence of various rare-earth ions.[5–8] Trivalent europium is a fairly widely used rare-earth activator for crystals, glass, and dyes.[9–12] Systems activated with europium (III) ions are of interest for various reasons, including the fact that europium is a luminescence activator with a high quantum yield, so that it can be used in laser technology. A laser utilizing an alcohol solution of europium benzoylacetonate was first reported in 1963 by Lempicki and Samelson.[13] Researchers were attracted by the relatively simple energy level structure, which makes it easier to interpret the optical transitions and use these to study the structure of the luminescence centers. This is reflected in the use of europium as a spectroscopic probe to study the structure of many materials.[14]

Silicon oxide, potassium metaphosphate, and aluminum were used to prepare the charge. Europium was introduced as the oxide Eu_2O_3 and titanium as the oxide TiO_2, which were then reduced. The concentration of the activator ions was 5 wt. % europium and 0.5 wt. % titanium.

The electronic absorption spectra were recorded using an SF-20 spectrophotometer. The luminescence spectra were re-

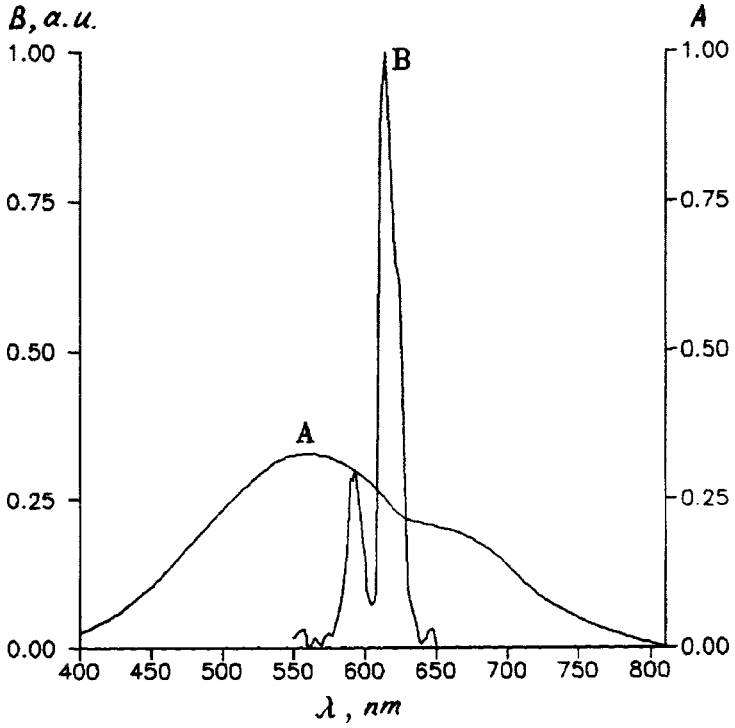

FIG. 1. Absorption spectrum (A) of potassium aluminosilicophosphate glass activated with Ti^{3+} and luminescence spectrum (B) for this glass activated with Eu^{3+}.

corded with an SDL-1 spectrometer and an FÉU-62 photomultiplier. The luminescence was excited with an LGI-21 nitrogen laser ($\lambda_{exc}=337$ nm) and an LGN-222 helium–neon laser ($\lambda_{exc}=630$ nm, $P=55$ mW).

The electronic spectrum of this glass reveals superposed absorption bands of titanium and europium. We detected no visible departures from the spectra of the corresponding noncoactivated ions in this matrix. Glasses doped only with europium ions exhibit intense luminescence in the 550–650 nm range (see Fig. 1, curve *B*). It can be seen that the bands of the europium luminescence spectrum (curve *B*) and the titanium absorption band (curve *A*) overlap. In the luminescence spectrum of the glass coactivated with both Eu^{3+} and Ti^{3+}, the relative intensity of the europium luminescence band decreases more than 25 times.

A study of the luminescence decay kinetics revealed that the average excited state lifetime of the Eu^{3+} ions decreased from 2.5 ms to 14 μs in the presence of Ti^{3+} ions.

To sum up, the interaction in a Eu^{3+}–Ti^{3+} system in glasses has been investigated for the first time and it has been shown that the europium (III) ion luminescence is quenched in the presence of titanium (III) ions.

[1] S. B. Sukhanov and I. M. Batyaev, Opt. Spektrosk. **72**, 1367 (1992) [Opt. Spectrosc. **72**, 765 (1992)].
[2] I. M. Batyaev and I. V. Golodova, Opt. Spektrosk. **77**, 54 (1994) [Opt. Spectrosc. **77**, 45 (1994)].
[3] S. B. Sukhanov, *Spectral and Luminescence Properties of Phosphate Glass Activated with Titanium (III) and Europium (III)*, Author's Abstract of Thesis for Candidate's Degree [in Russian], A. I. Gertsen Russian State Pedagogical University, St. Petersburg (1994).
[4] I. V. Golodova, *Spectral, Luminescence, and Various Physicochemical Properties of Gallium Phosphate Glasses Activated with Ti^{3+} and Nd^{3+} Ions*, Author's Abstract of Thesis for Candidate's Degree [in Russian], A. I. Gertsen Russian State Pedagogical University, St. Petersburg (1994).
[5] I. M. Batyaev and E. B. Kleshchinov, Pis'ma Zh. Tekh. Fiz. **22**(12), (1996) [Tech. Phys. Lett. **22**, 34 (1996)].
[6] I. M. Batajev, S. B. Sukhanov, O. A. Lasor, and E. B. Kletchinov, *Abstract of Papers presented at Eleventh Conference on Physical Methods in Coordination Chemistry*, Kishinev, 1993, p. 85.
[7] I. M. Batyaev and S. B. Sukhanov, Pis'ma Zh. Tekh. Fiz. **20**(10), 38 (1994) [Tech. Phys. Lett. **20**, 403 (1994)].
[8] I. M. Batyaev and I. V. Golodova, Opt. Spectrosk. **78**, 468 (1995) [Opt. Spectrosc. **78**, 421 (1995)].
[9] I. M. Batyaev, Usp. Khim. **40**, 1333 (1971).
[10] T. A. Privalova, Thesis for Candidate's Degree in Chemical Sciences [in Russian], Leningrad (1972).
[11] *Laser Handbook*, edited by A. M. Prokhorov, Parts 1 and 2 [Russ. transl. with changes and additions, Sovetskoe Radio, Moscow, 1978].
[12] I. M. Batyaev, S. M. Shilov, and Kolani Meĭulebte, Opt. Spektrosk. **76**, 424 (1994) [Opt. Spectrosc. **76**, 378 (1994)].
[13] A. Lempicki and H. Samelson, Phys. Lett. **4**, 133 (1963).
[14] V. F. Zolin and L. G. Koreneva, *Rare-Earth Probes in Chemistry and Biology* [in Russian], Moscow (1980).

Translated by R. M. Durham

Nonlinear effects in dynamic loading of a material with defect zones

S. G. Psakh'e, K. P. Zol'nikov, and D. Yu. Saraev

Institute of Physics of Strength of Materials and Materials Science, Siberian Branch of the Russian Academy of Sciences, Tomsk

(Submitted July 3, 1997)
Pis'ma Zh. Tekh. Fiz. **24**, 42–46 (February 12, 1998)

An analysis is made of some characteristic features of the interaction between solitary pulses (soliton-like waves) generated under high-velocity loading and structural defects in an Al crystallite. Calculations are made using the molecular dynamics method. It is shown that in materials undergoing shear loading and those undergoing compression different types of solitary pulses are formed which interact differently with regions containing structural defects. The waves formed under compression have a higher propagation velocity in the material, and their profile recovers fairly rapidly after propagating through defect zones. These phenomena are of interest for developing methods of nondestructive testing. © *1998 American Institute of Physics.* [S1063-7850(98)00802-7]

One of the most important and interesting manifestations of nonlinear effects in materials is the formation of solitary waves under high-velocity loading.[1–5] It was shown in Refs. 4–6 that the interaction between solitary waves and material defects such as vacancy clusters may result in the formation of hot spots which play an important role in the initiation of solid-phase reactions. Moreover, various characteristics of hot spots such as their lifetime, maximum heating temperature, and so on, are related to the amplitude of the solitary pulse.[5] In many respects, the behavior of these solitary pulses is similar to the behavior of solitons in one-dimensional chains.[1,2,7]

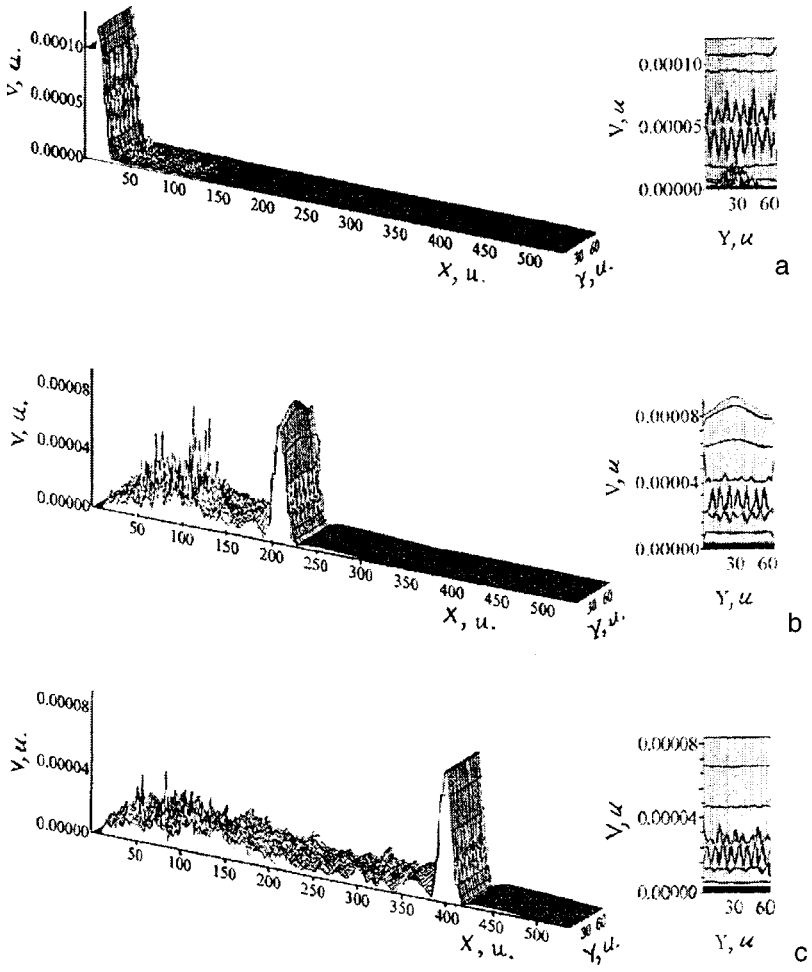

FIG. 1. Distribution of atomic velocities in a sample undergoing compression in the XY plane and in the Y direction: a—$t=0$, b—$t=300\ \Delta t$, and c—$t=1200\ \Delta t$.

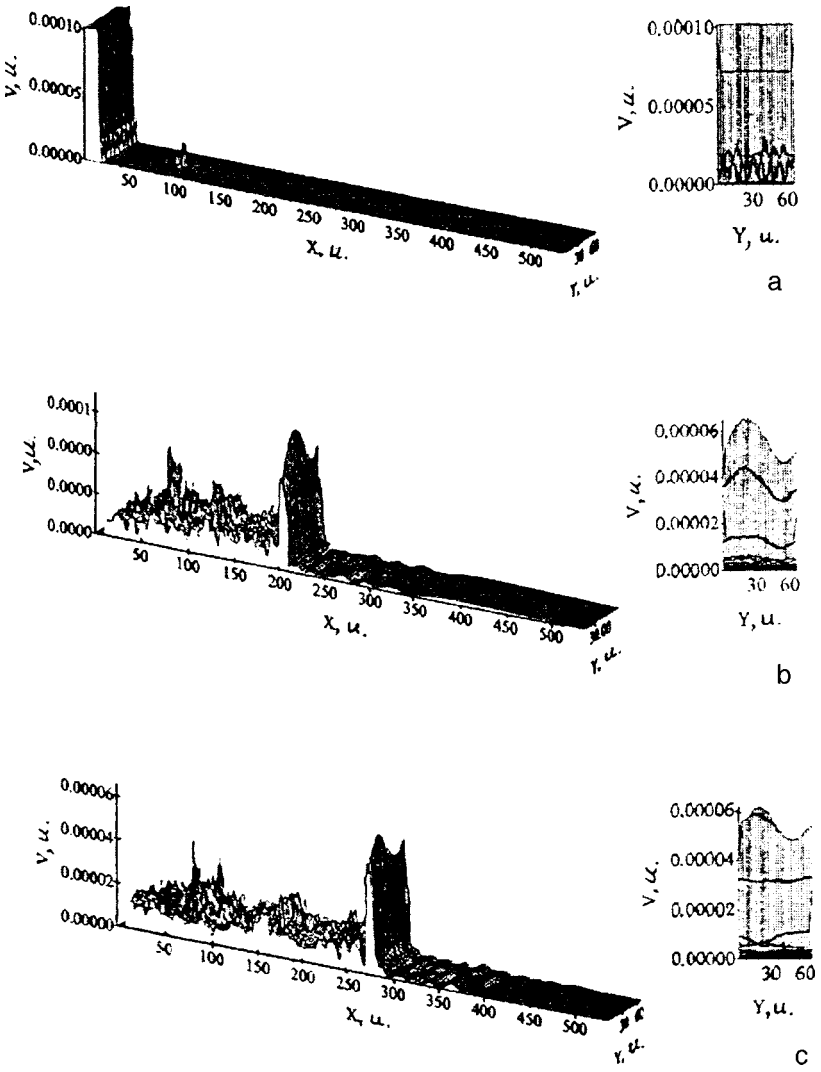

FIG. 2. Distribution of atomic velocities in a sample undergoing shear loading in the XY plane and in the Y direction: a—$t=0$, b—$t=1100\ \Delta t$, and c—$t=1500\ \Delta t$.

Here we investigate some characteristics of the propagation of solitary waves through regions of reduced atomic density. We also study differences in the generation and propagation of solitary waves initiated by high-velocity shear and compression.

The investigations were based on the molecular dynamics method and used the unique Monster-MD program package.[8]

A three-dimensional aluminum crystallite containing approximately 12,500 atoms was modeled at a temperature close to 0 K. The Z, Y, and X coordinate axes were oriented in the $\langle 111\rangle$, $\langle \overline{2}11\rangle$, and $\langle 01\overline{1}\rangle$ directions, respectively. Periodic boundary conditions were used in the Y and Z directions, while at the faces perpendicular to X the boundary conditions were set as follows:

1) For compression $V_z=V_y=0$, $V_x^l=\text{const}$, $V_x^r=0$, where V^l is the velocity component at the left edge of the sample and V^r is that at the right edge;

2) For shear loading $V_z=V_x=0$, $V_y^l=\text{const}$, $V_y^r=0$.

A region with an elevated concentration of point defects was created near the left edge of the sample in the X direction, and the sample then relaxed.

Note that microscopic calculations are usually made using the atomic system of units[9] in which the Bohr radius, Planck's constant, and the electron charge are unity. The integration step for the equations of motion was 100 atomic time units, which corresponds to 2.42×10^{-15} s. The effective pair interaction potential was calculated using pseudopotential theory, as in Ref. 10.

An analysis was made of the distribution of the atomic velocities and the change in the profile of the solitary wave at various times. Figure 1 shows distributions of the crystallite atomic velocities in the XY plane and in the Y direction for a solitary wave initiated by compression. It can be seen from a comparison of Figs. 1a and 1b that the wave crest changes substantially in the region with structural defects. Note that the shape of the crest recovers its initial form fairly rapidly, as can be seen from Fig. 1c.

A different pattern is observed for the propagation of solitary waves initiated by high-velocity shear (Fig. 2). In this case, the shape of the solitary wave crest (Fig. 2a) also changes significantly as it propagates through the region with point defects (Fig. 2b), but the initial shape of the wave crest was not restored and the change remained stable (Fig. 2c).

A more detailed analysis of the results revealed that different types of mechanical loading (shear, compression) gen-

erate different types of solitary waves. The profile of the solitary waves formed by high-velocity compression is determined by the structure of the particular part of the sample in which it propagates. It was noted that a wave in a defect-free region of the crystal recovers its initial form soon after interacting with structural defects. The calculations showed that a solitary wave initiated by high-velocity shear differs from the ''compression'' waves not only because its amplitude contains shear velocity components but also because it possesses a unique ''memory effect.'' For example, if the material contains regions saturated with different types of defects, the crest shape of this solitary wave will undergo constant changes. Thus, a solitary wave initiated by shear may carry information on whether the material has regions containing structural defects. This effect may be of some interest for the development of methods of nondestructive monitoring and testing to determine whether a material contains regions saturated in structural defects, and also to monitor the quality of coatings.

[1] J. Betteh and J. Powel, Appl. Phys. **49**, 3933 (1978).
[2] G. K. Straub, B. L. Holian, and R. G. Petsheck, Phys. Rev. B **19**, 4049 (1979).
[3] S. G. Psakh'e, K. P. Zol'nikov, and S. Yu. Korostelev, Pis'ma Zh. Tekh. Fiz. **21**(13), 1 (1995) [Tech. Phys. Lett. **21**, 489 (1995)].
[4] S. G. Psakh'e, D. Yu. Saraev, and K. P. Zol'nikov, Pis'ma Zh. Tekh. Fiz. **22**(10), 6 (1996) [Tech. Phys. Lett. **22**, 389 (1996)].
[5] S. G. Psakh'e, K. P. Zol'nikov, and D. Yu. Saraev, Fiz. Goreniya Vzryva **33**(2), 143 (1997).
[6] D. H. Tsai, J. Chem. Phys. **95**, 7497 (1991).
[7] S. Yu. Korostelev., S. G. Psakh'e, and V. E. Panin, Deposited Paper No. 6080–85 [in Russian], VINITI, Moscow (1985).
[8] S. G. Psakhie, S. Yu. Korostelev, S. I. Negreskul, K. P. Zolnikov, Z. Wang, and S. Li, Phys. Status Solidi B **176**, K41 (1993).
[9] W. A. Harrison, *Pseudopotential in the Theory of Metals* (North-Holland, Amsterdam, 1966).
[10] S. G. Psakh'e and V. E. Panin, Fiz. Met. Metalloved. **50**, 620 (1980).

Translated by R. M. Durham